# LARGE-SCALE CIRCULATIONS IN THE EAST PACIFIC AND WEST AFRICA REGIONS AND THEIR INTERACTION WITH CONVECTIVE STRUCTURES

A Dissertation

by

LIDIA HUAMAN CHUQUIHUACCHA

Submitted to the Graduate and Professional School of
Texas A&M University
in partial fulfillment of the requirements for the degree of

DOCTOR OF PHILOSOPHY

| | |
|---|---|
| Chair of Committee, | Courtney Schumacher |
| Committee Members, | Anita Rapp |
| | Lee Panetta |
| | Ping Chang |
| Head of Department, | Ramalingam Saravanan |

December 2021

Major Subject: Atmospheric Sciences

ABSTRACT

The interaction of large-scale atmospheric circulations with convective systems in two tropical regions (i.e., the East Pacific and West Africa) is studied using field campaign, reanalysis, and satellite datasets. In the East Pacific, organized cloud systems that propagate eastward or westward at synoptic time scales can alter the shallow meridional circulation (SMC) and deep meridional circulation (DMC) seen in the Intertropical Convergence Zone (ITCZ). During boreal winter, I identified convective disturbances that propagate eastward at 10 m/s within the central and East Pacific north of the ITCZ and exhibit high cloudiness associated with upper-level divergence. These eastward propagating disturbances do not impact the SMC, but the DMC in the northern part of the ITCZ strengthens. During boreal spring, convectively-coupled Kelvin waves initiate in the West Pacific and propagate along the ITCZ axis into the East Pacific at 15 m/s. The shallow convection ahead of the Kelvin wave enhances the SMC and the deep convection within the Kelvin wave enhances the DMC. During boreal summer and fall, easterly waves appear to strongly modulate the SMC and DMC in the East Pacific ITCZ. The easterly wave trough enhances the DMC, and the subsequent convectively-suppressed easterly wave ridge enhances the SMC over the southern part of the ITCZ. Additionally, the vertical velocity associated with the SMC and DMC in the East Pacific is assessed using the Organization of Tropical East Pacific Convection (OTREC) field campaign dataset. The OTREC 2019 field campaign observations were crucial to identify deficiencies in reanalysis and satellite products. Reanalyses underestimate the

DMC observed in the northern part of the ITCZ and satellite products underestimate the SMC observed in southern part of the ITCZ. Finally, the diurnal variation of the SMC and DMC over West Africa during the pre-monsoon and monsoon seasons is also studied. A daytime sea breeze and two nocturnal low-level jets (NLLJs) are shown to have varying impacts on the meridional overturning circulation and convective organization over West Africa. The daytime sea breeze initiates strong northward-propagating convection from the coast, especially during the pre-monsoon season, a coastal NLLJ enhances northward moisture transport during the monsoon season, and an inland NLLJ promotes the dry SMC over the Sahara during both seasons.

# ACKNOWLEDGEMENTS

I would like to thank my advisor and committee chair Dr. Courtney Schumacher for her guidance and support throughout the course of this research. She has been a wonderful and energetic advisor who also supported emotionally throughout my Ph.D. journey. Also, I want to thank my collaborators Dr. George N. Kiladis from NOAA/ Earth System Research Laboratory, Prof. Eric D. Maloney from Colorado State University, and Dr. Adam Sobel from Columbia University for useful discussions and comments in this research. Thanks to A. Funk for pre-processing the TRMM and GPM data products.

I also would like to thank my other committee members Dr. Anita Rapp, Dr. Lee Panetta, and Dr. Ping Chang for their support and comments in this dissertation. Finally, I would also like to thank the members of the A-Team for providing a fun and resourceful work environment.

CONTRIBUTORS AND FUNDING SOURCES

## Contributors

This work was supervised by Professor Courtney Schumacher. The data used in this dissertation were acquired from Goddard Earth System division and Information Service Center (GPM, TRMM and MERRA-2; http://disc.sci.gsfc.nasa.gov/), ECMWF (ERA5; http://apps.ecmwf.int/datasets/), NOAA/ESRL (NCEP-NCAR; http://www.esrl.noaa.gov/psd/), NCAR/UCAR research data archive (JRA, https://rda.ucar.edu), and Zenodo science (3DVar OTREC data; doi:10.5281/zenodo.5152171). Dr. Naoko Sakaeda from Oklahoma University provided the CLAUS Tb data.

This work was completed by the student independently, and chapter II in this dissertation is a version of Huaman, Lidia, C. Schumacher, and G. Kiladis (2020) "Eastward-propagating disturbances in the tropical Pacific", *Monthly Weather Review*. Chapter III has been conditionally accepted in the *Journal of the Atmospheric Sciences*, and Chapters IV and V have been submitted to *Geophysical Research Letters* and the *Journal of Geophysical Research*, respectively.

## Funding Sources

Graduate study was supported by a NASA Earth and Space Science Fellowship (NESSF) fellowship from NASA and The Good Neighbor scholarship from Texas A&M University. This work was also made possible in part by NASA PMM under Grant Number 80NSSC19K0734.

# NOMENCLATURE

| | |
|---|---|
| AEJ | African easterly jet |
| AMJ | April, May, and June |
| CAPE | Convective available potential energy |
| CCEW | Convectively coupled equatorial waves |
| CIN | Convective inhibition |
| CLAUS | Cloud Archive User Services |
| CLLJ | Caribbean low-level jet |
| CSH | Convective Stratiform Heating |
| DJF | December, January, and February |
| DMC | Deep meridional circulation |
| DPR | Dual-Frequency Precipitation Radar |
| EOF | Empirical Orthogonal Functions |
| EP | East Pacific |
| EPD | Eastward propagating disturbances |
| EPIC | East Pacific Investigation of Climate Processes in the Coupled Ocean |
| ERA5 | ECMWF Reanalysis 5$^{th}$ generation |
| EW | Easterly waves |
| GOES | Geostationary Operational Environment Satellite |
| GPM | Global Precipitation Measurement |

| | |
|---|---|
| GTS | Global Telecommunication System |
| HCR | Hiaper cloud radar |
| IMERG | Integrated Multi-satellitE Retrievals for Global Precipitation Measurement |
| IR | Infrared |
| ITCZ | Intertropical Convergence Zone |
| JAS | July, August, and September |
| LCL | Lifting condensation level |
| MAM | March, April, and May |
| MCS | Mesoscale convective system |
| MERRA2 | Modern-ERA Retrospective analysis for Research and Applications V2 |
| MJO | Madden-Julian Oscillation |
| MRG | Mixed Rossby-Gravity |
| MSE | Moist Static Energy |
| NCAR | National Center of Atmospheric Research |
| NH | Northern Hemisphere |
| NLLJ | Nocturnal low-level jet |
| OSTIA | Operational Sea Surface Temperature and Sea Ice Analysis |
| OTREC | Organization of Tropical East Pacific Convection |
| PBL | Planetary boundary layer |
| PC | Principal component |

| | |
|---|---|
| PR | Precipitation radar |
| PV | Potential vorticity |
| RF | Research flight |
| SH | Southern hemisphere |
| SLH | Spectral Latent Heating |
| SLLJ | Sahel/Sahara low-level jet |
| SMC | Shallow meridional circulation |
| SST | Sea surface temperature |
| $T_b$ | Brightness temperature |
| TD | Tropical disturbance |
| TEPPS | Tropical Eastern Pacific Process Study |
| TRMM | Tropical Rainfall Measuring Mission |

TABLE OF CONTENTS

Page

ABSTRACT ..... ii

ACKNOWLEDGEMENTS ..... iv

CONTRIBUTORS AND FUNDING SOURCES ..... v

NOMENCLATURE ..... vi

TABLE OF CONTENTS ..... ix

LIST OF FIGURES ..... xi

LIST OF TABLES ..... xvii

CHAPTER I INTRODUCTION ..... 1

CHAPTER II EASTWARD-PROPAGATING DISTURBANCES IN THE TROPICAL PACIFIC ..... 5

2.1. Background ..... 5
2.2. Data and Methodology ..... 8
2.3. EPDs in the tropical Pacific ..... 10
2.3.1. Mean state conditions ..... 10
2.3.2. Horizontal structure of eastward 2.5-20-day band regressions ..... 15
2.3.3. Vertical structure of eastward 2.5-20-day band regressions ..... 22
2.4. EPD impacts on the meridional overturning circulation ..... 28
2.5. Summary ..... 35

CHAPTER III EASTERLY WAVES IN THE EAST PACIFIC DURING THE OTREC 2019 FIELD CAMPAIGN ..... 38

3.1. Background ..... 38
3.2. Data and methods ..... 43
3.2.1. Data description ..... 43
3.2.2. Identification of EWs ..... 45
3.3. Horizontal and vertical structure of the OTREC EWs ..... 49
3.3.1. Composite EW structure ..... 49
3.3.2. Individual EWs ..... 56

3.4. Moisture budget ..... 62
3.5. EWs and the shallow and deep meridional circulations ..... 70
3.6. Summary ..... 74

CHAPTER IV ASSESSING THE VERTICAL VELOCITY IN THE EAST PACIFIC ITCZ ..... 78

4.1. Background ..... 78
4.2. Data and Methodology ..... 80
4.3. Vertical velocity during OTREC ..... 83
4.4. Monte Carlo Analysis ..... 87
4.5. Summary ..... 93

CHAPTER V DIURNAL VARIATION OF THE MERIDIONAL FLOW AND RAINFALL OVER WEST AFRICA DURING THE PRE-MONSOON AND MONSOON SEASONS ..... 95

5.1. Background ..... 95
5.2. Data and Methodology ..... 98
5.3. Seasonal mean precipitation and meridional overturning ..... 101
5.4. Diurnal cycle of dynamical fields ..... 105
5.5. Diurnal cycle of precipitation ..... 115
5.6. Synthesis of sea breeze and NLLJ impacts over West Africa ..... 121
5.7. Summary ..... 125

CHAPTER VI CONCLUSIONS ..... 128

6.1. East Pacific ..... 128
6.2. West Atlantic ..... 131

REFERENCES ..... 134

LIST OF FIGURES

Page

Figure 1.1 Annual precipitation in mm/d from TRMM (1998-2010). Box a indicates the region to study eastward disturbances (Chapter 2), box b indicates the region of the OTREC field campaign (Chapter 3 and 4), and box c indicates the region to study the diurnal cycle of African convection (Chapter 5). .....3

Figure 2.1 Wavenumber-frequency power spectrum (from 120°E-60°W) of the symmetric component of Tb summed from 15°S to 15°N for 1984-2016 for a) DJF and b) MAM. Thin black lines represent the dispersion curves for CCEWS. Heavy dashed gray and solid black boxes represent regions of Kelvin-band and east-band filtering, respectively. Wavenumber-frequency power spectrum (from 120°E – 60°W) of total PV summed from 20°N to 50°N for c) DJF and d) MAM. .....9

Figure 2.2 Hovmöller diagram of $T_b$ anomalies (shaded) and eastward 2.5-20-day band $T_b$ (contours; 5°C solid, - 5°C dashed) in °C along 2.5°-10°N from Dec 2007 to May 2008. The stars show two EPD events on 1 January and 27 March. .....11

Figure 2.3 Climatological eastward 2.5-20-day band $T_b$ (1984-2016, shaded) and precipitation (1998-2016, contours) variance in $°C^2$ and $mm^2\ d^2$, respectively, and 30-day high-pass-filtered E-vectors (1984-2016) in $m^2\ s^{-2}$ for a) DJF and b) MAM. Precipitation contour interval is 15 $mm^2\ d^{-2}$, $T_b$ values poleward of 20°N are masked out. Meridional cross sections at 130°W of $T_b$ and precipitation variance for c) DJF and d) MAM. .....13

Figure 2.4 a) Contribution of variance explained by the first four EOFs for both seasons. First EOF of eastward 2.5-20-day band $T_b$ for b) DJF and c) MAM. 15

Figure 2.5 Regressed values of a-d) $T_b$ in °C (shading), geopotential height in m (contours), precipitation in mm $d^{-1}$ (thick contours) and winds (vectors) at 850 hPa, and e-h) streamfuction in $m^2\ s^{-2}$ (contours) and winds (vectors) at 200 hPa, based on PC1 at different lag days during DJF. Panels e-h are on a different spatial scale than panels a-d. Geopotential height (streamfunction) contour interval is 4 m ($2 \times 10^5\ m^2\ s^{-1}$), precipitation contour interval is 1 mm $d^{-1}$. Locally significant winds are shown in bold vectors, with the largest vector around 3 m $s^{-1}$. .....18

Figure 2.6 Same as Fig. 2.5 but for MAM. .....19

Figure 2.7 Regressed values of $T_b$ in °C (contours), 200-hPa divergence in $s^{-1}$ (shaded) and winds in $10^{-6}$ m $s^{-1}$ (vectors) at lag day 0 for a) DJF and b)

MAM. $T_b$ contour interval is 1°C. Locally significant winds are shown in bold vectors, with the largest vector around 3 m $s^{-1}$. ..... 20

Figure 2.8 Longitude-time diagram of regressed $T_b$ in °C (shading) and 200-hPa streamfunction in $m^2$ $s^{-1}$ (contours), averaged from 2.5°N to 12.5°N from day -10 to day 8. Contour interval is 1 $\times 10^5$ $m^2$ $s^{-1}$ with positive (negative) values in solid (dashed) contours. ..... 21

Figure 2.9 Time-height cross sections of zonal wind in m $s^{-1}$ from the equator to 10°N for a) DJF at 140°N and b) MAM 160°N. ..... 23

Figure 2.10 Regressed values of a-c) $T_b$ in °C (blue and red contours), TRMM precipitation in mm $d^{-1}$ (gray contours), potential vorticity in PV units ($10^{-6}$ $m^2$ $s^{-1}$ K $kg^{-1}$, shaded) and winds in m $s^{-1}$ (vectors) at 850 hPa, and d-f) pressure-latitude cross sections of omega in Pa $s^{-1}$ and meridional flow (vertical velocity is amplified 15 times for better illustration), based on PC1 at different lag days during DJF. $T_b$ contour interval is 1°C. Locally significant winds are shown in bold vectors, with the largest vector around 3 m $s^{-1}$. ..... 25

Figure 2.11 Same as Fig. 2.10 but for MAM. Cross-sections (d-f) are at different longitude. ..... 26

Figure 2.12 Pressure-longitude cross section of the climatological (1984-2016) meridional wind in m $s^{-1}$ at the equator for a) DJF and b) MAM. The zero wind line is marked by the heavy black contour. Meridional circulation over the east Pacific at 120°W in vectors (vertical pressure velocity is amplified 15 times for better illustration) and vertical pressure velocity (Pa $s^{-1}$, shaded) for c) DJF and d) MAM. ..... 28

Figure 2.13 Latitude-pressure cross sections of omega in Pa $s^{-1}$ (shading) and meridional circulation v, $\boldsymbol{\omega}$ (vectors) anomalies in the far east Pacific (120°W) at different lag days for a-c) DJF and d-f) MAM. ..... 32

Figure 2.14 a-b) Eastward 2.5-20-day band Tb in °C (shading), TRMM precipitation in mm $d^{-1}$ (thick contours), 200-hPa streamfunction anomalies in ms (contours) and 200-hPa wind vector anomalies in mm s during a short-lived EPD on 1 January 2008 and a Kelvin wave on 27 March 2008, respectively. Largest wind vector is around 40 m $s^{-1}$ and precipitation (streamfunction) contour interval is 0.2 mm day (4 $m^2$ $s^{-1}$). c-d) Nadir swath view of CloudSat reflectivity in dBZ for each event along the red cross section line... 34

Figure 3.1 a) Total precipitation in mm $d^{-1}$ from IMERG and SST in C° from OSTIA, and b) cross section of omega in Pa $s^{-1}$ and meridional flow across the

OTREC region (blue rectangle in a) from ERA5 for August and September 2019. .....41

Figure 3.2 Hovmöller diagrams averaged from 3 - 11°N of a) precipitation in mm $d^{-1}$ from IMERG, and b) 600-hpa vorticity in $s^{-1}$ and c) 600-hPa meridional winds in m $s^{-1}$ from ERA5. Total values are shaded and TD-band values are in contours (precipitation contours every 4 mm $d^{-1}$, vorticity contours every 4 $s^{-1}$, and 600-hPa meridional wind contours every 2 m $s^{-1}$). Symbols are placed in the OTREC region, the stars indicate OTREC RF dates and the circles highlight enhanced convection (blue) and suppressed convection (red) associated with EWs. .....47

Figure 3.3 Time series of total (left axis) and TD-band (right axis) IMERG precipitation over the East Pacific OTREC flight box (89° - 86°W, 3° - 11°N). Dashed lines indicates the threshold of TD-band precipitation over the OTREC period average $\pm$ 1.25 standard deviation. As in Fig. 3.2, the stars indicate OTREC RFs and the circles highlight when EWs were present. .....48

Figure 3.4 IMERG precipitation in mm $d^{-1}$ averaged over the three OTREC EWs during a) enhanced (day 0) and b) suppressed (day +2) conditions. Longitude-time diagrams of c) total precipitation and d) anomaly precipitation for the latitude range 3°-11°N during the three EW events. The black box indicates the OTREC region box. .....50

Figure 3.5 (a-c, g-i) Precipitation anomalies in mm $d^{-1}$ superimposed with 600-hPa horizontal wind anomalies across the East Pacific and (d-f, i-l) omega cross sections in Pa $s^{-1}$ superposed by meridional flow over the OTREC region (gray rectangle) from day -2 to day +3 composited for the three EWs. The trough and ridge centers of the EW are labeled as T and R, respectively. Largest wind vector is 5 m $s^{-1}$. .....52

Figure 3.6 Time-height diagrams of vorticity ($s^{-1}$), specific humidity (g $kg^{-1}$), meridional wind (m $s^{-1}$), and omega (Pa $s^{-1}$) anomalies at a-d) 7-11°N and e-h) 3-7°N averaged at 89-86°W over the three OTREC EWs. .....55

Figure 3.7 Skew-T diagrams for all the 3 EWs (08/07, 08/15 and 09/18) during the OTREC field campaign from ERA5 and OTREC RFs at day 0 (left) and day 2 (right) for (a,b) 8°N and (c,d) 4°N. RF times are between 12-18 UTC. .....57

Figure 3.8 (a-b, e-f) GOES IR images (red/dark colors indicate convective regions) and (c-d, g-h) vertical reflectivity cross sections in dBZ from the NCAR Hiaper Cloud Radar during enhanced precipitation on 7 August 2019 (i.e., positive phase of EW) and suppressed precipitation on 17 August 2019 (i.e., negative phase of EW) across the flight path indicated by the red arrow in

the GOES IR images. The trough and ridge centers of the EW are labeled as T and R, respectively. ..... 62

Figure 3.9 Composite OTREC EW anomalies (shaded, in mm $d^{-1}$) of (a-e) moisture tendency from horizontal advection and (f-h) moisture tendency from vertical advection minus precipitation from day -1 to day +3 using ERA5 reanalysis. All images are superposed by 600-hPa wind vectors and ERA5 precipitation anomalies. Positive (negative) precipitation anomalies are in blue (red) contours, contours are every 10 (5) mm $d^{-1}$ starting at 5 mm $d^{-1}$. The trough and ridge centers of the EW are labeled as T and R, respectively. Largest wind vector is 5 m $s^{-1}$. ..... 65

Figure 3.10 Composite OTREC EW time-latitude diagrams over 89°-86°W of a-b) omega anomalies in Pa $s^{-1}$ at 400 hPa and 900 hPa (dashed lines indicate the climatological position of maximum omega at the determined level), c-d) vertical and horizontal advection of total MSE in W $m^{-2}$, e) anomalies of moisture tendency from vertical advection in mm $d^{-1}$ superposed by moisture tendency from vertical advection minus precipitation in mm $d^{-1}$ (contours every 2 mm $d^{-1}$, negative values dashed and positive values solid), and f) anomalies of moisture tendency from horizontal advection in mm $d^{-1}$ .. 68

Figure 3.11 Composite OTREC EW a-b) vertical velocity in Pa $s^{-1}$ and meridional flow, c-d) relative humidity in % averaged over 89°-86°W, and e-f) anomalies of moisture tendency from horizontal advection in shaded and vertical advection in contours superposed by winds at 850 hPa during day 0 and +2. Positive (negative) vertical advection anomalies are in blue (red) contours, contours are every 5 mm $d^{-1}$ starting at 3 mm $d^{-1}$. The trough and ridge centers of the EW are labeled as T and R, respectively. Largest wind vector is 6 m $s^{-1}$. ..... 71

Figure 3.12 Meridional wind profiles from ERA5 in m $s^{-1}$ at (a,b) 7 - 8°N, 89° - 86°W and (c, d) 4 - 5°N, 89° - 86°W for the three EWs and the August-September average during day 0 (a, c) and +2 (b, d). ..... 73

Figure 3.13 Latitude-height sketch of the evolution of EWs and their effect on shallow and deep circulations in the East Pacific. Horizontal (vertical) bold vectors indicate total meridional winds (upward motion) larger than 8 m $s^{-1}$ (0.3 Pa $s^{-1}$). Positive (negative) total vorticity is shown in a red cyclonic (blue anticyclonic) vertical vorticity features and bold trajectories indicate vorticity of magnitude larger than 4 x $10^{-5}$ $s^{-1}$. The EW horizontal scale is approximated by the size of vorticity features. The clouds denote the position of the shallow and deep convection. Encircled x's (dots) denote westward (eastward) winds. ..... 75

Figure 4.1 a) Precipitation from IMERG in mm $d^{-1}$ (shaded) and SST in C° (contours). The black box indicates the OTREC flight box. b-f) Vertical cross sections of vertical motion in Pa $s^{-1}$ across 89°W-86°W from OTREC dropsondes and the four analyzed reanalyses (ERA5, MERRA-2, JRA-55, and NCEP-NCAR) averaged over the nine RFs. ..... 84

Figure 4.2 Vertical cross sections of vertical motion in Pa $s^{-1}$ across 89°W-86°W during RF14 (21 September 2019), from a) OTREC dropsondes, b-d) GPM algorithms (SLH, CSH, and HS2018), and e-h) reanalyses. ..... 86

Figure 4.3 Vertical cross sections of vertical motion in Pa $s^{-1}$ across 89°W-86°W from a) OTREC dropsondes averaged over the 9 RF samples, b-d) GPM algorithms and e-h) reanalyses averaged over 42 day samples between 2014 and 2020..... 88

Figure 3.4 Distribution of vertical motion with height in Pa $s^{-1}$ at a) 4°N-7.5°N, b) 7.5°N-9°N and c) 9°N-10.5°N in the EP ITCZ based on Monte Carlo analysis using 42 samples between 2014 and 2020 from the GPM algorithms and reanalyses. Each set of points represent the minimum average, 25th percentile, mean, 75th percentile, and maximun average. The black profile shows the OTREC vertical velocity 9-day sample mean with standard error in gray lines. c) Sketch of the OTREC mean conditions of the meridional overturning circulation over the East Pacific ITCZ. The thin, thick, and thickest horizontal vectors indicate meridional winds smaller than 2 m $s^{-1}$, between 2 and 4 m $s^{-1}$, and larger than 4 m $s^{-1}$, respectively. The short double arrow indicates meridional winds around 0 m $s^{-1}$. ..... 91

Figure 5.1 a-b) Total precipitation from the TRMM/GPM radars (shaded, in mm $d^{-1}$) and topography (contours, in km) during AMJ (left panel) and JAS (right panel). c-d) Convective, stratiform and shallow precipitation from TRMM/GPM radars and e-f) omega cross section (shaded, in Pa $s^{-1}$) and meridional flow (arrows) from ERA5 across 7°W – 3°E (dashed lines in top figures) for each season. The vertical meridional flow component has been multiplied by 10 to account for the small ratio of the plot. Largest meridional wind vector is 5 m $s^{-1}$. The solid line at 5.5°N highlights the coastline. ..... 103

Figure 5.2 Total meridional wind (shaded) and the sea breeze (12 – 18 UTC, contours) and NLLJ (20 – 08 UTC, contours) anomalies in m $s^{-1}$ at 950 hPa (a and c), convergence (shaded) and sea breeze and NLLJ anomalies (contours) in $s^{-1}$ at 950 hPa (b and d). The dashed line at 5.5°N highlights the coastline. ..... 106

Figure 5.3 Latitude-time diagram at 950 hPa of divergence (a and g) in $s^{-1}$, vorticity (b and h) in $s^{-1}$, meridional wind (c and i) in m $s^{-1}$, zonal wind (d and j) in m

$s^{-1}$, temperature (e and k) in °C, and specific humidity (f and l) in g $kg^{-1}$ across 7°W-3°E during AMJ (left) and JAS (right). The solid line at 5.5°N highlights the coastline. .....108

Figure 5.4 Diurnal variation of vertical motion (Pa $s^{-1}$) and meridional flow cross sections across 7°W-3°E during AMJ. The vertical meridional flow component has been multiplied by 10 to account for the small ratio of the plot. Largest meridional wind vector is 5 m $s^{-1}$. The solid line at 5.5°N highlights the coastline. .....110

Figure 5.5 Same as fig. 5.5 but for JAS. .....111

Figure 5.6 Latitude-time diagram of vertical velocity at 400 hPa (shaded) and 850 hPa (contours) in Pa $s^{-1}$ (a and d), precipitation (shaded) and MFC (contours) in mm $d^{-1}$ from ERA5 (b and e), and convective (shaded), stratiform (black contours each 1 mm $d^{-1}$ starting at 2 mm $d^{-1}$), and shallow (blue contours each 0.5 mm $d^{-1}$ starting at 0.5 mm $d^{-1}$) precipitation in mm $d^{-1}$ from TRMM-GPM (c and f) during AMJ (left) and JAS (right). The solid gray line at 5.5°N highlights the coastline. .....115

Figure 5.7 Latitude-time diagram of a-b) convective (shaded) and large scale (contours) precipitation from ERA, and c-d) convective plus shallow (shaded) and stratiform (contours) precipitation from TRMM/GPM across 7°W-3°E during AMJ. Precipitation in mm $d^{-1}$. The solid gray line at 5.5°N highlights the coastline. .....119

Figure 5.8 Schematic of the diurnal variation of West African meridional overturning and convection during the pre-monsoon (left) and monsoon (right) season. The triangle indicates the location of the coastline. The thin, thick, and thickest horizontal (vertical) vectors indicate meridional winds (upward motion) smaller than 2 m $s^{-1}$ (-0.05 Pa $s^{-1}$), between 2 and 4 m $s^{-1}$ (-0.05 and -0.1 Pa $s^{-1}$), and larger than 4 m $s^{-1}$ (-0.1 Pa $s^{-1}$), respectively. Two (four) dashes under the convective cloud indicate precipitation smaller (larger) than 18 mm $d^{-1}$ during the pre-monsoon season and smaller (larger) than 13 mm $d^{-1}$ during the monsoon season. .....123

LIST OF TABLES

Page

Table 3.1 LCL (hPa), CAPE (J $kg^{-1}$), and CIN (J $kg^{-1}$) at 4°N and 8°N from the three EWs at day +0 and +2 from OTREC RFs and ERA5 ..... 60

Table 4.1 Reanalyses and GPM latent heating products ..... 82

# CHAPTER I

# INTRODUCTION

The tropics contain a complex range of atmospheric circulations that vary spatially and temporally. On the largest scale, there is deep meridional overturning in the Hadley Cell and deep zonal overturning in the Walker Circulation that are typically averaged over seasonal or longer time scales. Monsoons represent large shifts in regional circulations over seasonal time scales. Circulation features can also propagate across much of the tropics on intraseasonal to synoptic time scales, such as the Madden-Julian Oscillation and equatorially trapped waves. Diurnally varying circulations commonly occur near coasts in the form of the sea/land breeze and nocturnal low-level jets. These circulations all significantly impact tropical cloudiness and precipitation, and it is the goal of this dissertation to focus on the most relevant of these circulations and their interaction with convection in two regions: the East Pacific and West Africa.

In the East Pacific, organized cloud systems propagate eastward (e.g., Kelvin waves; Kiladis et al. 2009) or westward (easterly waves; Serra et al. 2008) at synoptic time scales (i.e., between 2 to 20 days). Some eastward disturbances with similar Kelvin wave zonal phase speed may be forced by extratropical Rossby waves (Straub and Kiladis 2003). Additionally, these propagating systems can interact with larger scales circulations such as the deep meridional circulation (DMC) and shallow meridional circulation (SMC) seen in the East Pacific intertropical convergence zone (ITCZ). While the DMC can be related to the Hadley Cell, the East Pacific SMC is driven by the

meridional sea surface temperature (SST) gradient that produces low-level convergence (Lindzen and Nigam, 1987) and latent heating from shallow convection (Huaman and Takahashi 2016, Huaman and Schumacher 2018).

Over West Africa, there is also a DMC related to monsoon convection and an SMC driven by the strong temperature gradient over the Sahel region. However, the West African SMC is dry and forced by sensible heating (Hagos et al. 2010). The convection over West Africa seems to be initiated by a sea-breeze front that propagates cloud systems onto land. Additionally, the nocturnal low-level jets (NLLJs) modulate shallow upward motion and low-level stratus clouds (Lohou et al 2020).

For my PhD research, I have separated my work into distinct studies of particular circulations over either the East Pacific or West Africa. However, my overarching goal is to understand the scale interactions at play over each region and how larger scale circulations (i.e., the DMC and SMC) interact with convective structures and ultimately the climatology of each region. The specific goals of this research are:

A. Identify and characterize eastward propagating disturbances, including Kelvin waves, and study their interaction with shallow and deep circulations over the East Pacific.
B. Study the interaction of easterly waves with larger scale shallow and deep circulations over the East Pacific and assess the "true" vertical velocity using field campaign, satellite and reanalysis data over the East Pacific.
C. Determine the diurnal variation of the meridional flow and rainfall over West Africa.

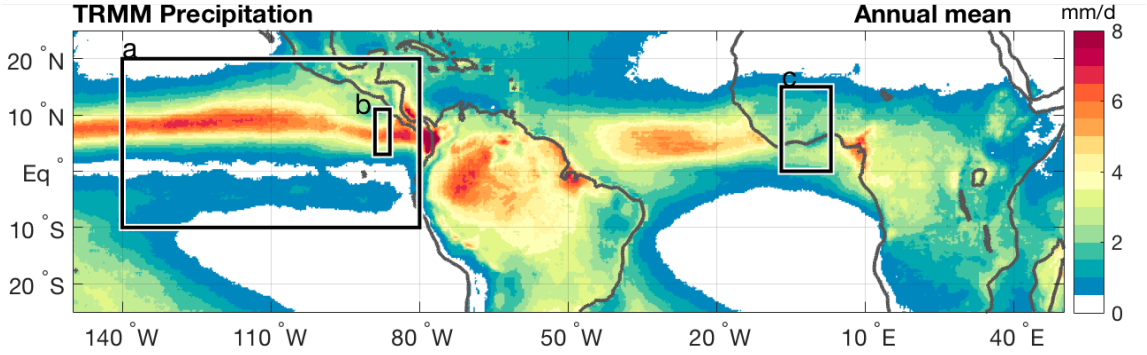


**Figure 1.1 Annual precipitation in mm/d from TRMM (1998-2010). Box a indicates the region to study eastward disturbances (Chapter 2), box b indicates the region of the OTREC field campaign (Chapters 3 and 4), and box c indicates the region to study the diurnal cycle of African convection (Chapter 5).**

The first part of this dissertation, as described in Chapter II, is the study of eastward propagating disturbances in the East Pacific (box a in Fig. 1.1). Eastward propagating disturbances have different physical characteristics and forcing mechanisms during boreal winter (DJF) and spring (MAM). Additionally, since the East Pacific is home to an SMC in addition to the deeper Hadley cell associated with deep ITCZ convection, I analyzed how the meridional overturning structure of the East Pacific is altered during the passage of eastward propagating disturbances.

The second and third part of this dissertation, found in Chapters III and IV, focus on the meridional overturning structure in the East Pacific using the Organization of the Tropical East Pacific Convection (OTREC) field campaign (box b in Fig. 1.1). In this part of my PhD research, I explored how the DMC and SMC are modified during the passage of westward propagating easterly waves (Chapter III). Additionally, the vertical velocity associated with the shallow and deep meridional circulation is assessed using OTREC field campaign, reanalysis, and satellite datasets to determine which product is

closer to the OTREC observations and thus more likely to represent the true meridional overturning structure in the East Pacific ITCZ (Chapter IV).

The diurnal variation of the meridional flow and rainfall over West Africa during the pre-monsoon and monsoon seasons is presented in Chapter V. Using the most recent, high-resolution reanalysis data and satellite precipitation observations, I characterize the diurnal variation of West African precipitation and low-level winds emanating from the Gulf of Guinea coast. Finally, Chapter VI contains the conclusions and a summary of all the presented results.

# CHAPTER II

# EASTWARD-PROPAGATING DISTURBANCES IN THE TROPICAL PACIFIC*

## 2.1. Background

Convection in the ITCZ occurs on many time and space scales, from localized cells lasting an hour or less to widespread convective activity ebbing and flowing over many weeks. An important subset of this convective variability can be characterized as eastward propagating disturbances (EPDs) occurring at synoptic time scales (i.e., on the order of a few days to two weeks) with eastward phase propagation. Kelvin waves can be considered one of the dominant synoptic scale convective modes in the Pacific basin (Huang & Huang, 2011; Roundy & Frank, 2004; Straub & Kiladis, 2002). The Kelvin wave is a solution of the shallow water equations on an equatorial beta plane (Matsuno, 1966). Convectively coupled Kelvin waves propagate eastward along the ITCZ and arise from the interaction between dry Kelvin waves and moist convective processes (Straub & Kiladis, 2003). Although Kelvin waves propagate at around 12 to 15 m $s^{-1}$, a particular phase speed itself is not proof that an EPD is a Kelvin wave. Rather, the large-scale kinematic and thermodynamic perturbations associated with an EPD should be consistent with the Kelvin wave solution from the shallow water equations (Kiladis et al., 2009).

---

* A version of this chapter was published as "Eastward-propagating disturbances in the tropical Pacific" in *Monthly Weather Review* by Huaman, Lidia, C. Schumacher, and G. Kiladis, 2020. 

Extratropical Rossby waves play a potentially important role in forcing tropical convection (Ortega et al., 2018; Stan et al., 2017). In relation to the Pacific basin, Straub and Kiladis (2003) reported that extratropical Rossby waves originating in the Southern Hemisphere (SH) can initiate Kelvin waves in the tropical west Pacific in boreal summer by inducing upper tropospheric divergence and vertical motion as the Rossby waves propagate into the tropics. Liebmann et al. (2009) showed that some Kelvin waves over South America are initiated by SH extratropical Rossby waves in boreal winter. Kiladis and Weickmann (1992, 1997) and Kiladis (1998) found that Northern Hemisphere (NH) extratropical Rossby waves enhance local cloudiness with eastward propagation in the vicinity of the central and east Pacific ITCZ during boreal winter; however, these disturbances did not appear to correspond to Kelvin waves.

The Kelvin wave signal in the tropical Pacific is minimum during boreal winter (Roundy & Frank, 2004) and much stronger in boreal spring (Baranowski et al., 2016). The weaker Kelvin wave signal in DJF could be due to the intensification of the east Pacific cold tongue that inhibits convection around the equator along with the weak SH wave Rossby wave activity, limiting Kelvin wave initiation in the west Pacific. However, the relationship between NH extratropical Rossby waves and Kelvin waves (and eastward disturbances more generally) in the tropical Pacific remains understudied for boreal winter and is virtually unstudied for boreal spring.

The east Pacific is home to an SMC in addition to the deeper Hadley cell associated with deep ITCZ convection (Trenberth et al., 2000; Zhang et al., 2004; 2008). The meridional overturning circulation in the east Pacific ITCZ is dominated by a shallow circulation in the southern part of the ITCZ and a deep circulation in the northern part of the ITCZ (Huaman & Takahashi, 2016; Huaman & Schumacher, 2018). The SMC exists year- round in the east Pacific, but is more dominant in DJF compared to MAM because of the existence of the double ITCZ north and south of the equator during boreal spring. The vertical structure of a Kelvin wave is tilted in the zonal direction, with maximum low-level convergence ahead of the Kelvin wave and maximum upper tropospheric zonal divergence behind the location of low-level convergence (Kiladis et al., 2009). Straub and Kiladis (2002) reported that Kelvin wave propagation in the east Pacific evolves from shallow congestus clouds to organized deep convective features. Thus, there is a likelihood that the meridional overturning structure in the east Pacific may be altered during the passage of EPDs, including Kelvin waves.

This study analyzes the characteristics and extratropical forcing of EPDs in the tropical Pacific during boreal winter (DJF) and spring (MAM), as well as associated variations in the meridional overturning circulation in the east Pacific. Brightness temperature ($T_b$) for cloud properties, satellite precipitation for convective intensity, and reanalysis data for dynamical fields were used; and DJF and MAM are focused due to the strong NH wave activity during these seasons.

## 2.2. Data and Methodology

Daily $T_b$ with a resolution of 0.5° x 0.5° from Cloud Archive User Services (CLAUS) was used, which utilizes geostationary and polar-orbiting images (Hodges et al., 2000), for the period 1984-2016. Daily precipitation from the Tropical Rainfall Measuring Mission (TRMM) product 3B42 (Huffman et al., 2007) with a resolution of 0.5° x 0.5° for the period 1998-2016 was also used to quantify precipitation. In addition, this study utilized daily wind, geopotential height, omega and temperature fields interpolated to a resolution of 2.5° x 2.5° from the Modern-ERA Retrospective analysis for Research and Applications V2 (MERRA2) reanalysis (Bosilovich et al., 2015) for the period 1984-2016 to characterize the atmospheric circulation associated with the EPDs and meridional overturning circulation. Huaman and Schumacher (2018) showed that MERRA2 better reproduces the east Pacific atmospheric conditions compared to other commonly used reanalyses, especially with respect to the complex vertical structure of convection observed by satellite.

Daily $T_b$ anomalies were calculated by removing the first three harmonics, which represent the seasonal cycle. Frequency-wavenumber diagrams from Wheeler and Kiladis (1999) were then calculated for the central and east Pacific. This study is focused on high-frequency variability, so successive overlapping (by 2 months) 64-day windowed segments is used to allow a smooth Kelvin signal distribution while excluding much of the intraseasonal signal associated with the Madden-Julian Oscillation (MJO). From the frequency-wavenumber diagram, $T_b$ signal with a period between 2.5 and 20 days and wavenumbers equal to and greater than +1 using Fourier filters is retained

(Figs. 2.1a and b). The result is called the eastward band $T_b$ and includes the Kelvin-band signal.

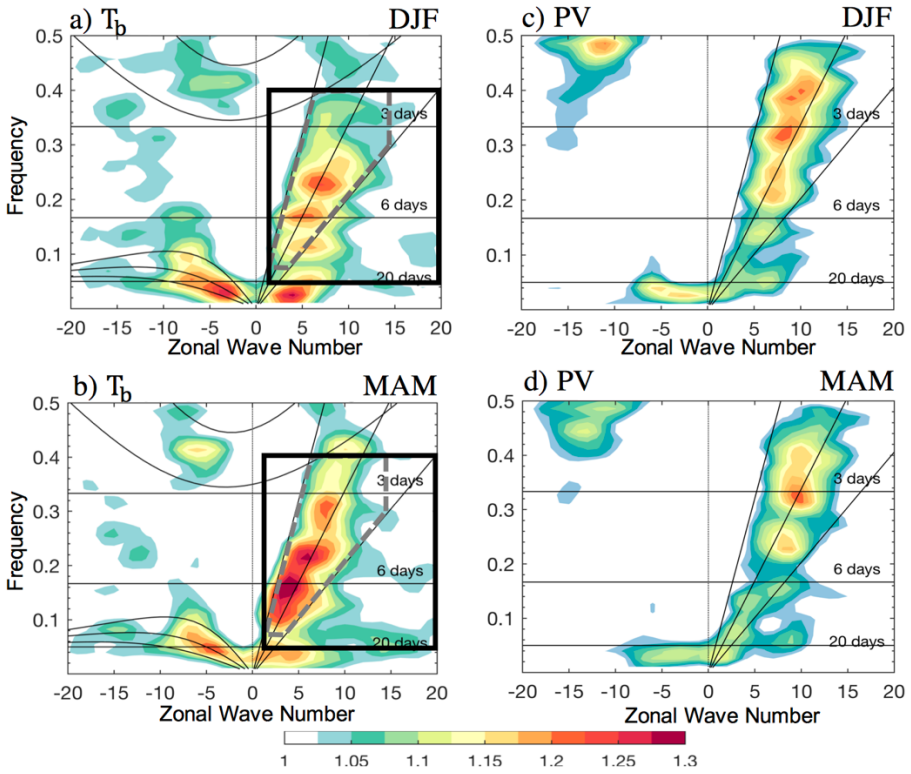


**Figure 2.1 Wavenumber-frequency power spectrum (from 120°E-60°W) of the symmetric component of Tb summed from 15°S to 15°N for 1984-2016 for a) DJF and b) MAM. Thin black lines represent the dispersion curves for CCEWS. Heavy dashed gray and solid black boxes represent regions of Kelvin-band and east-band filtering, respectively. Wavenumber-frequency power spectrum (from 120°E – 60°W) of total PV summed from 20°N to 50°N for c) DJF and d) MAM.**

The eastward band $T_b$ was used to identify and characterize EPDs. Empirical orthogonal functions (EOFs) for DJF and MAM were used to isolate the maximum local eastward wave variance over the Pacific region from 15°S-20°N and 180°W-80°W (similar results were obtained when the spatial domain to 150°W-85°W was slightly decreased). In all cases the leading modes occur as pairs of EOFs, the combination of

which represent eastward propagating features. The total dynamic fields against the first principal component (PC) time series at different lags and levels were regressed for the two seasons to obtain the statistical behavior of each mode. A similar regression technique using a base point $T_b$ instead of EOFs was also applied by Straub and Kiladis (2003) to characterize extratropical forcing of Kelvin waves by SH Rossby waves.

The linear regression results based on PC 1 were scaled to a 12°C anomaly in $T_b$ at the basepoint on day 0, a typical value for an eastward propagating event. It is worth mentioning that the standard deviation (variance) of the filtered $T_b$ is around 9.5°C (90 $°C^2$) at 130°W at the latitude of the ITCZ (7.5°N) during DJF and MAM. The statistical significance of these results was calculated based on a local two-sided significance test, which takes into account the correlation coefficients and a reduced number of degrees of freedom based on the decorrelation timescale (Livezey & Chen, 1983). Results were considered significant at the 95% level or greater.

## 2.3. EPDs in the tropical Pacific

### *2.3.1. Mean state conditions*

Figure 2.2 shows a hovmöller from December 2007 to May 2008 of the $T_b$ anomaly from 2.5°N to 10°N overlain by the eastward band $T_b$ in contours. EPDs are evident in both boreal winter (DJF) and spring (MAM) in the Pacific basin. During MAM, EPDs propagate from the west Pacific through the east Pacific at around 15 m $s^{-1}$, such as the event on 27 March, consistent with Kelvin wave phase speeds and lifetimes (Straub & Kiladis, 2002). Additional EPDs are shown during DJF that initiate in the

central Pacific and have phase speeds between 10 to 13 m $s^{-1}$, such as the event on 1 January. These waves are slower and shorter lived than the MAM waves, which suggests that they may be different phenomena.

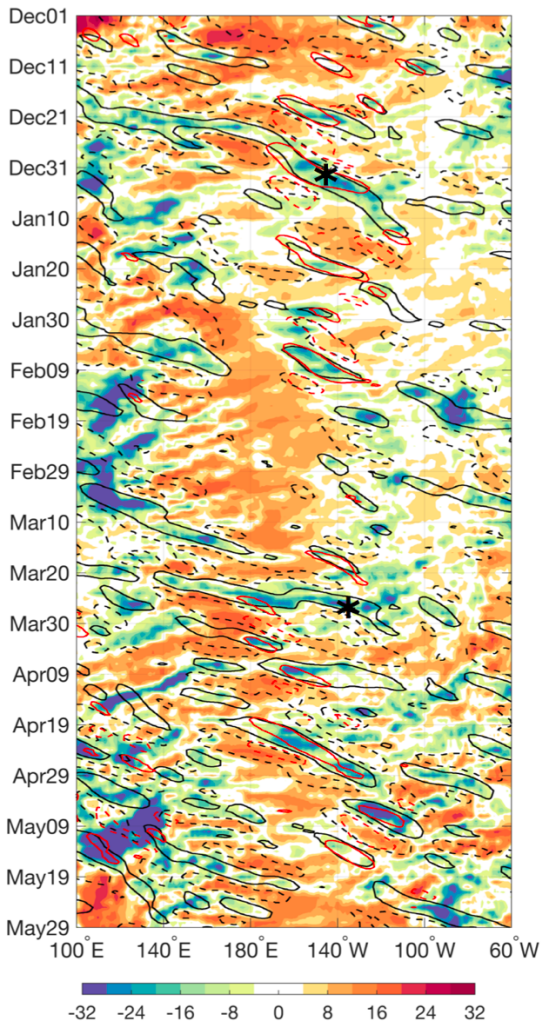


**Figure 2.2 Hovmöller diagram of $T_b$ anomalies (shaded) and eastward 2.5-20-day band $T_b$ (contours; 5°C solid, - 5°C dashed) in °C along 2.5°-10°N from Dec 2007 to May 2008. The stars show two EPD events on 1 January and 27 March.**

The left panels in Fig. 2.1 show the climatological wavenumber-frequency power spectrum of $T_b$ across the tropical Pacific (from 120°E – 60°W and 15°S – 15°N) for DJF and MAM. While both seasons exhibit significant power in the eastward band $T_b$ region (solid box), the Kelvin wave signal (dashed region) is weaker in DJF compared to MAM. A wavenumber-frequency diagram of potential vorticity (PV) in the extratropical Pacific (from 120°E – 60°W and 20°N – 50°N) is shown in the right panels of Fig. 2.1 for DJF and MAM. Extratropical Rossby wave activity is well represented by PV, which is approximately conserved (Bluestein 1992) and frequently propagates into the tropics over the central and eastern Pacific (Kiladis & Weickmann, 1992, 1997; Kiladis, 1998; Tomas & Webster, 1994). While Kelvin waves are equatorially trapped and cannot be present at this latitude range, a strong eastward PV signal in the 2.5-20-day band is evident during both seasons, with power concentrated at higher zonal wavenumbers than in Kelvin waves. Thus, Figs. 2.1c and d show that Rossby waves propagate eastward in the NH extratropics with a similar phase speed as Kelvin waves. This strong signal is also seen in the wavenumber-frequency diagram of meridional wind and at a range of latitudes bands extending from the extratropics into the tropics (not shown).

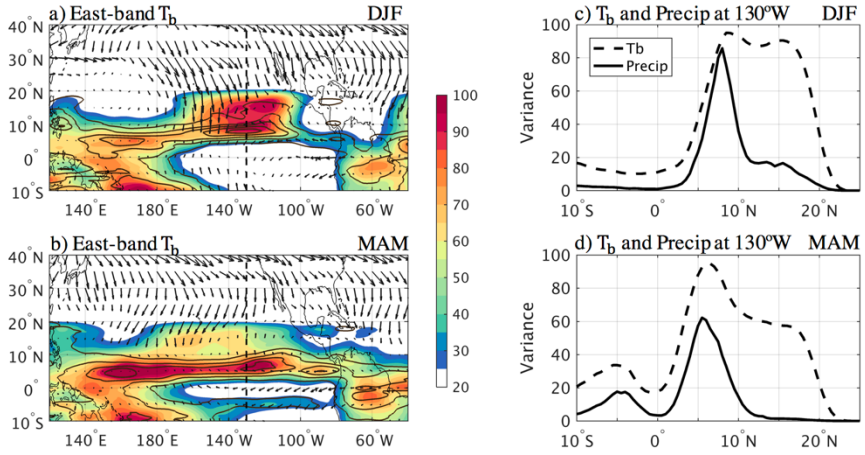


**Figure 2.3 Climatological eastward 2.5-20-day band $T_b$ (1984-2016, shaded) and precipitation (1998-2016, contours) variance in °C$^2$ and mm$^2$ d$^2$, respectively, and 30-day high-pass-filtered E-vectors (1984-2016) in m$^2$ s$^{-2}$ for a) DJF and b) MAM. Precipitation contour interval is 15 mm$^2$ d$^{-2}$, $T_b$ values poleward of 20°N are masked out. Meridional cross sections at 130°W of $T_b$ and precipitation variance for c) DJF and d) MAM.**

The left panels of Fig. 2.3 show the geographical distribution of the eastward band $T_b$ and precipitation variance over the tropical Pacific for DJF and MAM. To focus on the tropical distribution of $T_b$ and precipitation, values poleward of 20°N were masked out. The 30-day high-pass-filtered E-vectors at 200 hPa (Hoskins et al., 1983) are also plotted. The E-vector is calculated as $\overline{v'^2 - u'^2}, -\overline{u'v'}$, where $u$ and $v$ are the zonal and meridional wind, respectively. The primes represent 30-day high-pass fluctuations and the bars represent seasonal averages. E-vectors provide a qualitative measure of the amplitude and direction of propagation of upper tropospheric extratropical wave activity and point in the approximate direction of the group velocity of a wave packet (Hoskins et al., 1983; Kiladis, 1998; Straub & Kiladis, 2003)

In the north Pacific during DJF (Fig. 2.3a), the E-vectors point southeastward indicating that the preferred path of extratropical Rossby wave energy is equatorward into the central and eastern tropical Pacific. The eastward band $T_b$ variance (from 1984-2016) shows lower values in the west Pacific and two relative maxima in the east Pacific at 7.5°N and 17°N. While the eastward band precipitation variance (from 1998-2016) also shows lower values in the west Pacific, there is only one peak in the east Pacific at 7.5°N. This structure is similar when considering the same time range (from 1998-2016) for $T_b$ and TRMM rainfall (not shown). Figure 2.3c shows a meridional cross section of the variance of the eastward band precipitation and $T_b$ at 130°W. Precipitation variance is large in the ITCZ at 7.5°N, but drops off rapidly on either side of the ITCZ. $T_b$ variance also peaks at 7.5°N, but remains large until its second peak at 17°N. Figures 2.3a and c suggest that extratropical perturbations modulate high-cloud structure (and to a lesser extent rainfall) north of the ITCZ up to 20°N during DJF. This result is consistent with (Kiladis, 1998), who proposed that the intrusion of positive PV associated with extratropical Rossby wave perturbations into low latitudes modulates cloudiness and vertical motion in the vicinity of the ITCZ during DJF.

During MAM (Fig. 2.3b), a large eastward band $T_b$ and precipitation signal exists in the west Pacific and may be mostly accounted for by the Kelvin band (Fig. 2.1b). Eastward band $T_b$ and precipitation variance remains strong north of the equator as Kelvin waves propagate eastward from the west Pacific into the east Pacific. A much weaker secondary maximum occurs south of the equator, extending into the southern ITCZ over the easternmost Pacific. The meridional precipitation variance cross section

at 130°W (Fig. 2.3d) shows a double ITCZ at 5°S and 7.5°N. The double ITCZ is also evident in the eastward band $T_b$, and while there is some $T_b$ variance poleward of the northern branch of the ITCZ, the signal is not as strong as in DJF (Fig. 2.3c). The E-vectors in the north Pacific during MAM (Fig. 2.3b) point mainly southwestward, indicating that Rossby wave perturbations in the subtropical jet tend to propagate equatorward into the west and central tropical Pacific.

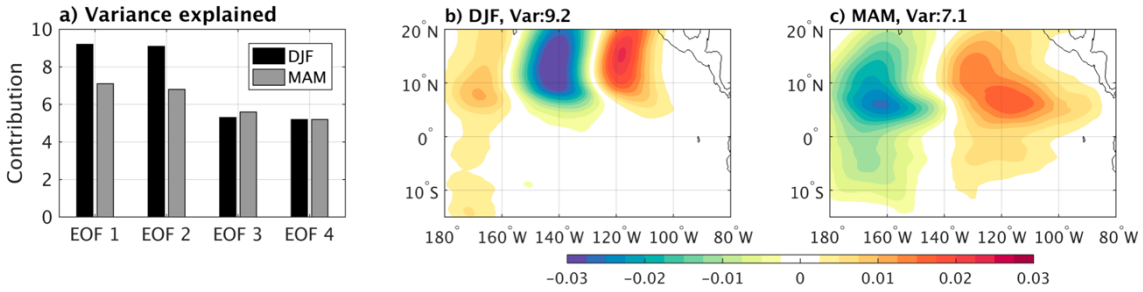


**Figure 2.4 a) Contribution of variance explained by the first four EOFs for both seasons. First EOF of eastward 2.5-20-day band $T_b$ for b) DJF and c) MAM.**

*2.3.2. Horizontal structure of eastward 2.5-20-day band regressions*

To examine the horizontal structure of EPDs in the Pacific region, EOFs of eastward band $T_b$ were used to isolate the leading modes of EPDs over the central and east Pacific (180°W-80°W, 15°S-20°N). Figure 2.4a shows the contribution of the first four EOFs for DJF and MAM. The leading EOF pairs explain 15.4% and 11.2% in DJF and MAM, respectively. Additionally, the leading EOF pair maps are orthogonal and the cross correlation between PC1 and PC2 reach up to 0.8 (not shown). Therefore, results based on EOF1 are similar to those based on EOF2 and the leading EOFs will be focused in the remainder of this study. During DJF (Fig. 2.4b), EOF1 suggests an

eastward wave that propagates at 15°N with a local zonal wavenumber of about 7. Minima (maxima) in $T_b$, which suggest wet (dry) conditions, are observed at 140°W (115°W). This EPD propagates zonally well to the north of the main axis of the ITCZ through the strongest region of extratropical Rossby wave activity (Fig. 2.3a). During MAM (Fig. 2.4c), the EPD suggested by EOF1 propagates at 7.5°N, which is along the climatological ITCZ axis, and has a local zonal wavenumber of around 4. Wet (dry) conditions are observed at 160°W (120°W). The $T_b$ signal extends across the equator and shows an enhanced secondary signal around 5°S consistent with the double ITCZ structure during boreal spring.

In order to characterize the large-scale atmospheric circulation associated with EPDs, the total $T_b$, TRMM precipitation, winds, geopotential height, and streamfunction fields are regressed onto PC1. Figure 2.5 shows the regressed structure during DJF at 850 and 200 hPa at different lag days. At day -4 (Fig. 2.5a), a positive $T_b$ perturbation is seen at 140°W with a weak negative $T_b$ perturbation at 160°W. The negative $T_b$ perturbation propagates along 15°N to 155°W at day -2 and to 140°W at day 0 (Figs. 2.5b and c), consistent with Fig. 2.4b. The 850-hPa geopotential height and wind signal is weak over the equatorial region with values under 10 m and 2 m $s^{-1}$, respectively. At 200 hPa (Figs. 2.5e-h), a Rossby wave train is seen in the central Pacific propagating southeastward. The negative $T_b$ signal is associated with the southwesterly flow ahead of the Rossby wave trough, consistent with Fig. 2.3a. This interaction was well documented in (Kiladis & Weickmann, 1992) and (Kiladis, 1998). A comparison between $T_b$ in shading and TRMM precipitation (for the period 1998 - 2016) in thick contours shows

that, while the rainfall signal is concentrated within the ITCZ, the $T_b$ signal with its center further north is primarily associated with high cloudiness. The divergence at 200 hPa at day 0 is shown in Fig. 2.7a and the high cloudiness is associated with the positive upper level divergence and southerly winds on the trough side of the Rossby wave. This structure is also seen at other lags (not shown).

A more complex structure associated with EPDs is seen during MAM (Fig. 2.6). At day -4 (Figs. 2.6a and e), a negative $T_b$ signal is located close to the equator in the west Pacific but is then displaced off the equator as it propagates eastward along the ITCZ axis at 7.5°N at later lag days. At day -2 (Fig. 2.6b), the 850-hPa geopotential height field has a center at the equator with values up to 20 m, with a primarily zonal wind field in phase with the geopotential as in a theoretical Kelvin wave (Matsuno, 1966). Dynamical fields centered on the equator accompanied by off equatorial convective signals are also seen for convectively coupled Kelvin waves during boreal summer (Straub & Kiladis, 2002, 2003). At day 0 (Fig. 2.6c), the 850-hPa wind convergence peaks around 145°W, ahead of the strongest negative $T_b$ signal at 160°W. This structure is consistent with the description of Kelvin waves in (Kiladis et al., 2009).

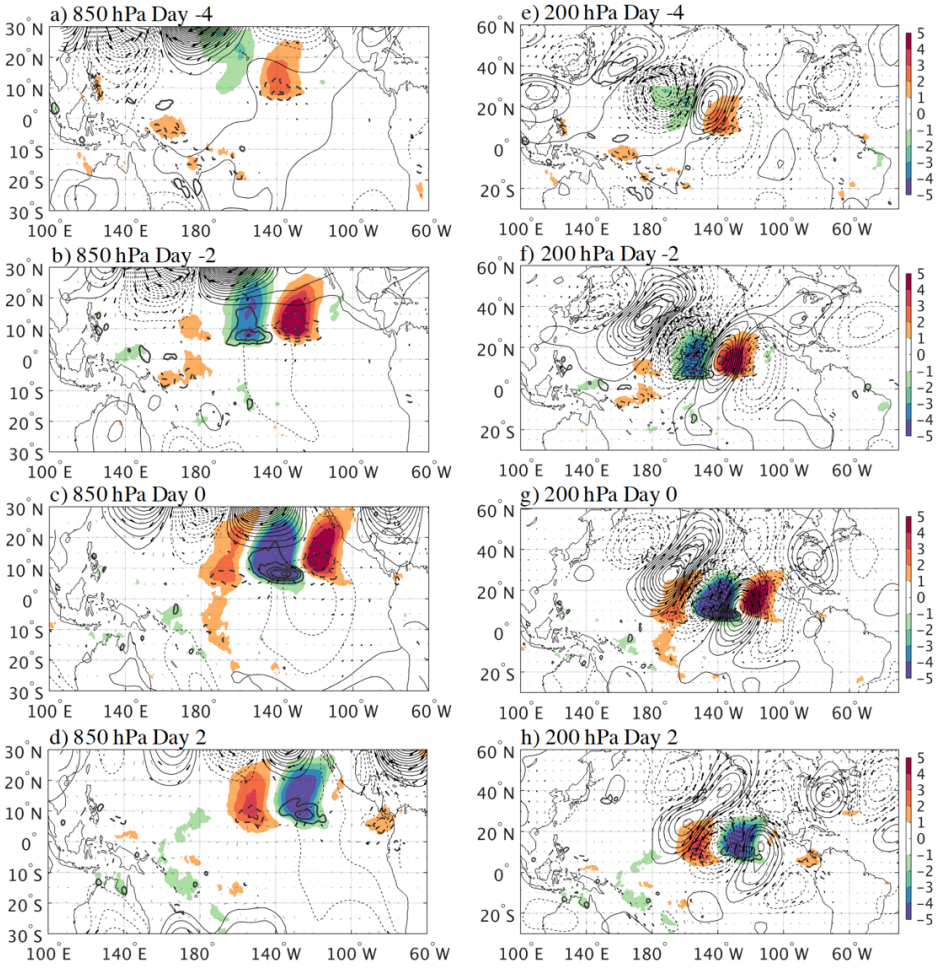


**Figure 2.5 Regressed values of a-d) $T_b$ in °C (shading), geopotential height in m (contours), precipitation in mm $d^{-1}$ (thick contours) and winds (vectors) at 850 hPa, and e-h) streamfuction in $m^2$ $s^{-2}$ (contours) and winds (vectors) at 200 hPa, based on PC1 at different lag days during DJF. Panels e-h are on a different spatial scale than panels a-d. Geopotential height (streamfunction) contour interval is 4 m (2 ×$10^5$ $m^2$ $s^{-1}$), precipitation contour interval is 1 mm $d^{-1}$. Locally significant winds are shown in bold vectors, with the largest vector around 3 m $s^{-1}$.**

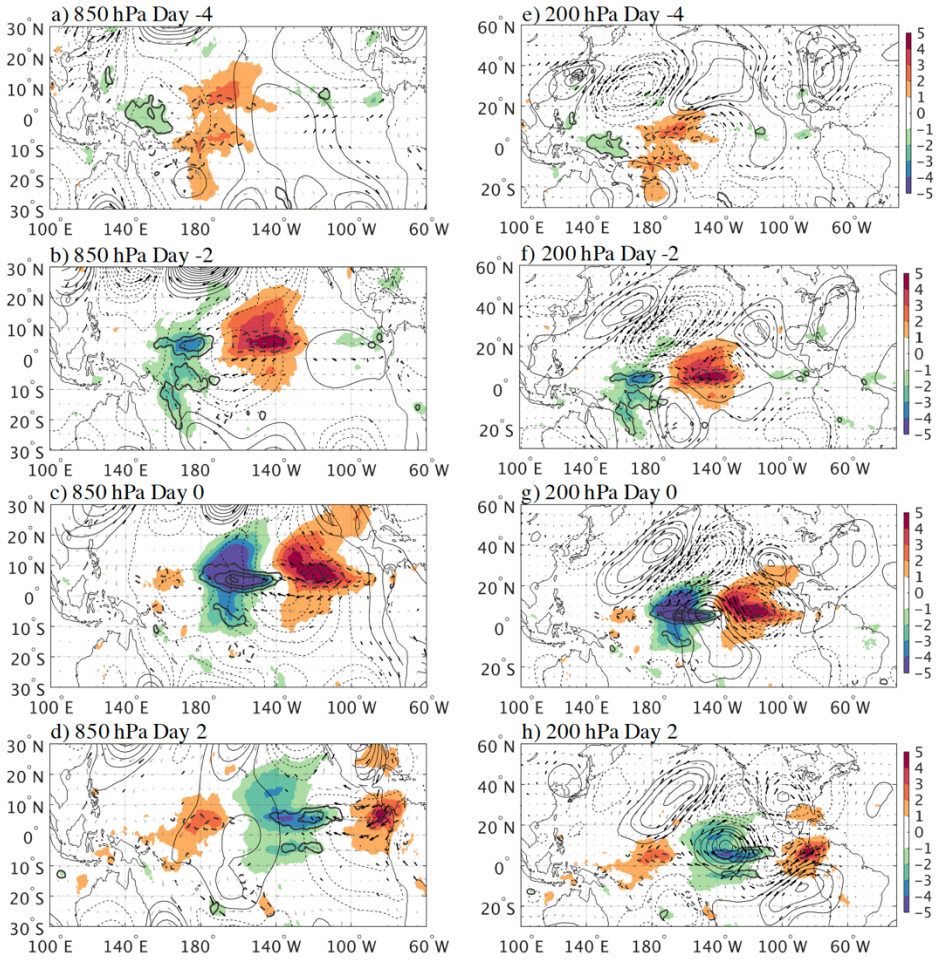


**Figure 2.6 Same as Fig. 2.5 but for MAM.**

Figure 2.6 also indicates enhancement of negative $T_b$ at 15°N, similar to the EPDs observed during DJF. As in DJF, a comparison with TRMM precipitation (in contours) shows that this $T_b$ enhancement is primarily associated with non-precipitating high cloudiness and at 200 hPa (Figs. 2.6e-h), a Rossby wave train appears to modulate the negative eastward $T_b$ perturbations at 15°N. However, the Kelvin wave at 7.5°N and EPD at 15°N occur at the same longitudes during MAM and can potentially interact. This extratropical-tropical connection is most clear at days -2 and 0 (Figs. 2.6f and g),

when the upper level cyclonic circulation on the trough side of the Rossby wave interacts with the upper level equatorial westerly winds between the convective and nonconvective part of the Kelvin wave around 160°W. This pattern also induces strong upper level divergence in the Kelvin wave at 7.5°N at day 0 (Fig. 2.7b). At day +2, the Kelvin wave modulates precipitation in the double ITCZ at 5°S and 5°N (Fig. 2.6d).

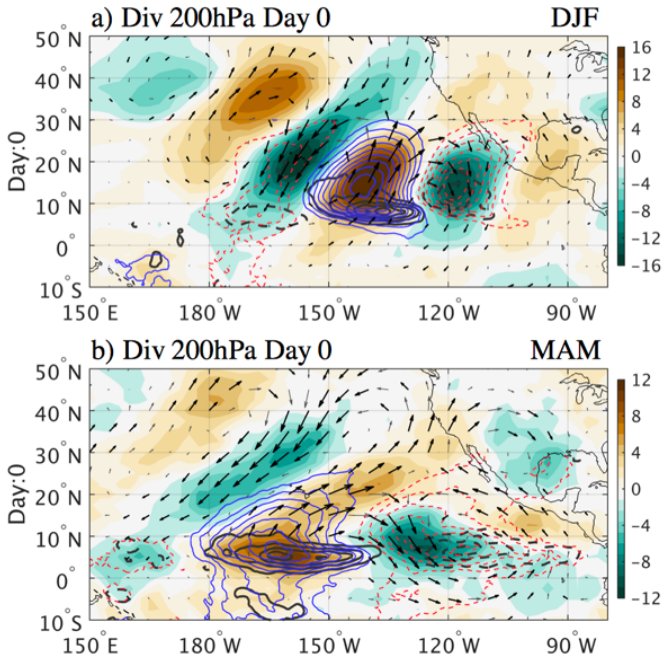


**Figure 2.7 Regressed values of $T_b$ in °C (contours), 200-hPa divergence in $s^{-1}$ (shaded) and winds in $10^{-6}$ m $s^{-1}$ (vectors) at lag day 0 for a) DJF and b) MAM. $T_b$ contour interval is 1°C. Locally significant winds are shown in bold vectors, with the largest vector around 3 m $s^{-1}$.**

To synthesize the propagation characteristics of eastward disturbances and their associated extratropical forcing during DJF and MAM, Fig. 2.8 shows the time-longitude diagram of regressed $T_b$ and 200-hPa streamfunction from 2.5°N to 12.5°N for both seasons. During DJF (Fig. 2.8a), the eastward wave covers less longitudinal extent

than MAM so it was label as a "short-lived EPD" (see also Fig. 2.2). A positive (negative) 200-hPa streamfunction perturbation is located ahead (behind) the minimum $T_b$, consistent with Fig. 2.5 and the forcing of short-lived EPDs from the extratropics. The NH Rossby wave propagation estimated from the 200-hPa streamfunction has a similar phase speed (10 m $s^{-1}$). During MAM (Fig. 2.8b), the $T_b$ signal propagates eastward at 15 m $s^{-1}$, consistent with a Kelvin wave; however, the NH Rossby wave estimated from the 200-hPa streamfunction still propagates at 10 m $s^{-1}$ and the streamfunction signal does not precede the $T_b$ minimum as in DJF. This indicates that while extratropical Rossby waves may not initiate Kelvin waves, they may strengthen their convective signal by causing upper-level divergence in the pre-existing Kelvin wave (Fig. 2.7b).

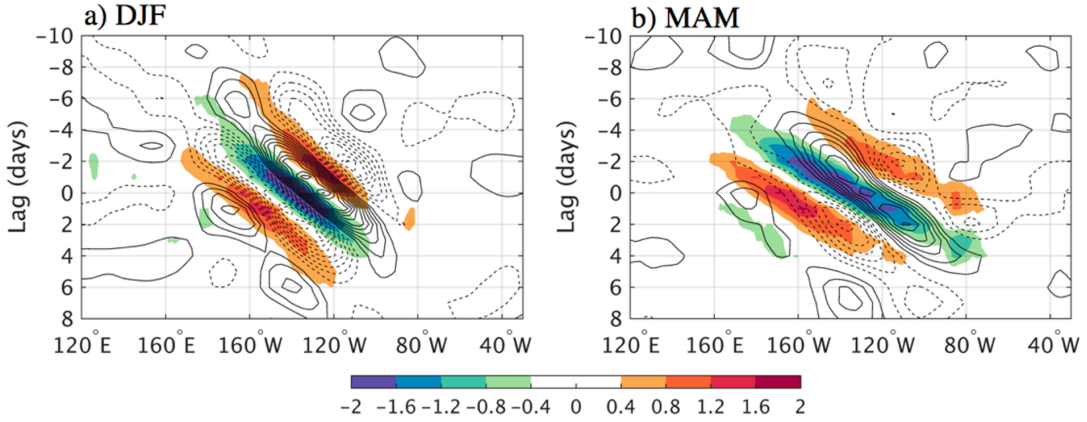


**Figure 2.8 Longitude-time diagram of regressed $T_b$ in °C (shading) and 200-hPa streamfunction in $m^2$ $s^{-1}$ (contours), averaged from 2.5°N to 12.5°N from day -10 to day 8. Contour interval is 1 ×$10^5$ $m^2$ $s^{-1}$ with positive (negative) values in solid (dashed) contours.**

To see if our regression-based results are consistent with the occurrence and evolution of individual Kelvin events, 42 case studies of EPDs (i.e., eastward 2.5-20-day $T_b$ larger than 1.25 standard deviation) were identified that propagate at 15 m $s^{-1}$ from the west Pacific to east Pacific for at least five days in MAM in the east Pacific from 1984-2016. While ten of these EPDs propagated across the tropics without interacting with NH extratropical Rossby waves, 32 were associated with extratropical forcing (i.e., negative geopotential height anomaly intrusion into the tropics on the trough side of the extratropical Rossby wave). Eleven of these 32 EPDs were excited from NH extratropical Rossby waves in the central Pacific, similar to what it was postulated in DJF. These short-lived EPDs were sometimes as fast as Kelvin waves. However, the other 21 EPDs were Kelvin waves that initiated in the Indian Ocean, Maritime Continent or west Pacific. As these Kelvin waves moved eastward, they interacted with an extratropical Rossby wave in the central and east tropical Pacific. It is worth mentioning that most of the ten EPDs that do not interact with the NH extratropical Rossby waves seem to be initiated or strengthen by the SH extratropical Rossby waves in the west and central Pacific as suggested by (Straub & Kiladis, 2003).

### *2.3.3. Vertical structure of eastward 2.5-20-day band regressions*

In this section, the vertical structure of the short-lived EPDs is examined in DJF and Kelvin waves in MAM. The time-height cross section of zonal wind anomalies from the equator to 10°N at 140°W for DJF is shown in Fig. 2.9a. At 200 hPa, the zonal wind anomalies reflect the Rossby wave train, such that the anomalous westerlies at day 0

correspond to the wave trough, which also supports the northerly flow seen in Fig. 2.5g. Similarly, the upper level anomalous easterly flow at day -5 corresponds to the Rossby wave ridge (Fig. 2.5e). These features tilt upward and eastward with height. The zonal wind anomaly cross section for MAM at 160°W (Fig. 2.9b) tilts westward with height and corresponds closely to a Kelvin wave structure, with low-level convergence and upper level divergence around day 0 (Kiladis et al., 2009; Straub & Kiladis, 2002). The upper level anomalous westerly flow at day -2 is strengthened as a result of the interaction of the Kelvin wave and trough of the extratropical Rossby wave. Thus, the zonal wind vertical structure of the two types of eastward disturbances further differentiate them from one another.

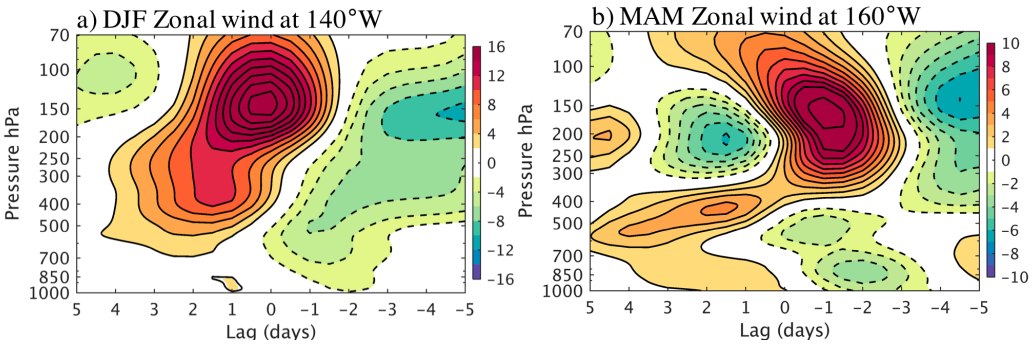


**Figure 2.9 Time-height cross sections of zonal wind in m $s^{-1}$ from the equator to 10°N for a) DJF at 140°N and b) MAM 160°N.**

Extratropical Rossby wave propagation into the tropics is associated with the intrusion of high PV into low latitudes (Kiladis & Weickmann, 1992; Tomas & Webster, 1994). The left panels of Fig. 2.10 show 200-hPa PV at different lag days during DJF overlain by 200-hPa wind vectors and $T_b$ and TRMM precipitation contours, while the

right panels show the meridional circulation at 140°W for each lag day. At day -3 (Fig. 2.10a), the minimum $T_b$ is at 160°W and is located east of the Rossby wave trough (i.e., positive PV) with upper tropospheric southerly flow. It is interesting to note that the Rossby wave trough is tilted southwest-northeast, therefore the $T_b$ is also tilted in this direction, especially at later lag days. At 140°W, positive $T_b$ occurs with negative PV and peaks at 12.5°N. Descending motions predominate (Fig. 2.10d), while weak ascending motion at 25°N is associated with the tilted Rossby wave trough and upper level divergence (not shown). As the EPD progresses eastward from day -3 to day -1, the minimum $T_b$ shifts to 145°W (Fig. 2.10b). While the rainfall signal is concentrated within the ITCZ, the $T_b$ signal with its center further north is primarily associated with high cloudiness. Strong ascending motion in the mid- to upper troposphere is seen between 15°N and 25°N in the 140°W cross section (Fig. 2.10e), along with a strong southerly flow associated with the Rossby wave trough. Ascending motion is relatively weak at low levels. This region is dominated by mid-level convergence and lower and upper level divergence (not shown), which is consistent with a stratiform rain structure (Mapes & Houze, 1995).

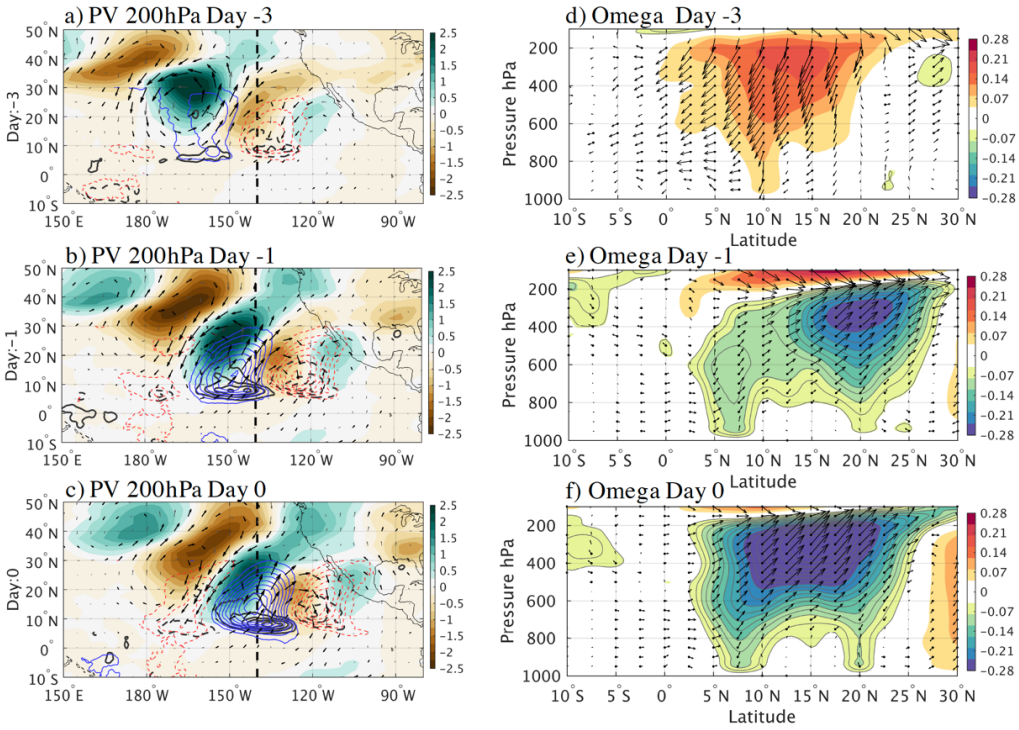


**Figure 2.10 Regressed values of a-c) $T_b$ in °C (blue and red contours), TRMM precipitation in mm $d^{-1}$ (gray contours), potential vorticity in PV units ($10^{-6}$ $m^2$ $s^{-1}$ K $kg^{-1}$, shaded) and winds in m $s^{-1}$ (vectors) at 850 hPa, and d-f) pressure-latitude cross sections of omega in Pa $s^{-1}$ and meridional flow (vertical velocity is amplified 15 times for better illustration), based on PC1 at different lag days during DJF. $T_b$ contour interval is 1°C. Locally significant winds are shown in bold vectors, with the largest vector around 3 m $s^{-1}$.**

At day 0 (Fig. 2.10c), the short-lived EPD has a negative $T_b$ peak at 140°W and propagates along 15°N, several degrees north of the climatological ITCZ where the regressed TRMM precipitation signal maximizes (i.e., at 7.5°N). The positive PV advection associated with the trough side of the extratropical Rossby wave enhances upward motion throughout the troposphere in the vicinity of the climatological ITCZ and to its north (Fig. 2.10f), although the maximum upward motion is still confined to upper levels and this drives the cloudiness signal as reflected in the $T_b$ field. The climatological

ITCZ in the east Pacific during DJF has a bottom-heavy structure with maximum vertical motion at 850 hPa (Huaman & Schumacher, 2018). This analysis shows that the mid-level forcing from the NH Rossby wave trough enhances ITCZ precipitation and suggests that the convection in the ITCZ evolves from shallow to deep during the passage of short-lived EPDs.

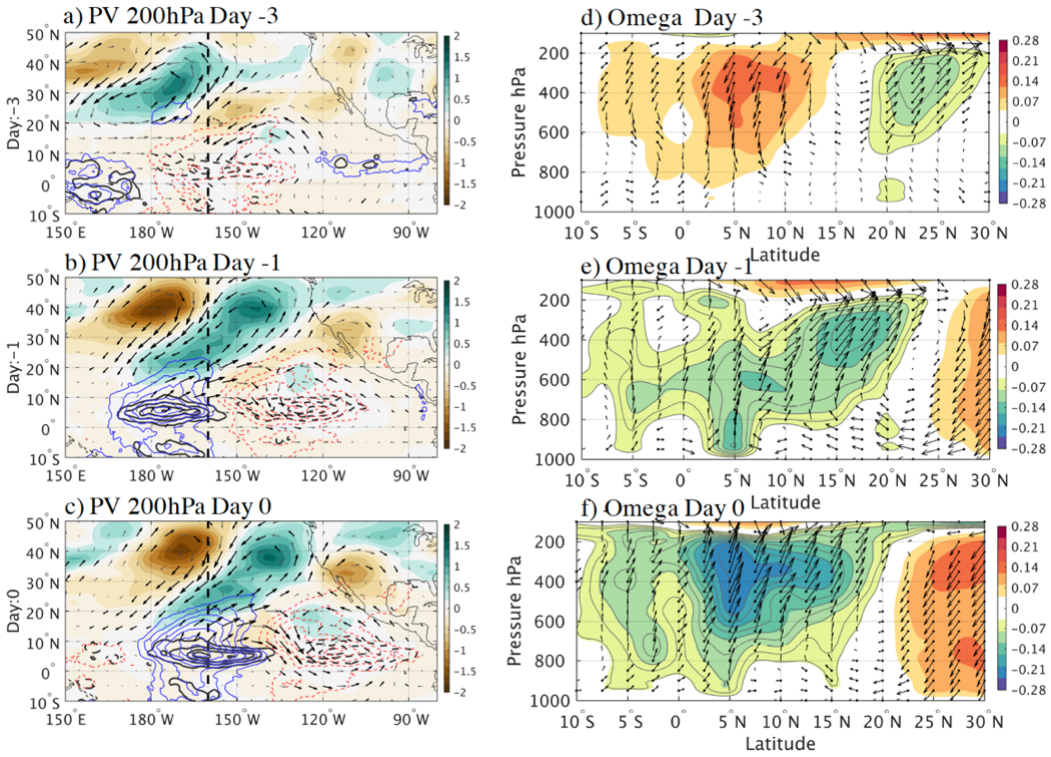


**Figure 2.11 Same as Fig. 2.10 but for MAM. Cross-sections (d-f) are at different longitude.**

Figure 2.11 shows a similar set of plots for MAM, with the vertical cross section taken at 160°W. At day -3 (Fig. 2.11a), the convectively active part of the Kelvin wave is centered at 160°E along the equator and appears removed from the influence of the extratropical Rossby wave. A northeastward tilting upper level cloud signal centered at

170°W, 25°N is being initiated/modulated by the NH Rossby wave ahead of the Kelvin wave. At 160°W, the convectively suppressed part of the Kelvin wave peaks at 5°N, where descending motion is observed in the mid to upper troposphere (Fig. 2.11d). By day -1 (Fig. 2.11b), the Kelvin wave has propagated along the ITCZ axis and has caught up with the upper cloud signal from further north. This short-lived EPD is positively tilted within the Rossby wave structure, as in DJF. Figure 2.11e shows the vertical structure of the Kelvin wave ahead of the $T_b$ minimum. Low- to mid-level upward motion is observed ahead of the Kelvin wave with a peak at 800 hPa, consistent with the fact that the convective cloud population progress from shallow to deep as a Kelvin wave propagates eastward over a particular location (Straub & Kiladis, 2002). This upward motion profile is in contrast to the DJF profile, which peaks in the mid- to upper troposphere (Figs. 2.10e and f). The omega field in Fig. 2.11e tilts upward and poleward with height, so that the short-lived EPD has peak ascending motion around 500 hPa at 17.5°N. Thus, while the Kelvin wave shows low-level convergence, the short-lived EPD vertical motion structure suggests low-level divergence. At day 0 (Fig. 2.11c), the $T_b$ minimum associated with the Kelvin wave is located at 160°W, 5°N where the maximum upward motion peaks at 400 hPa (Fig. 2.11f), consistent with the deepening of convection during a Kelvin wave passage.

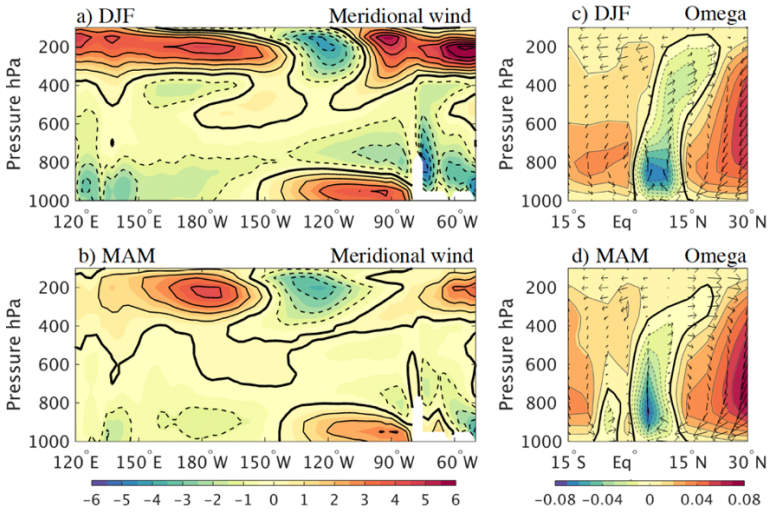


**Figure 2.12 Pressure-longitude cross section of the climatological (1984-2016) meridional wind in m $s^{-1}$ at the equator for a) DJF and b) MAM. The zero wind line is marked by the heavy black contour. Meridional circulation over the east Pacific at 120°W in vectors (vertical pressure velocity is amplified 15 times for better illustration) and vertical pressure velocity (Pa $s^{-1}$, shaded) for c) DJF and d) MAM.**

## 2.4. EPD impacts on the meridional overturning circulation

The east Pacific ITCZ has a two-mode vertical structure of convection: shallow and deep. Using reanalysis data, Back and Bretherton (2006) suggested a predominantly bottom-heavy vertical motion profile (i.e., shallow convection), with a maximum at 850 hPa controlled by a shallow meridional circulation and moist static energy import. However, satellite data suggest a top-heavy vertical motion profile, with a maximum at 400 hPa mainly from deep convective and stratiform rainfall (Hagos & Zhang, 2010; Schumacher et al., 2004). Huaman and Schumacher (2018) studied the vertical structure of latent heating in the east Pacific ITCZ, which is closely related to vertical velocity, using TRMM and CloudSat data. They showed two peaks of latent heating at 850 and 400 hPa associated with shallow and deep convection, respectively. Shallow convection

predominates in the southern part of the ITCZ where the meridional sea surface temperature (SST) gradient induces low-level convergence, and deep convection predominates in the northern part of the ITCZ over the warm SST. This section will describe changes to the overturning meridional circulation and convective clouds in the east Pacific during the passage of short-lived and Kelvin wave EPDs in DJF and MAM, respectively.

Zhang et al. (2008) identified the SMC in the east Pacific with the following criteria: i) meridional wind at 700 hPa in the opposite direction of the near-surface wind and ii) meridional wind either decreasing in magnitude or changing direction between 700 to 400 hPa. Using these criteria, the SMC is evident in the far east Pacific (140°W – 85°W) in DJF (Fig. 2.12a) and MAM (Fig. 2.12b), where the southerly component of the trade winds overturns at 800 hPa. In addition, there is a progressive transition from southerly to northerly winds in the central Pacific at 200 hPa during both seasons, which is associated with an upper level trough in the south Pacific (Vincent, 1994). The vertical structure of omega and meridional flow along 120°W is shown in Figs. 2.12c and d for DJF and MAM, respectively. During DJF (Fig. 2.12c), upward motion is strongest at low levels in the ITCZ axis and is associated with a strong shallow meridional overturning. The weaker upper level ascending motion around 15°N is related to the intrusion of NH Rossby waves with northerly flow that modulate cloudiness north of the ITCZ (Kiladis, 1998). During MAM (Fig. 2.12d), upward motion in the ITCZ deepens, suggesting convection of greater vertical extent, and the shallow meridional overturning is less distinct (although still present as shown in Fig. 2.12 b). The upper level ascending

motion around 15°N has weakened compared to DJF, but still may reflect the influence of NH Rossby waves over the central and east Pacific ITCZ. The double ITCZ is also apparent in Fig. 2.12d with the second ITCZ branch at 5°S shown by weak ascending motion below 750 hPa. Even though some studies from radiosonde and dropsonde wind profiles support the existence of the SMC (Zhang et al., 2004), Huaman and Takahashi, (2016) warned that reanalyses overestimate the total vertical velocity at low levels. Therefore, the anomalies of the meridional circulation associated with short-lived EPDs and Kelvin waves are analyzed next.

Figure 2.13 shows the vertical structure of omega and meridional circulation anomalies in the far east Pacific (120°W) during suppressed convection conditions, the transition from suppressed to deep convection, and deep convective conditions associated with short-lived EPDs during DJF and Kelvin wave EPDs during MAM. During both seasons, shallow (deep) vertical motion associated with suppressed (active) convection is seen within the ITCZ at day 0 (+2), and the transition between these conditions occurs at day +1. During MAM, short-lived EPDs are the result of extratropical Rossby waves propagating into the tropics and the meridional circulation north of the ITCZ is highly impacted, especially at mid- to upper levels (Figs. 2.13a-c). During suppressed convective conditions, northerly winds at 200 hPa associated with the NH Rossby wave ridge are associated with upper level convergence, which produces descending motion in the ITCZ and to the north (Fig. 2.13a). Weak northerly flow at 700 hPa occurs near the top of the omega anomaly in the ITCZ and indicates a small contribution to the shallow meridional overturning south of the ITCZ. During the

transition between suppressed and deep convection at day +1 (Fig. 2.13b), the extratropical Rossby wave trough and southerly winds at 200 hPa start inducing upper level divergence and low-level convergence in the ITCZ (i.e., intensification of the trade winds), but little change in flow occurs at 700 hPa. At day +2 (Fig. 2.13c), strong upper level vertical motion is observed in the ITCZ (around 7.5°N) and to the north and is associated with the upper tropospheric southerly winds and enhanced divergence. Anomalous winds are southerly at 700 hPa, acting against the shallow meridional overturning. Therefore, while short-lived EPDs seem to strengthen the meridional circulation in the northern part of the ITCZ, the SMC is much less impacted by short-lived EPDs in DJF.

During the passage of Kelvin waves in MAM, the meridional circulation in the far east Pacific is quite different than in DJF. At day 0 (Fig. 2.13d), suppressed convection is seen in the ITCZ region at 5°N and low-level divergence weakens the southerly and northerly trade winds. At 25°N, the tilted through side of the extratropical Rossby wave (see Fig. 2.6g) produces ascending motion. On day +1 (Fig. 2.13e), the Kelvin wave propagates eastward over the far east Pacific and the shallow cloud population that precedes the deep convection in the Kelvin wave appears to strengthen the shallow meridional overturning in the southern part of the ITCZ (around 5°N). The strength of the SMC is consistent when a smaller EOF domain that brackets the Kelvin wave in the far east Pacific is considered (not shown). The SMC turns into a deep circulation at day +2 (Fig. 2.13f) when deep convection is observed over the east Pacific double ITCZ. Therefore, the passage of the Kelvin wave seems to alter the southern

branch of the ITCZ, at 2.5°N, which evolves from shallow to deep convection. The southern branch of the ITCZ could be forced by both the extratropical Rossby and Kelvin waves, with both inducing upper-divergence and low-level convergence, respectively. The meridional circulation in the northern part of the ITCZ does not seem be altered during Kelvin wave passages.

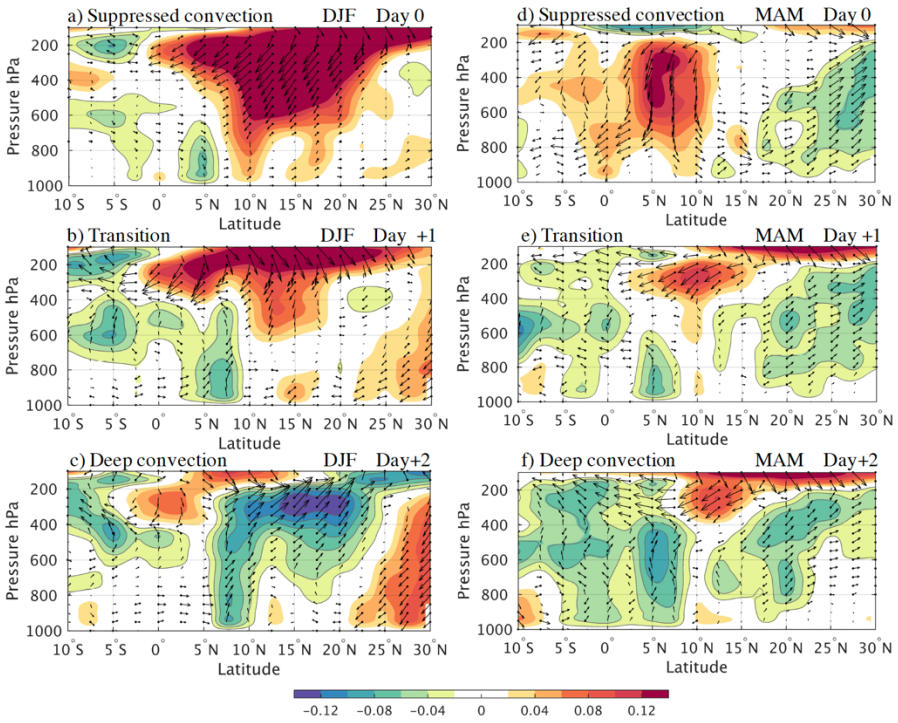


**Figure 2.13 Latitude-pressure cross sections of omega in Pa $s^{-1}$ (shading) and meridional circulation v, $\omega$ (vectors) anomalies in the far east Pacific (120°W) at different lag days for a-c) DJF and d-f) MAM.**

It has been shown that the vertical structure of vertical velocity and diabatic heating from reanalyses are inconsistent with one another and with satellite retrievals in the east Pacific due to the lack of observational constraints and limitations in the parent model convective parameterizations (e.g. Hagos & Zhang, 2010). Therefore,

measurements from the CloudSat profiling cloud radar, product 2B-GEOPROF (Marchand, R., Mace, G. G., Ackerman, T., & Stephens, 2008; Stephens, G. L., Vane, D. G., Boain, R. J., Mace, G. G., Sassen, K., Wang, Z., 2002) were used, to see if there are different observed cloud structures associated with EPDs between seasons. Two case studies were selected, a short-lived EPD from 1 January 2008 and a Kelvin wave from 27 March 2008 (see Fig. 2.2). Figure 2.14 shows the large-scale dynamical structures and vertical cross sections of CloudSat reflectivity for each event. During the short-lived EPD (Figs. 2.14a and c), the ITCZ is between 10°N and 16°N where there is a maximum in TRMM rainfall and deep convection observed by CloudSat. The short-lived EPD, which was initiated on the trough side of the extratropical Rossby wave, is located north of the ITCZ (around 17° to 25°N) along with CloudSat-observed deep upper level cloud but little rain at the surface, consistent with the DJF eastward band $T_b$ and precipitation latitudinal distribution (Figs. 2.3a and c) and anomalies of vertical velocity in MERRA2 (Figs. 2.10f and 2.13c). South of the ITCZ, most of the observed clouds have very low tops (2 km or less) and some may be classified as stratocumulus.

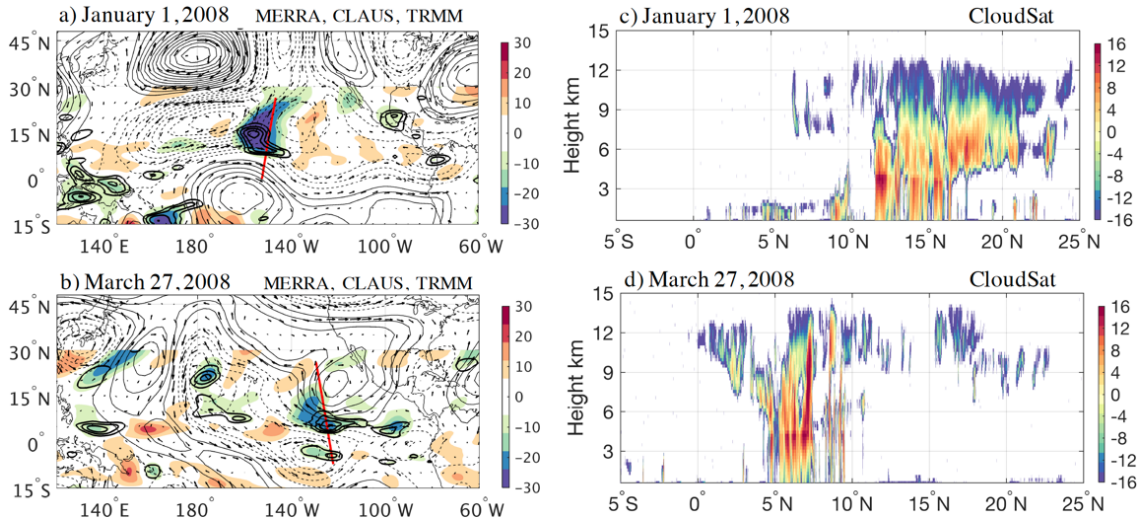


**Figure 2.14 a-b) Eastward 2.5-20-day band Tb in °C (shading), TRMM precipitation in mm $d^{-1}$ (thick contours), 200-hPa streamfunction anomalies in ms (contours) and 200-hPa wind vector anomalies in mm s during a short-lived EPD on 1 January 2008 and a Kelvin wave on 27 March 2008, respectively. Largest wind vector is around 40 m $s^{-1}$ and precipitation (streamfunction) contour interval is 0.2 mm day (4 $m^2$ $s^{-1}$). c-d) Nadir swath view of CloudSat reflectivity in dBZ for each event along the red cross section line.**

During the Kelvin wave passage (Figs. 2.14b and d), the ITCZ is between 5°N and 10°N based on the TRMM rainfall and CloudSat cross section. The convection around 5°N appears to be evolving from congestus to deep convection rapidly based on the CloudSat reflectivity structure. Very little upper level cloud is evident north of the ITCZ, which is also consistent with Figs. 2.3b and d. This Kelvin wave was forced by an extratropical Rossby wave and although the Rossby wave structure is not tilted as Fig. 2.6g, the extratropical forcing mechanism seems to be similar. The trough side of the Rossby wave propagated into the tropics and injected positive potential vorticity and upper level divergence in the tropical Kelvin wave along the ITCZ. The evolution of the SMC into a single deep overturning circulation in the southern part of the ITCZ could

produce an upper level outflow and the clouds observed by CloudSat between the equator and 5°N. The double ITCZ with deep convection is seen at 2.5°N and 5°N as suggested by the TRMM rainfall in Fig. 2.14b. The double ITCZ may be forced by both the Kelvin wave and extratropical Rossby wave. The scattered shallow clouds seen at 2.5°N in Fig. 2.14d evolved to deep convection during the following days (not shown), likely as the result of the strong low-level convergence and upper-level divergence associated with the Kelvin wave and extratropical Rossby wave, respectively.

## 2.5. Summary

This study analyzes EPDs in the tropical Pacific during boreal winter (DJF) and spring (MAM) when the wave activity in the NH extratropics is strong. Extratropical Rossby waves excited in the NH subtropical jet can propagate to low latitudes and modulate or interact with EPDs in the eastward 2.5-20-day band. The mechanisms of these EPDs were studied over the central and east Pacific using daily $T_b$ and precipitation from satellite data and dynamic fields from MERRA2 reanalysis. Empirical orthogonal functions to the eastward 2.5-20-day band $T_b$ was applied and the first principal component is regressed against TRMM precipitation and dynamic fields from MERRA2 at different lags.

The eastward 2.5-20-day band $T_b$ signal is significant during DJF and MAM, especially in the central and east Pacific. During DJF, extratropical NH Rossby waves inject positive PV into the tropics that can initiate and modulate tropical short-lived EPDs. These disturbances propagate along 15°N, many degrees north of the

climatological ITCZ, with a phase speed around 10 m $s^{-1}$ based on $T_b$ and streamfunction fields. The intrusion of high PV air into low latitudes excites upper level divergence and mid-level convergence, resulting in deep upper level cloud decks north of the ITCZ. The upper level outflow also strengthens the deep meridional circulation in the northern portion of the ITCZ. The climatological SMC observed in the southern part of the ITCZ and below 700 hPa is not significantly impacted by short-lived EPDs, perhaps because the extratropical forcing is located in the northern hemisphere and at upper levels.

During MAM, the strong eastward 2.5-20-day band $T_b$ signal corresponds to Kelvin waves that initiate in the west Pacific and propagate eastward at 15 m $s^{-1}$ along the ITCZ axis. As Kelvin waves reach the central and east Pacific, they may interact with NH extratropical Rossby waves, which propagate eastward at 10 m $s^{-1}$. The intrusion of high PV air associated with NH extratropical Rossby waves into low latitudes excites upper level divergence in the Kelvin wave, which strengthens the Kelvin wave convection. The NH Rossby waves in MAM also modulate short-lived EPDs north of the Kelvin waves, around 15°N, similar to DJF. Therefore, tropical convection in the eastward 2.5-20-day band during MAM is the result of Kelvin waves in the ITCZ region (7°N climatologically) and short-lived EPDs north of the ITCZ (15°N climatologically). Shallow convection ahead of the Kelvin wave appears to enhance the SMC in the southern part of the ITCZ.

Our results distinguish between two types of eastward disturbances in the tropical Pacific during DJF and MAM, with different physical mechanisms and impacts in the central and east Pacific ITCZ. Future work involves analyzing the interannual variability

of short-lived EPDs and Kelvin waves, especially during El Niño events when the central and east Pacific is dominated by deep convection.

# CHAPTER III

# EASTERLY WAVES IN THE EAST PACIFIC DURING THE OTREC 2019 FIELD CAMPAIGN[*]

## 3.1. Background

Easterly waves (EWs) are prominent synoptic (i.e., 2 to 10-day period) features in the Pacific ITCZ with westward phase speeds between 11 - 14 m $s^{-1}$ (Serra et al., 2008). EWs commonly serve as precursors to tropical cyclones and hurricanes in the East Pacific (Pasch et al., 2009; Serra et al., 2010) and are associated with 25 to 40% of the deep convective clouds and produce up to 50% of the seasonal precipitation over the far East Pacific during boreal summer (Dominguez et al., 2020). Thus, EWs impact both the weather and climate of the East Pacific ITCZ.

EWs are found in the eastern Atlantic and West Africa (Berry et al., 2007; Gomes et al., 2019; Janiga & Thorncroft, 2013; Kiladis et al., 2006; Reed et al., 1977), East Pacific (Raymond & Torres, 1998; Rydbeck et al., 2017; Serra et al., 2008; Tai & Ogura, 1987; Zehnder et al., 1999), the western and central Pacific (Reed & Johnson, 1974; Reed & Recker, 1971), and the Caribbean Sea (Riehl, 1954). In the East Pacific, EWs are consistent with Riehl's classical “inverted trough" model (Riehl, 1954). In this model, positive specific humidity anomalies are concentrated in the lower troposphere in advance of the trough axis and deepen within and behind the trough where enhanced

[*] A version of this chapter was published as “Easterly waves in the East Pacific during the OTREC 2019 field campaign” in *Journal of Atmospheric Sciences* by Huaman, Lidia, E. Maloney, C. Schumacher, and G. Kiladis, 2021. 

convection and column-integrated moisture anomalies are favored. The maximum vertical component of vorticity is located between 700 and 600 hPa and EW wavelengths range between 4200 and 5900 km. Ahead of the wave (i.e., west of the trough axis), the planetary boundary layer (PBL) is warm and moist, and northerly winds are predominant. Behind the wave (i.e., east of the trough axis), the PBL is cold and dry and dominated by southerly winds. Serra et al. (2010) showed that while some East Pacific EWs originate from Atlantic disturbances east of 70°W, others are generated locally in the Caribbean and East Pacific. Additionally, it is important to mention that the EWs predominate over warm SST regions and notable mean meridional humidity gradients. Rydbeck and Maloney (2015) showed that anomalous meridional winds acting on the mean meridional moisture gradient of the ITCZ produce moisture anomalies that enhance convection in the though side of the EW. The orientation of EWs is generally southwest-northeast, which helps an EW maintain kinetic energy through barotropic conversion in the presence of a meridionally sheared zonal flow (Rennick, 1976; Rydbeck & Maloney, 2014; C. Thorncroft & Hoskins, 1993).

EWs are important features of the East Pacific ITCZ. The net effect of many synoptic-scale disturbances, such as EWs and convectively coupled equatorial waves (CCEWs; Huaman et al., 2020; Kiladis et al., 2009; Serra et al., 2014), plus local mechanisms like low-level convergence produced by strong meridional sea surface temperature (SST) gradients (Back & Bretherton, 2009; Lindzen & Nigan, 1987), define the climatological structure of the ITCZ. The mean vertical structure of the East Pacific ITCZ has been studied in some detail. Back and Bretherton (2006) showed maximum

vertical motion at 850 hPa based on reanalysis fields that was associated with an import of moist static energy (MSE) through vertical advection. However, a second vertical motion peak aloft was observed using two months of data from the East Pacific Investigation of Climate Processes in the Coupled Ocean – Atmosphere System (EPIC-2001) field campaign and satellite data (Huaman & Takahashi, 2016; Zhang et al., 2004, 2008). Additionally, Huaman & Schumacher (2018) used 16 years of CloudSat and Tropical Rainfall Measuring Mission (TRMM) satellite data to demonstrate that two peaks of latent heating associated with deep and shallow convection are apparent in this region and linked to deep and shallow meridional circulations. They also found that the vertical structure of the ITCZ is tilted meridionally; shallow convection occurs around 6°N in the southern part of the ITCZ, and transitions to deep convection around 9°N in the northern part of the ITCZ.

Most of the studies in the East Pacific have relied on reanalyses to describe the three-dimensional structure of EWs. The lack of direct observations in the East Pacific causes reanalysis datasets to rely heavily on model physical parameterizations, supporting the need for targeted field campaigns. Serra and Houze (2002) used the Tropical Eastern Pacific Process Study (TEPPS-1997) research cruise dataset to study synoptic-scale convection and found that EWs are prominent convective features during boreal summer. Petersen et al. (2003) used the EPIC-2001 field campaign dataset to study EWs, revealing their thermodynamic characteristics and four-dimensional precipitation structure using shipborne C-band, Doppler radar data. OTREC is the latest field campaign over the East Pacific and took place from 4 August to 2 October 2019

(Fuchs-Stone et al., 2020). OTREC goals were to determine the large-scale environmental factors that control convection over the tropical oceans and to characterize the interaction of convection with tropical disturbances, especially EWs. OTREC used the NSF/NCAR Gulfstream V aircraft to survey the East Pacific and deploy gridded patterns of dropsondes from a high altitude (i.e., 13 km) to characterize the large-scale environmental state and integrated effects of convection. The aircraft also provided profiles of radar reflectivity with a W-band radar.

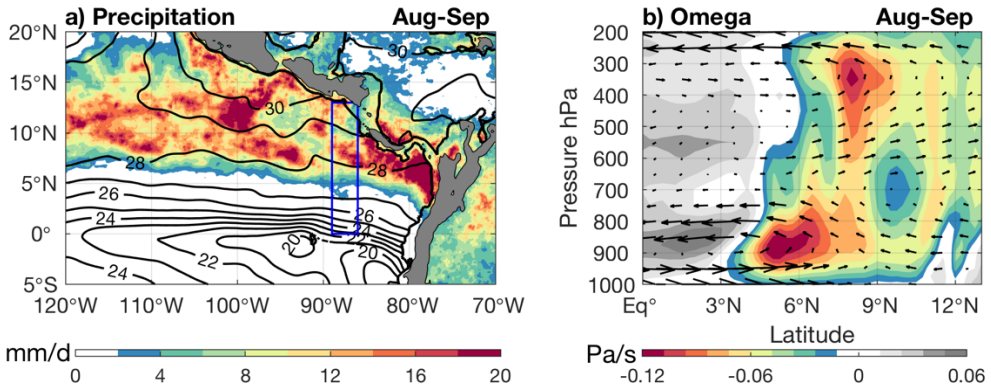


**Figure 3.1 a) Total precipitation in mm $d^{-1}$ from IMERG and SST in C° from OSTIA, and b) cross section of omega in Pa $s^{-1}$ and meridional flow across the OTREC region (blue rectangle in a) from ERA5 for August and September 2019.**

Figure 3.1 shows the mean precipitation from the Integrated Multi-satellitE Retrievals for Global Precipitation Measurement (IMERG) dataset and mean SST from the Operational Sea Surface Temperature and Sea Ice Analysis (OSTIA) (left panel) and a cross section of vertical motion and flow in the meridional plane over the far East Pacific from ECMWF Reanalysis 5th Generation (ERA5) reanalysis (right panel) for August-September 2019, a period approximately corresponding to the OTREC field

campaign period. Section 2 describes the precipitation and reanalysis data sets in more detail. The OTREC field campaign was held in the far East Pacific in a box delineated approximately by 89°-86°W and 0°-13°N (indicated by the blue rectangle in Fig. 3.1a); this will hereafter be called the OTREC region box. Over the OTREC region box the maximum precipitation (Fig. 3.1a) was located around 9°N over a weak SST gradient (i.e., the East Pacific warm pool) and precipitation extended towards this region from the Colombian coast (Toma & Webster, 2010a,b). A strong meridional SST gradient was seen south of the precipitation maximum, with coldest SSTs south of the equator (i.e., the East Pacific cold tongue). The vertical motion cross section (Fig. 3.1b) shows shallow and deep vertical motion peaks associated with differing convective profiles that are linked to shallow and deep circulations, respectively. Jaramillo et al., (2017) showed that the deep convection located around 8°N over warmer SSTs is associated with mesoscale convective systems (MCSs), while the shallow vertical motion peak at 6°N has been shown to be driven by the strong SST meridional gradient and associated low-level convergence (Lindzen & Nigan, 1987) that forms shallow cloud structures with light precipitation (Huaman & Schumacher, 2018). The shallow structures likely do not evolve into deep structures because of the cooler SST and dry upper-level air in that region (Zuidema et al., 2006).

Most previous studies about the vertical structure of the East Pacific ITCZ and associated circulations have been focused on seasonal scales, but synoptic variations of the deep and shallow circulations have not yet been examined in detail. Further, previous analyses were limited to reanalysis data and satellite retrievals (e.g., Back & Bretherton,

2006; Handlos & Back, 2014; Huaman & Schumacher, 2018; Huaman & Takahashi, 2016) because of the lack of observations in the East Pacific. In this study, the goals are to 1) characterize the synoptic variability in the East Pacific during the OTREC 2019 field campaign, providing useful large-scale context for more specialized studies in this region, and 2) understand how this synoptic variability influences convection and deep and shallow circulations in the East Pacific ITCZ during OTREC by modulating the moisture and MSE fields. The modulation of shallow and deep meridional circulations associated with the passage of EWs will be assessed using ERA5 reanalysis fields, satellite precipitation, and OTREC field campaign data. Thompson et al., (1979) stated that shallow clouds were found to be abundant near the EW ridge, whereas detrainment from both deep and mid-level cumulus clouds dominated in the wave trough. It is hypothesized that EWs alter the moisture and MSE fields that modify the strength of convection and the overturning circulation in the ITCZ region.

## 3.2. Data and methods

### *3.2.1. Data description*

Hourly data from the ERA5 reanalysis (Hersbach et al., 2020) is used with a horizontal grid spacing of 0.25° and 37 pressure levels. The hourly ERA5 data were averaged to daily data. The variables from ERA5 used in this study include horizontal and vertical winds, specific humidity, temperature, and precipitation during the OTREC period (August 5 - October 3 of 2019).

Daily precipitation retrievals from the Global Precipitation Measurement (GPM) mission (Hou et al., 2014) were also used. IMERG is a unified satellite precipitation dataset produced by NASA to estimate surface precipitation over most of the globe (Huffman et al., 2015). Precipitation estimates from the GPM core satellite are used to calibrate precipitation estimates from microwave and infrared sensors on other satellites. After merging the estimates from multiple satellites, surface precipitation maps are produced at 0.1° horizontal resolution in the IMERG product.

OTREC dropsondes from the NSF/NCAR Gulfstream V aircraft were also used. Flight operations for OTREC took place from 5 August to 3 October 2019. While other regions were also sampled, twelve research flights (RFs) were performed over an East Pacific OTREC flight box (89° - 86°W, 3° - 11°N), a slightly smaller area than the OTREC region delineated in Fig. 3.1a. Each flight lasted six hours, starting in the southern part of the box at 12 UTC and reaching the northern part at 18 UTC. The flight pattern is shown in Figure 1 of Fuchs-Stone et al. (2020). Around 32 dropsondes were deployed during each flight from an altitude near 13 km. The dropsondes collected measurements of horizontal winds, temperature, and humidity between the aircraft and the surface with vertical resolution of around 0.5 hPa. The data was downsampled to a resolution of 20 hPa. As part of the OTREC field campaign, radiosondes in Santa Cruz, Costa Rica (10.26°N, 85.58°W) were also launched between 20 August and 30 September 2019, at 00 and 12 UTC (6 pm and 6 am local time, respectively). OTREC dropsonde and sounding data were sent to the Global Telecommunication System (GTS) and ERA5 reanalysis assimilated these data.

In addition to dropsondes, observations from the Hiaper cloud radar (HCR) installed on the NSF/NCAR Gulfstream V aircraft (Rauber et al., 2017) were used. HCR is a polarimetric, millimeter-wavelength (W-band) radar that can detect light rain and ice and liquid clouds. It collects reflectivity and Doppler radial velocity measurements, which at a vertical incident angle include the vertical wind speed and particle fall speed. The aircraft flies at an average ground speed of 190 m $s^{-1}$, with a radar sampling rate of 0.1 s. All OTREC datasets were processed by the National Center of Atmospheric Research (NCAR; Vomel et al., 2021).

Additionally, Geostationary Operational Environmental Satellite (GOES)-16 images were used to complement the OTREC dataset. GOES-16 is a current geostationary satellite operated by NOAA and NASA and provides 16 spectral bands including 10 infrared (IR) channels. This study used the GOES-16 longwave IR channel 14 with a 6 km x 6 km resolution processed by NCAR/EOL and available at http://catalog.eol.ucar.edu/maps/otrec.

*3.2.2. Identification of EWs*

The ERA5 and IMERG anomaly values used in the identification of the EWs were calculated by removing the first three harmonics of the seasonal cycle based on the climatology between 1998 and 2018. Additionally, the OTREC period average was removed in order to eliminate any decadal or interannual signal that may have occurred during this period. EWs during the OTREC campaign were identified as follows. First, precipitation anomalies and dynamical fields were filtered using a fast Fourier technique retaining wavenumbers between -20 to 0 and periods between 2.5 and 10 days

corresponding to EWs. This filtered domain band is also referred to as tropical depression (TD) type disturbance region (Frank & Roundy, 2006). Although this region of wavenumber-frequency space includes both TD-type disturbances and mixed Rossby-gravity (MRG) waves (Yokoyama & Takayabu, 2012), the horizontal structure of winds and vorticity for each EW event are consistent with previous EW studies. Additionally, an extended time period was used for this calculation (from June to November 2019) to minimize edge effects and ensure no data loss due to filtering for the OTREC period.

The total precipitation and TD-band precipitation anomaly averaged were averaged over the OTREC flight box (89° - 86°W, 3° - 11°N) and identified potential convectively-active EW events when the total precipitation and TD-band precipitation anomaly were larger than the mean + 1.25 standard deviation. The potential EWs identified on the basis of precipitation were checked to ensure they were also accompanied by strong filtered vorticity and meridional wind signals at 600 and 700 hPa that resemble EWs and not other westward propagating disturbances such as MRG waves that have a similar phase speed but a different dynamical horizontal structure. In particular, the convectively-active EWs selected had horizontal structures similar to those studied by Serra et al. (2008) and Rydbeck and Maloney (2015). Additionally, the wave life cycle lasted more than two days as in Hodges (1995, 1999).

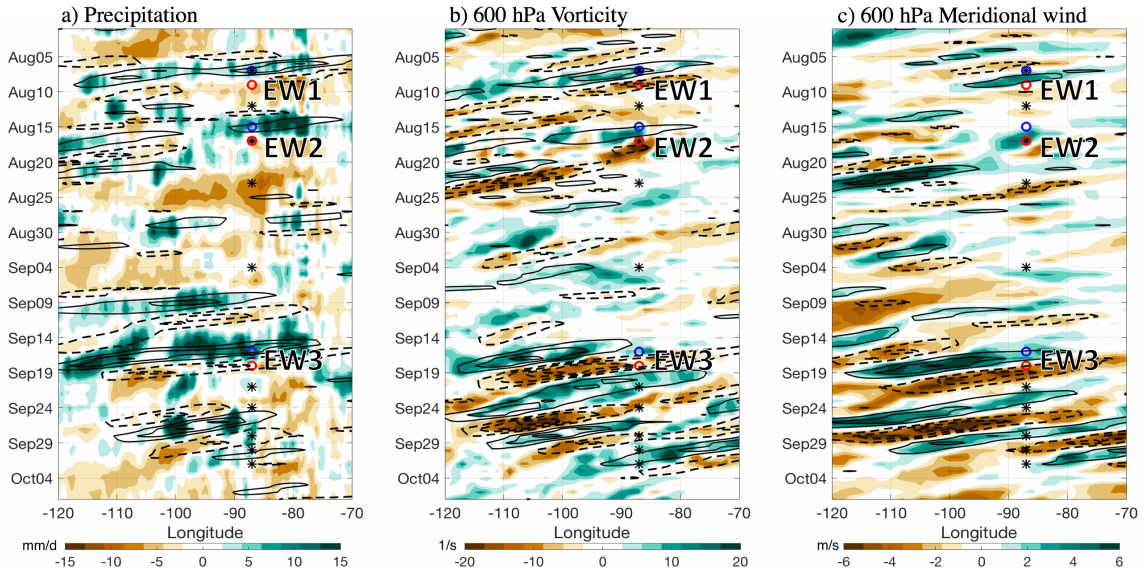


**Figure 3.2 Hovmöller diagrams averaged from 3 - 11°N of a) precipitation in mm $d^{-1}$ from IMERG, and b) 600-hpa vorticity in $s^{-1}$ and c) 600-hPa meridional winds in m $s^{-1}$ from ERA5. Total values are shaded and TD-band values are in contours (precipitation contours every 4 mm $d^{-1}$, vorticity contours every 4 $s^{-1}$, and 600-hPa meridional wind contours every 2 m $s^{-1}$). Symbols are placed in the OTREC region, the stars indicate OTREC RF dates and the circles highlight enhanced convection (blue) and suppressed convection (red) associated with EWs.**

Figure 3.2 shows Hovmöller diagrams of total and EW filtered anomalies for precipitation, 600-hPa vorticity, and 600-hPa meridional wind in the OTREC flight box. The 700-hPa Hovmöller diagrams look generally similar to the 600-hPa Hovmöller, and are not shown. Based on the criteria discussed above, three convectively-active EWs were identified in the Hovmöller precipitation diagram accompanied by strong vorticity and meridional wind signals that propagated from southwest to northwest. EWs 1 and 3 produced enhanced precipitation in the OTREC region on 7 August and 17 September, respectively, associated with positive vorticity anomalies at 600 hPa. Southerly wind anomalies at 600 hPa were seen the next day. EW 2 produced enhanced precipitation in

the OTREC region on 15 August, and the strongest vorticity and southerly wind anomalies were seen at 700 hPa (not shown). EWs 1 and 2 showed strong signals of precipitation over the Caribbean (80°W) at day -1 and seemed to pass from the Caribbean to the East Pacific (90°W), although EW 3 appeared to be generated in the East Pacific (not shown). Although vorticity and meridional winds displayed westward propagation during the last two weeks of September, these propagating features did not have a strong reflection in precipitation, and hence are not analyzed further here.

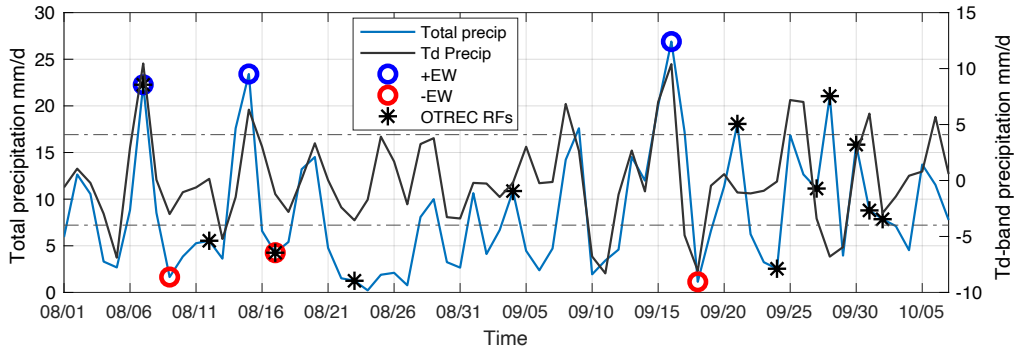


**Figure 3.3 Time series of total (left axis) and TD-band (right axis) IMERG precipitation over the East Pacific OTREC flight box (89° - 86°W, 3° - 11°N). Dashed lines indicate the threshold of TD-band precipitation over the OTREC period average ± 1.25 standard deviation. As in Fig. 3.2, the stars indicate OTREC RFs and the circles highlight when EWs were present.**

The total precipitation and TD-band precipitation anomaly time series over the OTREC flight box are shown in Fig. 3.3. The convectively-active EWs identified had a strong positive precipitation peak (> 17 mm $d^{-1}$), accompanied by cyclonic vorticity anomalies as seen in Fig. 3.2, followed by suppressed precipitation two days later. There were two additional events that exceeded our 1.25 deviation standard threshold but, based on Fig. 3.2, were not analyzed further due to the lack of vorticity and meridional

wind signals (9 September) or unclear precipitation propagation (25 September). Two OTREC RFs coincided with the passage of the EWs identified in this study. The first OTREC RF, on 7 August, corresponded to a day with enhanced precipitation associated with the trough of the EW. The other OTREC RF, on 17 August, corresponded to a day with suppressed precipitation associated with the ridge of the EW. Although OTREC RFs only partially captured two EWs, ERA5 data was employed to study the three EWs previously identified with the IMERG data. ERA5 assimilated all available dropsondes and intensive radiosonde operations occurred in Costa Rica and Colombia during OTREC that provided further constraints on the reanalysis fields for all EWs examined.

## 3.3. Horizontal and vertical structure of the OTREC EWs

### *3.3.1. Composite EW structure*

Figures 3.4 and 3.5 show the composite precipitation during the passage of the three EWs. Precipitation at day 0 (Figs. 3.4a, 3.5c) corresponds to the precipitation averaged on 7 August, 15 August and 17 September, when precipitation peaks in the OTREC region, and day +2 (Figs. 3.4b, 3.5h) represents the suppressed precipitation phase two days later. On day 0, enhanced precipitation associated with the convective part of the EW was seen over the far East Pacific ITCZ centered over the OTREC box. At day +2, the enhanced precipitation associated with the EW propagated northwestward along the coast to 105°W, 17°N, while precipitation became suppressed in the OTREC box. The intense precipitation at 100°W, 10°N is caused by the EW and the northwestward propagation is confirmed in Fig. 3.5. The mean zonal phase speed of the

three EWs was estimated from the longitude-time diagram of composite precipitation for the latitude range 3°-11°N, which corresponds to the OTREC flight box latitudes (Fig. 3.4c). Composite precipitation associated with the EWs propagated westward at about 11.5 m $s^{-1}$ between 80° and 115°W, although it was slower near 100°W. The zonal propagation of precipitation was seen both in the total precipitation (Fig. 3.4c) and precipitation anomalies (Fig. 3.4d), although it should be noted that there was also substantial meridional propagation (not shown).

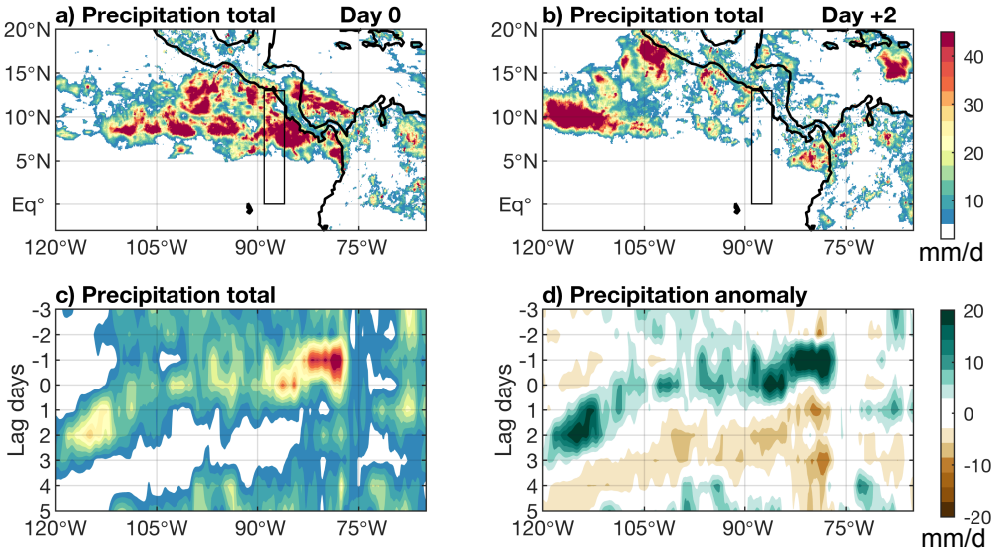


**Figure 3.4 IMERG precipitation in mm $d^{-1}$ averaged over the three OTREC EWs during a) enhanced (day 0) and b) suppressed (day +2) conditions. Longitude-time diagrams of c) total precipitation and d) anomaly precipitation for the latitude range 3°-11°N during the three EW events. The black box indicates the OTREC region box.**

Figure 3.5 shows the composite horizontal structure of EW precipitation anomalies and 600-hPa horizontal wind anomalies and the north-south cross sections of vertical velocity and meridional motion in the OTREC box from day -2 to day +3.

Vertical velocity was used as a proxy for convective strength. Weak vertical motion (i.e., vertical velocities between -0.05 and 0.05 Pa/s) were seen at 90°W, 9°N especially at low levels (below 600 hPa) due to the cold SSTs in this region (i.e., the Costa Rica dome, Xie et al. 2005) that inhibit deep convection. At day -2 (Figs. 3.5a, d), positive precipitation anomalies of about 10 mm $d^{-1}$ were located in the ITCZ axis, with generally easterly 600-hPa wind anomalies. Over the OTREC box, the vertical motion cross section suggests shallow and deep convection similar to the August-September average cross section in Fig. 3.1b. Shallow convection associated with a shallow meridional circulation was located at 850 hPa and 6°N, while deep convective vertical motion associated with a deep meridional circulation was located at 300 hPa and 8°N.

At day -1 (Figs. 3.5b, e), enhanced precipitation (with anomalies larger than 30 mm $d^{-1}$) associated with the EW trough (i.e., the center of maximum vorticity) was greatest at 80°W, slightly east of the OTREC box. Over the OTREC box, ahead of the EW trough, the northerly flow at 850 hPa associated with the shallow circulation weakened from 4 m $s^{-1}$ at day -2 to 2 m $s^{-1}$ at day -1 and the region of shallow vertical motion moved northward toward the region of deep convection. The trough of the EW was associated with a transition of the shallow convection structure over the OTREC box to a deep convective structure. Additionally, the anomalous wind field at 600 hPa indicated a strengthening of the Caribbean low-level jet (CLLJ) during the passage of EWs with easterly zonal wind anomalies around 5 m $s^{-1}$ located near 15°N, 75°W that maximized at 925 hPa (not shown) and extended upward to 600 hPa (Martin & Schumacher, 2011; Poveda et al., 2014; Rapp et al., 2014; Whitaker & Maloney, 2018).

The cyclonic circulation of EWs has been associated with strengthening of the CLLJ easterly flow at 850 hPa (Molinari & Vollaro, 2000), which can then penetrate from the Caribbean into the Pacific through a gap in the mountains as the Papagayo jet (Molinari et al., 1997; Shapiro, 1986). The variations of the CLLJ during OTREC are consistent with Whitaker and Maloney (2020) who showed the strengthening of the CLLJ and Papagayo jet during the passage of an individual EW in the East Pacific. However, further examination of the interactions between the CLLJ and EWs is outside the scope of this study.

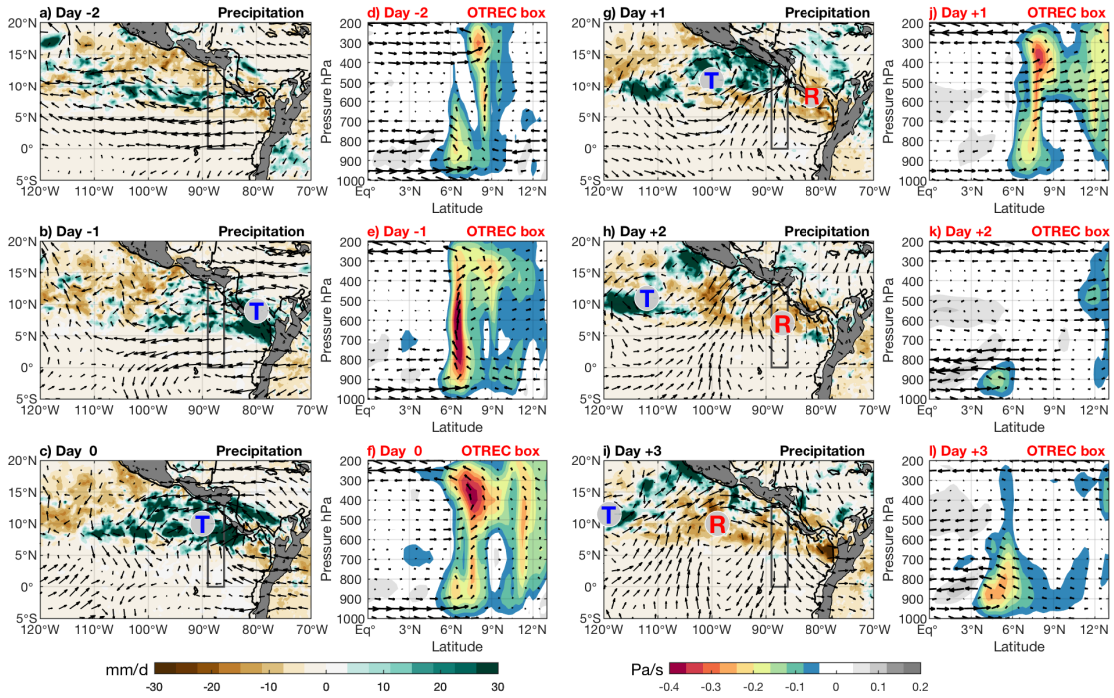


**Figure 3.5 (a-c, g-i) Precipitation anomalies in mm $d^{-1}$ superimposed with 600-hPa horizontal wind anomalies across the East Pacific and (d-f, i-l) omega cross sections in Pa $s^{-1}$ superposed by meridional flow over the OTREC region (gray rectangle) from day -2 to day +3 composited for the three EWs. The trough and ridge centers of the EW are labeled as T and R, respectively. Largest wind vector is 5 m $s^{-1}$.**

At day 0 (Figs. 3.5c, f), the enhanced precipitation associated with the EW trough was located at 90°W, next to the OTREC box. The horizontal winds at 600 hPa were characterized by anomalous cyclonic rotation and positive midlevel vorticity that supported deep convection and enhanced precipitation. Raymond et al. (2014) used observational data over the tropics to show that mid-level vortices modify the virtual temperature profile (i.e., cooler below the mid-level vortex and warmer above) to create low-level instability that fosters strong low-level convergence and subsequent deep convection. Over the OTREC box, the deep circulation was dominant compared to the shallow circulation. The vertical velocity peak was centered at 400 hPa and 8°N, indicating a stratiform profile (Schumacher et al., 2004). A weak shallow vertical velocity peak also existed at day 0, consistent with the presence of updrafts in convective elements that accompany the stratiform features, as noted in previous studies (e.g. Masunaga & Luo, 2016).

At day +1 (Figs. 3.5g, j), enhanced precipitation associated with the trough of the EW moved to 100°W, a few degrees west of the OTREC box, and the circulation field was oriented southwest - northeast. Over the OTREC box and behind the EW trough center, the vertical motion associated with deep convection was still strong but weaker compared to the previous day, and the shallow circulation was still muted. The deep convection was likely maintained by the enhanced mid-level southerly inflow associated with the cyclonic circulation of the EW that brings horizontal convergence (Huaman and Takahashi 2016; Nolan et al. 2007, 2010}. At day +2 (Figs. 3.5h, k), the enhanced precipitation associated with the EW trough was centered at 110°W, 15°N, and

suppressed precipitation and associated negative vorticity anomalies in the EW ridge (i.e., the center of minimum vorticity) were predominant over the OTREC box. The EW circulation was oriented west-east at day 0, but developed a southwest-northeast tilt on subsequent days. This tilted structure has been argued by previous studies to be associated with vortex stretching and horizontal elongation from southwest to northeast of the dynamical signature of the wave (Rydbeck & Maloney, 2015). The cross section over the OTREC box shows suppressed deep convection and a pronounced shallow circulation with a strong overturning circulation at 850 hPa (i.e., meridional winds larger than 7 m $s^{-1}$) south of 6°N. This shallow circulation became deeper and strengthened at day +3 (Figs. 3.5i, l). The composite analysis suggests strong modification of the shallow and deep circulations during the passage of EWs, including intensification of the deep circulation at day +0 and shallow circulation at days +2 and +3. All three EWs examined during OTREC have qualitatively similar modulation of the deep and shallow circulations (not shown). The mechanisms through which the deep and shallow circulations are modulated by the passage of the EWs will be discussed in section 5.

The vertical structure of EWs at the two latitude ranges where the deep and shallow circulations predominated will now be described. Figure 3.6 shows time-height diagrams of anomalous ERA5 vorticity, specific humidity, meridional wind, and vertical velocity composited for the three EWs over the northern part of the OTREC box (7 - 11°N) where the deep circulation in the ITCZ was dominant (Figs. 3.6a-d) and the southern part of the OTREC box (3 - 7°N) where the shallow circulation was dominant

(Figs. 3.6e-h). The composite evolution of the EW vertical structure during the OTREC campaign in the northern part of the ITCZ is consistent with Serra et al. 2008.

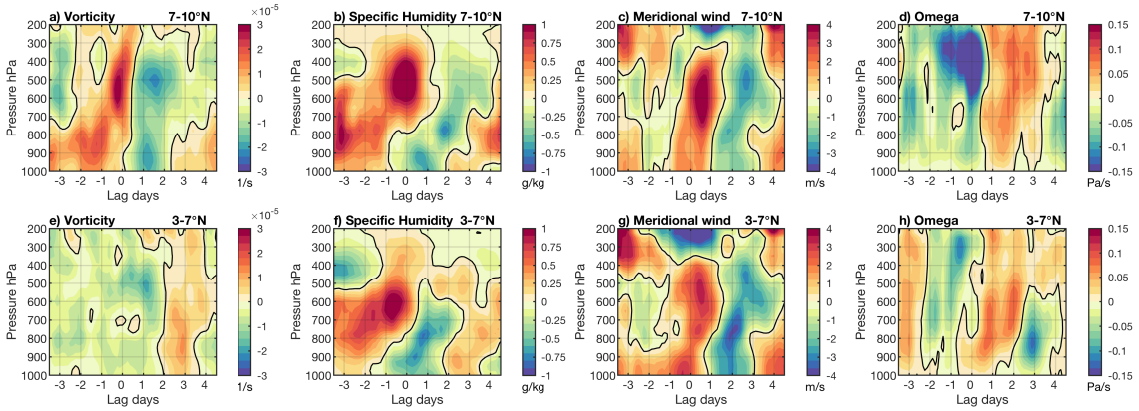


**Figure 3.6 Time-height diagrams of vorticity ($s^{-1}$), specific humidity (g $kg^{-1}$), meridional wind (m $s^{-1}$), and omega (Pa $s^{-1}$) anomalies at a-d) 7-11°N and e-h) 3-7°N averaged at 89-86°W over the three OTREC EWs.**

At days - 2 and -1, ahead of the EW trough, positive vorticity (Fig. 3.6a), positive humidity anomalies (Fig. 3.6b), and northerly winds (Fig. 3.6c) occurred below 600 hPa between 7 - 10°N, with upward vertical motion anomalies throughout the troposphere (Fig. 3.6d). However, the southern part of the OTREC box (3 - 7°N) was not as strongly impacted by the EWs, and the vorticity (Fig. 3.6e) and upward motion (Fig. 3.6h) anomalies were weak. Northerly winds associated with the cyclonic circulation of the EW were not seen but instead southerly winds below 850 hPa (Fig. 3.6g) dominated over this region. At day 0, within the convective part of the EW, positive vorticity and strong upward vertical velocity anomalies occurred throughout the troposphere between 7 - 10°N, with positive specific humidity anomalies above 800 hPa and negative specific humidity anomalies below 800 hPa. The meridional wind anomalies suggest a

strengthening of the deep meridional circulation, with intensification of the upper-level (200 hPa) meridional outflow and low to mid-level meridional inflow, especially around 600 hPa where anomalies were up to 5 m $s^{-1}$. This structure is consistent with convective and stratiform structures in MCSs with deep circulations (Whitaker & Maloney, 2020) and in other equatorial disturbances (Kiladis et al., 2009). However, in the southern part of the OTREC box, the vorticity and upward vertical motion anomalies were weak throughout the troposphere at day 0, which suggests only weak impact of EWs on shallow convection and associated circulations at these latitudes. At day +2, behind the trough of the EW, negative vorticity anomalies and downward anomalous vertical motion were seen throughout the troposphere with anomalous northerly winds at mid-levels between 7 - 10°N. In the southern part, positive vorticity anomalies and positive specific humidity anomalies occurred, with strong meridional outflow around 800 hPa characterized by anomalies up to 4 m $s^{-1}$ and shallow upward vertical motion that intensified until day +3, suggesting significant impacts on shallow convection and associated circulations at these latitudes. The vertical structure of the EWs between 7 - 10°N from ERA5 was consistent with the vertical structure of EW 3 derived using OTREC radiosondes from Santa Cruz, Costa Rica (not shown).

### *3.3.2. Individual EWs*

The individual EW events are now analyzed using the OTREC field campaign observations, supplemented by ERA5 and GOES IR imagery. Two RFs occurred during the passage of EWs (Figs. 3.2 and 3.3). During OTREC RF 1 (7 August), the

NSF/NCAR Gulfstream V aircraft flew in the region of enhanced precipitation associated with the trough of EW 1. During OTREC RF 5 (17 August), the aircraft flew in the suppressed precipitation associated with the ridge of EW 2.

Figure 3.7 shows the air temperature (red) and dewpoint temperature (blue) profiles at days 0 and +2 at 8°N and 4°N during all three EWs from ERA5 and OTREC. OTREC dropsondes from two RFs and profiles from ERA5 for the other times are used. ERA5 profiles are similar to the OTREC profiles during the August 7 and August 17 events shown here (not shown). Table 1 shows the lifting condensation level (LCL), convective available potential energy (CAPE), and convective inhibition (CIN) values for each day and latitude.

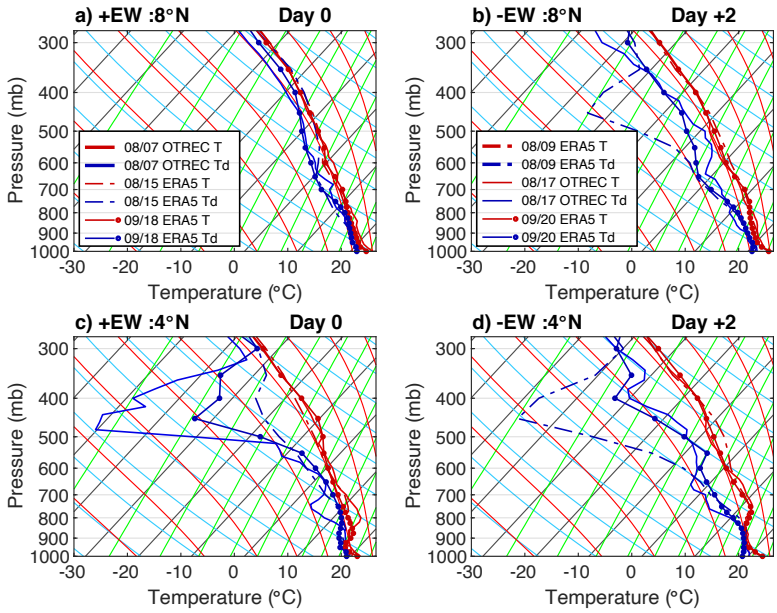


**Figure 3.7 Skew-T diagrams for all the 3 EWs (08/07, 08/15 and 09/18) during the OTREC field campaign from ERA5 and OTREC RFs at day 0 (left) and day 2 (right) for (a,b) 8°N and (c,d) 4°N. RF times are between 12-18 UTC.**

At day 0 and 8°N (Fig. 3.7a), the soundings showed moist conditions throughout the troposphere associated with the convectively active part of the EWs (Figs. 3.5c, f). Table 1 indicates that the LCL was around 970 hPa in each EW, CAPE was 1934 J $kg^{-1}$ for EW 1 and around 1185 J $kg^{-1}$ for the other two EWs, while CIN was 0 J $kg^{-1}$ for all EWs. At day +2 (Fig. 3.7b), when the composite EW trough had moved west and there was no longer a deep meridional circulation (Figs. 3.5h, k), a shallow moist layer was seen between 1000 and 900 hPa, with drier conditions above, especially during EW 1. The LCL varied between 956 hPa and 975 hPa, making the LCL slightly higher in two of the three EWs (i.e., EW 1 and EW 3) at day +2 compared to day 0. CAPE increased in EW 2 and EW 3 at day 2, reaching 2260 J $kg^{-1}$ in EW 2. This large value indicates that this index is inadequate by itself for detecting the potential for deep convection, as found in other studies (e.g., Sherwood et al. 2004), since suppressed convection is associated with the ridge of the EW (Fig, 3.5h). CIN remained zero in all three EWs at day +2.

At day 0 and 4°N (Fig. 3.7c), which represented conditions south of the main precipitation area of the convectively-active EW, there was a layer of moist air below 800 hPa, consistent with shallow convection driven by the strong meridional SST gradients (Back & Bretherton, 2009). Dry air predominated aloft, especially between 500 and 300 hPa. The temperature profiles also suggested a weak trade wind inversion between 950 and 850 hPa. Table 1 shows that the LCLs were similar to 8°N values but that CAPE was substantially less, with values ranging from 62 to 395 J $kg^{-1}$. CIN was strongly negative with values ranging from -36 to -68 J $kg^{-1}$. The decrease in CAPE and change to negative CIN can be explained by the large north-to-south variation in SST

and vertical motion in the East Pacific ITCZ that substantially alters the boundary layer properties and impacts CAPE and CIN (e.g., Ye et al. 1998), such as the existence of the trade wind inversion at 4°N. At day +2 (Fig. 3.7d), the low-level moist layer extended up to 800 hPa and was capped by a stronger, deeper (between 850 and 750 hPa) inversion than on day 0. Conditions remained dry aloft. LCL heights became higher in EW 1 and EW 3 and CAPE increased in EW 2 and EW 3 (similar to the day 0 to day +2 trends at 8°N). CIN was less strongly negative compared to day 0 except in EW 3.

Figure 3.7 and Table 3.1 indicate that the thermodynamic structure variations of the three EWs between days 0 and +2 were qualitatively similar, although the magnitude of the variations showed substantial differences across events. Of note is a larger spread in the dew point profiles at the mid and upper levels than in the temperature profiles, and this difference became more pronounced at 4°N. While it could be argued that some of this variability was introduced by only assimilating OTREC dropsondes in a subset of the profiles, the very strong dry air layer during EW 1 exists in the ERA5 profiles two days after the OTREC dropsondes were assimilated so it appears that the ERA5 reanalysis can successfully represent EW structure and its variability to some extent. OTREC dropsondes launched through cloudy vs clear air may also account for some of this difference.

**Table 3.1 LCL (hPa), CAPE (J kg$^{-1}$), and CIN (J kg$^{-1}$) at 4°N and 8°N from the three EWs at day +0 and +2 from OTREC RFs and ERA5**

| EWs | Day 0 | | | | | Day +2 | | | | |
|---|---|---|---|---|---|---|---|---|---|---|
| | Source (date) | Latitude | LCL | CAPE | CIN | Source (date) | Latitude | LCL | CAPE | CIN |
| EW 1 | OTREC | 8°N | 971 | 1934 | 0 | ERA5 | 8°N | 958 | 1713 | 0 |
| | (Aug. 7) | 4°N | 977 | 395 | -68 | (Aug. 9) | 4°N | 954 | 276 | -30 |
| EW 2 | ERA5 | 8°N | 968 | 1190 | 0 | OTREC | 8°N | 975 | 2259 | 0 |
| | (Aug. 15) | 4°N | 958 | 207 | -46 | (Aug. 17) | 4°N | 975 | 1053 | -12 |
| EW 3 | ERA5 | 8°N | 974 | 1182 | 0 | ERA5 | 8N | 956 | 1331 | 0 |
| | (Sep. 16) | 4°N | 972 | 62 | -36 | (Sep. 18) | 4°N | 947 | 303 | -44 |

The convective structures seen by the HCR are now examined, the cloud radar installed on the NSF/NCAR Gulfstream V aicraft. On 7 August, RF 1 sampled a large MCS located in the northern part of the OTREC box (Fig. 3.8a). In regions of deep convective structures and stratiform rain regions with a well-defined bright band near an altitude of 4.5 km (Fig. 3.8c), the radar was strongly attenuated in the lower troposphere given the nature of W-band retrievals in deep convective systems. The southern part of the OTREC box did not show deep convection (Fig. 3.8b) and was impacted by very dry mid-level air (Fig. 3.7c). The HCR observed shallow cumulus clouds with echo-top heights around 1 km (or 900 hPa) and cirrus clouds near 10 km (Fig. 3.8d). On 17 August, RF 3 sampled suppressed convection in the northern part of the OTREC box associated with the non-convective part of the EW that passed through two days before (Fig. 3.8e). The HCR detected isolated convective cells with echo-top heights near 6 km (Fig. 3.8g). In the southern part of the OTREC box (Fig. 3.8f), the HCR observed

shallow cumulus clouds with echo-top heights at 1.5 km (or 850 hPa) and cirrus clouds at 10 km. The shallow cumulus extended slightly higher than those seen during RF1, potentially because of the elevated trade inversion at day +2 (cf. Figs. 3.7c and d). Therefore, deep convection in the northern part of the OTREC box and muted shallow convection in the southern part of the OTREC box dominated at day 0 when the trough center of the EW was near. Deep convection at day 0 was accompanied by an enhanced deep circulation (Fig. 3.5f). Suppressed deep convection in the northern part of the OTREC box and enhanced shallow convection in the southern part of the OTREC box dominated at day +2 with the EW ridge passage. The shallow convection at day +2 was accompanied by a strong shallow circulation (Fig, 3.5k). A separate analysis with radar observations from the GPM satellite was performed over the East Pacific OTREC box during the three EWs and also found stronger and deeper shallow structures in the southern part of the ITCZ at day +2 compared to day 0 (not shown).

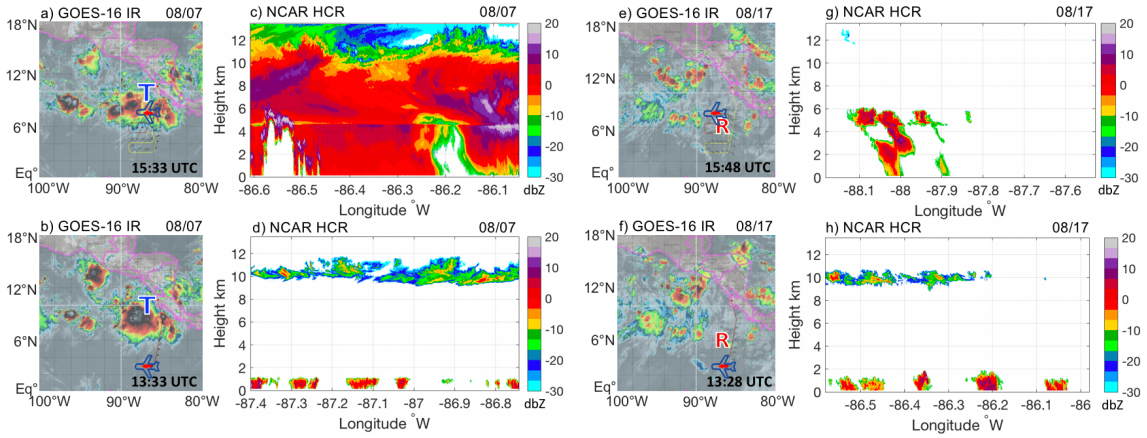


**Figure 3.8 (a-b, e-f) GOES IR images (red/dark colors indicate convective regions) and (c-d, g-h) vertical reflectivity cross sections in dBZ from the NCAR Hiaper Cloud Radar during enhanced precipitation on 7 August 2019 (i.e., positive phase of EW) and suppressed precipitation on 17 August 2019 (i.e., negative phase of EW) across the flight path indicated by the red arrow in the GOES IR images. The trough and ridge centers of the EW are labeled as T and R, respectively.**

### 3.4. Moisture budget

In this section, the moisture budget is examined to help understand why convection varies as a function of EW phase in climatologically shallow and deep regions. Many previous studies have shown that convection is favored when the lower free troposphere is moist (e.g., Holloway & Neelin, 2009; Raymond & Torres, 1998). (Rydbeck & Maloney, 2015) further suggest that the distribution of convection within EWs is strongly constrained by the moisture field. The moisture budget is represented as:

$$\left[\frac{\delta q}{\delta t}\right] = -[v_h . \nabla_h q] - \left[\omega \frac{\delta q}{\delta p}\right] + E + P \quad (1)$$

where $q$ is specific humidity, $v_h$ is horizontal wind, $\omega$ is vertical velocity, $E$ is evaporation and $P$ is precipitation. The brackets represent the mass-weighted vertical

integral from 1000 to 200 hPa. The term on the left-hand side of Eq. (1) represents the vertically integrated specific humidity tendency. The first term on the right-hand side of Eq. (1) is the moisture tendency resulting from horizontal advection and the second term on the right-hand side is the moistening by vertical advection. These terms have been calculated using finite centered differences. The third and fourth terms on the right-hand side are the column moisture tendency as a result of surface evaporation and precipitation, respectively. In this study, $E$ is not explicitly examined because it was previously shown to be of second order importance for determining the EW modulation of convection (Rydbeck & Maloney, 2015). Vertical advection minus precipitation has parallels to the sum of vertical advection and radiation in the column-integrated MSE budget, and has been referred to as the “column process" by some studies (e.g., Wolding et al., 2016).

The vertically-integrated moisture budget has been used to study regions with large precipitation produced by EWs. For example, Rydbeck and Maloney (2015) showed that anomalous horizontal advection has large contributions to the positive tendency of column-integrated moisture tendencies ahead of the EW convection, and to negative moisture tendencies behind the EW convection. Ahead of the cyclonic EW center, northeasterly flow advects moist air from the East Pacific warm pool, and behind the cyclonic EW center, southwesterly flow advects dry air from the East Pacific cold tongue. They also examined the difference between the tendency resulting from vertical advection and precipitation, calculated as the residual of the other terms in the budget to obtain the ``column process". Positive regions of this quantity indicate where anomalous

vertical advection is moistening the atmosphere more than anomalous drying by precipitation. Rydbeck and Maloney (2015) showed that while moistening not counteracted by precipitation preferentially occurs ahead of the wave trough, vertical advection minus precipitation is anomalously negative behind the wave trough. The difference between vertical advection and precipitation is substantially smaller than the total moisture tendency, suggesting that horizontal advection is the largest contributor to the positive tendency of column-integrated moisture tendencies ahead of EW convection.

This previous work implies in the context of the current study that shallow, non-precipitating convection might play a moistening role ahead of the wave because of anomalously large low-level moisture convergence and suppressed precipitation. On the other hand, regions of stratiform rain from deep convection with muted low-level moisture convergence and large precipitation might play a drying role behind the wave. Figure 3.9 shows the composite moisture tendency anomalies resulting from horizontal advection and from vertical advection minus precipitation. Precipitation from ERA5 is used in the moisture budget rather than IMERG because of the better physical consistency with the convergence field.

The spatial structure of the ERA5 precipitation was generally consistent with the IMERG precipitation structure in Fig. 3.5, however, ERA5 precipitation anomalies were up to 20% lower within the EW at days -1, 0, and +1 (not shown).

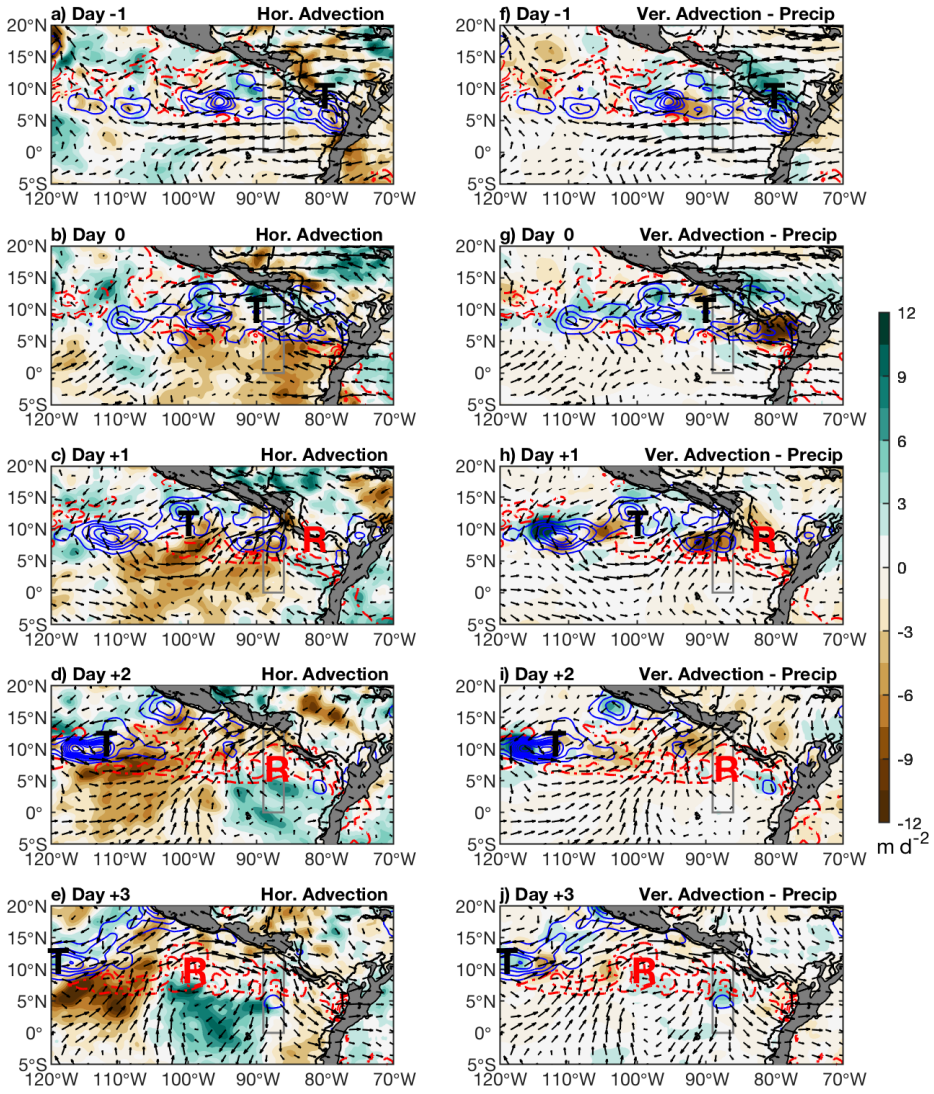


**Figure 3.9 Composite OTREC EW anomalies (shaded, in mm $d^{-1}$) of (a-e) moisture tendency from horizontal advection and (f-h) moisture tendency from vertical advection minus precipitation from day -1 to day +3 using ERA5 reanalysis. All images are superposed by 600-hPa wind vectors and ERA5 precipitation anomalies. Positive (negative) precipitation anomalies are in blue (red) contours, contours are every 10 (5) mm $d^{-1}$ starting at 5 mm $d^{-1}$. The trough and ridge centers of the EW are labeled as T and R, respectively. Largest wind vector is 5 m $s^{-1}$.**

At day -1 (Fig. 3.9a), the enhanced precipitation associated with the EW trough was located at 80°W and ERA5 precipitation (blue contours) showed a zonal band of precipitation at 8°N. While dynamical features resembling an EW at day -1 are generally weak, positive horizontal advection anomalies (shaded) were slightly less than 3 mm $d^{-1}$ ahead of the wave (i.e., west of the trough axis) and around -5 mm $d^{-1}$ behind the wave (i.e., east of the trough axis) near the South American coast. The difference between the vertical advection and precipitation (Fig. 3.9f) indicates anomalous moistening to the northwest (83°W, 10°N) of the convectively-active part of the EW trough. At day 0 (Fig. 3.5c), enhanced precipitation was associated with the EW trough centered near 90°W, next to the OTREC box. Negative horizontal advection anomalies increased over the southeastern part of this convectively active region (Fig. 3.9b). The vertical advection and precipitation mostly cancel each other at the EW trough axis around 90°W, Fig. 3.9g), but moistening by vertical advection exceeded drying by precipitation ahead of the wave, suggesting a region with large low-level convergence and weak precipitation (i.e., cumulus congestus). Behind the wave, anomalous precipitation exceeded vertical advection, resulting in drying, suggesting a region with anomalously weak low-level convergence and enhanced precipitation (stratiform structures). These horizontal patterns, while noisier given the smaller sample size, are consistent with (Rydbeck & Maloney, 2015) and propagated westward in association with the EW.

At day +1 (Fig. 3.9c), enhanced circulation and precipitation associated with the EW trough were oriented southwest-northeast. The EW trough was centered at 100°W, with anomalous negative horizontal moisture advection behind the wave trough also

oriented southwest-northeast. Over the OTREC box, anomalously negative horizontal moisture advection and 600-hPa southerly winds were predominant, consistent with intrusion of dry air from the equatorial region of the SST cold tongue. The difference between anomalous vertical advection and precipitation (Fig. 3.9h) suggests moistening by vertical advection exceeded drying by precipitation ahead of the wave. Behind the wave trough, precipitation exceeded vertical advection, resulting in drying. This behavior suggests shallow and stratiform structures ahead of and behind the wave trough, respectively. The stratiform structure behind the wave trough is consistent with Fig. 3.5j.

At days +2 and +3 (Figs. 3.9d and e), the convectively active part of the southwest-northeast oriented EW was centered around 110°W and 115°W (i.e., the trough), respectively. As on the previous days, anomalous negative horizontal moisture advection was observed behind the wave. Over the OTREC box, the precipitation was suppressed. In the northern part of the OTREC box, anomalous negative horizontal moisture advection predominated, and in the southern part, anomalous positive horizontal moisture advection predominated. Since the EW was tilted with height, the time-height diagram in Fig. 3.6g can also be interpreted as longitude-height diagram. The horizontal flow was mainly northerly at 850 hPa in the southern part and this was the main source of moistening. The structure of the horizontal advection field likely played an important role in regulating local shallow convection and circulation near 4-5°N (Figs. 3.5h-l, 3.8h). The difference between the vertical advection and precipitation (Figs. 3.9i and j) shows that moistening by vertical advection was small over the

OTREC box at day +2 and positive around 5°N at day +3, also suggesting the importance of shallow convection there (Fig. 3.8h) for fostering column moistening in addition to horizontal advection.

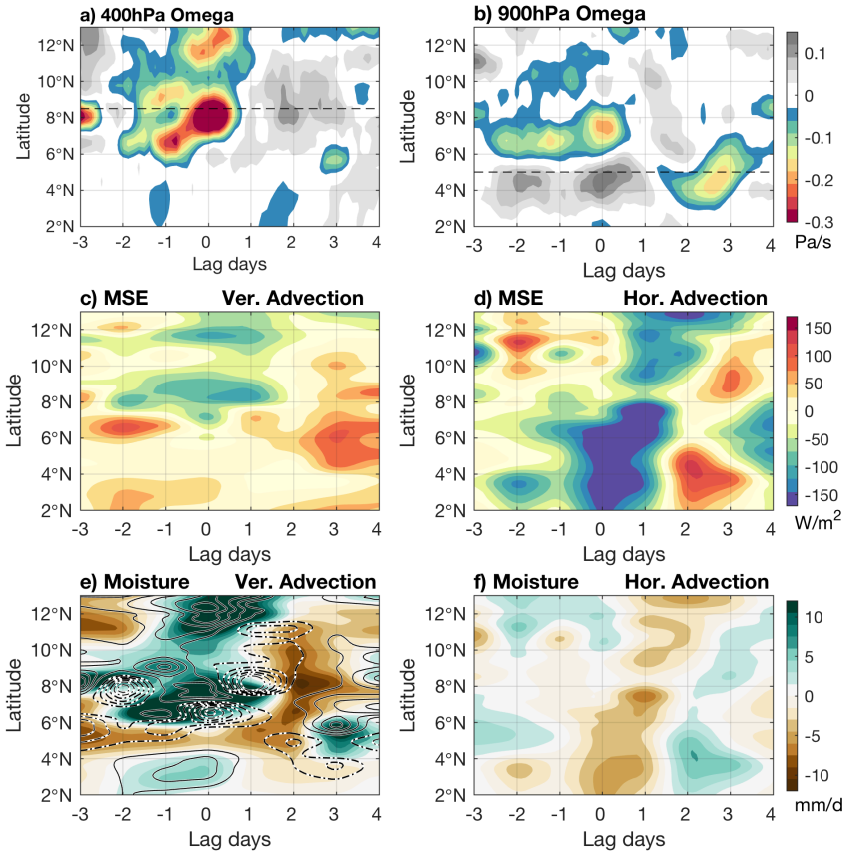


**Figure 3.10 Composite OTREC EW time-latitude diagrams over 89°-86°W of a-b) omega anomalies in Pa $s^{-1}$ at 400 hPa and 900 hPa (dashed lines indicate the climatological position of maximum omega at the determined level), c-d) vertical and horizontal advection of total MSE in W $m^{-2}$, e) anomalies of moisture tendency from vertical advection in mm $d^{-1}$ superposed by moisture tendency from vertical advection minus precipitation in mm $d^{-1}$ (contours every 2 mm $d^{-1}$, negative values dashed and positive values solid), and f) anomalies of moisture tendency from horizontal advection in mm $d^{-1}$.**

Figures 3.10a and b show the EW composite time-latitude plots of omega at 400 and 900 hPa that display deep and shallow convective structure evolution, respectively. In the OTREC average (Fig. 3.1), omega peaks at 400 and 900 hPa were located at 8.5° and 5°N, respectively (dashed lines in Figs. 3.10a and b). The vertical and horizontal advection of MSE calculated as in Back and Bretherton (2006) are shown in Figs. 3.10c and d. MSE is a thermodynamic variable that helps explain the interactions between convection and the large-scale circulation. The MSE budget has an advantage over the moisture budget in the deep tropics where temperature gradients are weak in that it accounts for the cancellation of vertical moisture advection and drying by precipitation in the its vertical advection term, especially when considered in conjunction with radiation (Wolding & Maloney, 2015). Additionally, the vertical advection of MSE is strongly related to the shape of the vertical motion profile in the ITCZ, and its use provides direct comparison to studies involving the vertical structure of the ITCZ and moist static stability (Back & Bretherton, 2006; Inoue & Back, 2015). Positive values indicate an import of MSE and maximum vertical velocity at low levels (i.e., a bottom-heavy structure), and negative values indicate the export of MSE with maximum vertical velocity at high levels (i.e., a top-heavy structure). Additionally, the moisture tendency resulting from vertical and horizontal advection (section 4) are shown in Figs. 3.10e and f, respectively. Vertical advection minus precipitation is shown in contours in Figure 3.10e.

For the deep convection regime at day 0 (Fig. 3.10a), the upper-level vertical velocity at 8°N is enhanced along with an anomalous export of MSE through vertical

advection (Fig. 3.10c). The export of MSE suggests that precipitation was stronger than vertical moisture advection, consistent with Fig. 3.10e (contours). For the climatological shallow convection region near 4-5°N, where the upward vertical motion is generally stronger at 900 hPa compared to 400 hPa, shallow convection was inhibited at day 0, especially at 4°N (Fig. 3.10b), with enhanced shallow convection at days +2 and +3 (cf. Figs. 3.5k-l). At day +2, the shallow convection region was characterized by an anomalous import of MSE (+100 W $m^{-2}$) and a positive moisture tendency resulting from horizontal advection (Figs. 3.10d and f) that would help support a deepening of the shallow clouds as suggested by the HCR data (Fig. 3.8h). The horizontal advection of MSE and the moisture tendency resulting from horizontal advection changed from negative values (< -150 W $m^2$ and -4 mm $d^{-1}$) at day 0 to positive values (+100 W $m^{-2}$ and +3 mm $d^{-1}$) at days +2 and +3. It is interesting to note that although the strongest shallow meridional overturning occurred on day +2 (Fig. 3.5k), the largest low-level vertical velocity occurred at day +3 (Fig. 3.5l). At day +3, the vertical moisture advection term was larger than the precipitation (Fig. 3.10e), consistent with the positive anomalous MSE import and indicative of the stronger congestus structures with large lower tropospheric vertical velocity.

### 3.5. EWs and the shallow and deep meridional circulations

The horizontal and vertical structure of EWs and ensuing moisture tendency field changes suggest substantial perturbations to the climatological deep and shallow circulations during wave passage (Figs. 3.5, 3.8 and 3.9). In this section, the mechanisms

responsible for the modification of deep and shallow circulations during the passage of EW are discussed in more detail. Figures 3.11a-d show total vertical velocity and relative humidity cross sections during the enhanced (day 0) and suppressed (day +2) convection periods associated with the passage of EWs across the OTREC box.

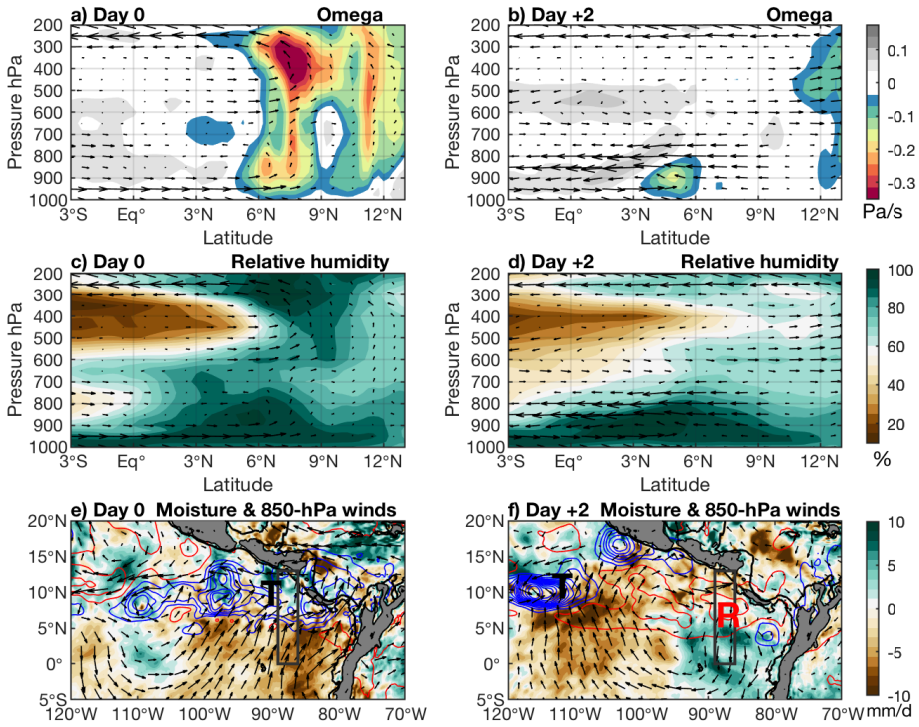


**Figure 3.11 Composite OTREC EW a-b) vertical velocity in Pa $s^{-1}$ and meridional flow, c-d) relative humidity in % averaged over 89°-86°W, and e-f) anomalies of moisture tendency from horizontal advection in shaded and vertical advection in contours superposed by winds at 850 hPa during day 0 and +2. Positive (negative) vertical advection anomalies are in blue (red) contours, contours are every 5 mm $d^{-1}$ starting at 3 mm $d^{-1}$. The trough and ridge centers of the EW are labeled as T and R, respectively. Largest wind vector is 6 m $s^{-1}$.**

At day 0, a deep circulation was observed in the ITCZ around 8°N with surface southerly inflow and return upper-level northerly outflow (Fig. 3.11a) and high relative

humidity throughout the troposphere (Fig. 3.11c). The moisture tendency anomaly resulting from vertical advection was positive (8 mm $d^{-1}$) in this deep convection region (Fig. 3.11e). Dry inflow between 600 and 400 hPa (Figs. 3.7c and 3.11c) was also observed that could have induced a positive feedback to a deep convective structure by inducing temperature anomalies as proposed by Zuidema et al. (2006) and Nolan and Rappin (2008). However, in the southern part of the ITCZ, where a shallow circulation is found in the climatology (i.e., around 6°N), negative horizontal moisture and MSE advection anomalies were apparent inhibited shallow convection (Fig. 3.8d). The shallow circulation had a weak northerly overturning flow at 850 hPa between 3 and 6°N associated with the cyclonic circulation around the trough of the EW that provided southerly wind anomalies (Fig. 3.11e) and weakened the shallow circulation overturning flow (Fig. 3.11a).

At day +2, the deep circulation was muted but a strong shallow circulation south of 5°N was observed with strong overturning northerly flow at 850 hPa (Fig. 3.11b). The shallow circulation associated with the shallow convection was likely inhibited from transitioning to deep convection due to the dry mid and upper level conditions imposed by the non-convectively active part of the EW (Fig. 3.11d). The climatological ITCZ axis (8 °N) was dominated by a negative tendency due to vertical advection and deep convection was also suppressed (Fig. 3.11f). However, horizontal advection anomalies were positive south of 5°N and likely helped maintain the shallow convection at day +2 (Fig. 3.8h). The strong northerly shallow overturning flow at 850 hPa was part of the EW horizontal structure that showed an anticyclonic circulation with strong northerly

flow at day +2 (Fig. 3.11f). The anticyclonic circulation was vertically tilted, with northerly flow at 850 hPa (600 hPa) that reached the OTREC box at day +2 (+3) as shown in Fig. 3.6. Additionally, the difference between vertical advection and precipitation suggests that this region was dominated by shallow structures that produced weak precipitation (i.e., shallow cumulus and stratocumulus clouds) but relatively strong low-level convergence at days +2 and +3 (Figs. 3.8h and 3.9i, j).

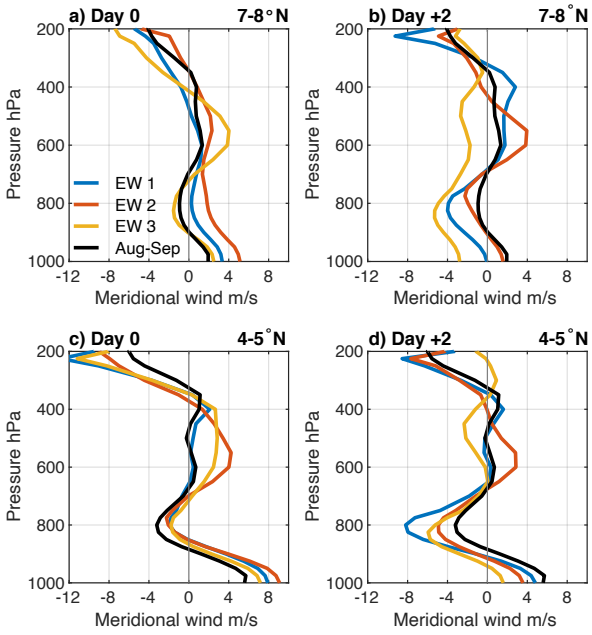


**Figure 3.12 Meridional wind profiles from ERA5 in m $s^{-1}$ at (a,b) 7 - 8°N, 89° - 86°W and (c, d) 4 - 5°N, 89° - 86°W for the three EWs and the August-September average during day 0 (a, c) and +2 (b, d).**

To show the consistency of the three EWs in modifying the climatological deep and shallow circulations in the East Pacific ITCZ, Fig. 3.12 compares the meridional wind profile of each wave at days 0 and +2 at 4 - 5°N (the shallow circulation region) and 7 - 8 °N (the deep circulation region) with the August-September 2019 mean profile.

On day 0 at 7 - 8°N (Fig. 3.12a), a deep circulation with southerly winds at low levels and northerly winds at upper levels was consistently produced across the three EWs. The deep circulations during the passage of EWs were stronger compared to the August-September average, especially during EW 1 and 2 with stronger low-level inflow. On day 0 at 4 - 5°N (Fig. 3.12c), there was weaker overturning flow near 800 hPa in the EWs compared to the August-September profile. At day +2, the deep circulation was weaker at 7 - 8°N (Fig. 3.12b), but the overturning flow around 800 hPa at 4 - 5°N was stronger after the passage of the EWs compared to the August-September profile (Fig. 3.12d).

### 3.6. Summary

This study aimed to identify synoptic variability associated with EWs during the OTREC field campaign and determine their impacts on the climatological deep and shallow circulations in the East Pacific. Using OTREC observations, ERA5 reanalysis, and satellite precipitation estimates, three strong EWs were identified. Although this study considers a limited number of EW events, it analyzes a period strongly constrained by in situ observations, and the mid-level vorticity and meridional wind structures examined are consistent across all the events during the OTREC field campaign.

Modulation of the climatological shallow and deep circulations in the far East Pacific at longitudes near the OTREC observational area were found during the passage of EWs, and a schematic that summarize the evolution of EWs is shown in Fig. 3.13. Normal conditions (Fig. 3.13a) represent the August-September 2019 mean (Fig. 3.1b),

with a shallow circulation near 6°N below 850 hPa and a deep circulation at 8°N between the surface and 200 hPa. Positive low-level vorticity (i.e., cyclonic circulation) is also characteristic of climatological conditions Raymond et al. (2014), with associated surface westerly winds at 7°N. Easterly winds occur near the equator between 700 and 600 hPa.

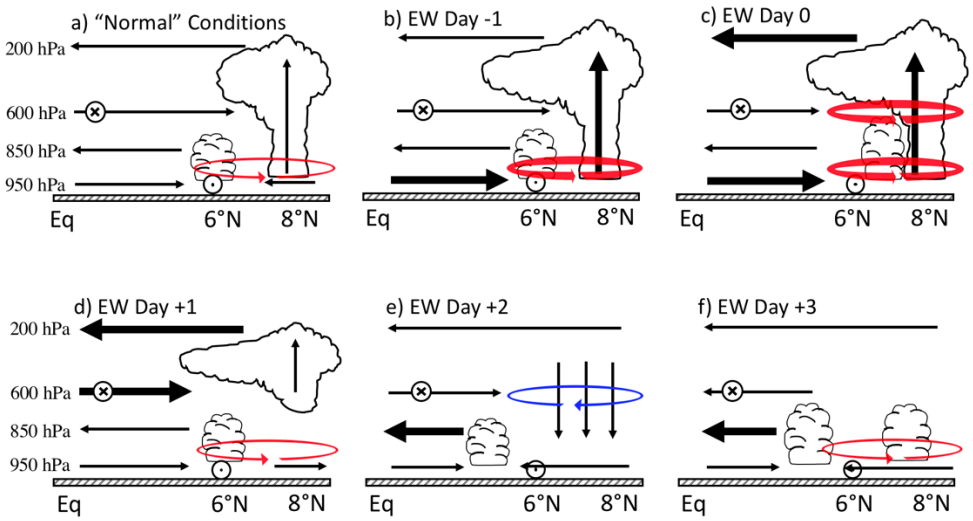


**Figure 3.13 Latitude-height sketch of the evolution of EWs and their effect on shallow and deep circulations in the East Pacific. Horizontal (vertical) bold vectors indicate total meridional winds (upward motion) larger than 8 m $s^{-1}$ (0.3 Pa $s^{-1}$). Positive (negative) total vorticity is shown in a red cyclonic (blue anticyclonic) vertical vorticity features and bold trajectories indicate vorticity of magnitude larger than 4 x $10^{-5}$ $s^{-1}$. The EW horizontal scale is approximated by the size of vorticity features. The clouds denote the position of the shallow and deep convection. Encircled x's (dots) denote westward (eastward) winds.**

The EWs during OTREC strongly modulated these seasonal mean conditions. At day -1 of the EW evolution (Fig. 3.13b), deep convection was enhanced at 8°N and the total low-level positive vorticity (Fig. 3.6a) was stronger than climatology and associated with intensified near-surface westerly flow. At day 0 (Fig. 3.13c), the trough of the EW

was associated with enhanced deep convection at 8°N and the shallow convection was displaced north of 6°N. This alteration is associated with the export of column integrated MSE by vertical advection. Positive vorticity predominated near the surface and at 600 hPa in the region of deep convection, associated with intensifying near-surface westerly flow just to the south of the deep convective region. At day +1 after the passage of the trough (Fig. 3.13d), deep convection decayed and stratiform clouds predominated at 8°N, with the net effect of vertical moisture advection and precipitation producing drying. Enhanced mid-level southerly inflow associated with the EW structure (Figs. 3.5g, j) and upper-level northerly outflow also occurred. At day +2 (Fig. 3.13e), positive values of moisture and MSE fields supported by horizontal advection in the EW ridge likely enhances shallow convection at 4°N. The strong shallow overturning circulation at 850 hPa was coupled with an EW anticyclonic structure that drove strong northerly winds between 700 and 800 hPa (Figs. 3.6g and 3.11f). At day +3 (Fig. 3.13f), weak convection was observed at 8°N, although the positive low-level vorticity recovered. The shallow circulation was still prominent associated with deeper and stronger shallow convection.

This schematic is consistent with the climatological deep and shallow circulations being modified by the passage of EWs in the East Pacific. The troughs of EWs enhanced the ITCZ deep circulation at day 0 and was associated with an export of column integrated MSE by vertical advection; however, the shallow circulation in the southern part of the ITCZ was weak due to a negative moisture tendency from horizontal advection over the southern part of the ITCZ. On the other hand, the suppressed part of

the EW enhanced the shallow circulation at day +2. The shallow overturning flow at 850 hPa was linked to the anticyclonic circulation of the EW. A positive anomalous moisture tendency that resulted from horizontal advection and import of MSE helped drive shallow convection over the southern part of the ITCZ. This MSE import was consistent with moistening by vertical advection that outpaced precipitation, which is suggestive of an enhancement of shallow convection that fostered column moistening at day +3. Our results indicate that the three EWs altered the East Pacific ITCZ circulation in this way consistently. Even though ERA5 did not assimilate OTREC data during all the EWs, it appears capable of capturing the salient structures and variations of the EWs during this time. Future work will involve the identification of EWs during a longer time period using satellite precipitation and reanalyses to confirm the systematic alteration of the shallow and deep circulation during the passage of EWs in the East Pacific ITCZ.

CHAPTER IV

# ASSESSING THE VERTICAL VELOCITY IN THE EAST PACIFIC ITCZ*

## 4.1. Background

The vertical structure of the vertical velocity in the East Pacific (EP) ITCZ has been highly debated, mainly because of the disagreement between reanalysis and satellite datasets (e.g., Hagos et al., 2010). While satellite-based studies show a predominance of deep ascending motion associated with deep convection (Liu et al., 2015; Schumacher et al., 2004), reanalyses suggest strong shallow ascending motion (Back & Bretherton, 2006; Yokoyama et al., 2014). Schumacher et al., 2004) used observations from the precipitation radar aboard the Tropical Rainfall Measurement Mission (TRMM) satellite to estimate vertical profiles of latent heating and showed top-heavy heating associated with deep ascending motion in the EP ITCZ. Back and Bretherton (2006) used ERA-40 and NCEP-NCAR reanalyses to study the vertical structure of the EP ITCZ and showed maximum ascending motion at 850 hPa associated with an import of moist static energy (MSE) through vertical advection. This shallow ascending motion is linked to a shallow meridional overturning circulation in the southern part of the EP ITCZ and is supported by the East Pacific Investigation of Climate Processes in the Coupled Ocean – Atmosphere System (EPIC-2001) field campaign dataset (Zhang et al., 2008).

---

* A version of this chapter has been submitted for publication in the *Geophysical Research Letters*.

In a more recent study using EPIC-2001 and other in situ data, Huaman and Takahashi (2016) showed a second vertical motion peak above the shallow ascending motion peak. Additionally, Huaman and Schumacher (2018) used 16 years of CloudSat and TRMM satellite radar observations to estimate vertical profiles of latent heating in the EP ITCZ. They combined shallow precipitation from the CloudSat W-band radar and deep (i.e., convective and stratiform) precipitation from the TRMM $K_u$-band radar to more accurately represent latent heating from the full convective spectrum. Their results demonstrated that two peaks of latent heating associated with deep and shallow ascending motion are apparent in this region and linked to deep and shallow meridional circulations. They also found that the vertical structure of the EP ITCZ is tilted meridionally; shallow ascending motion occurs around 6°N in the southern part of the ITCZ and transitions to deep ascending motion around 9°N in the northern part of the ITCZ. Using reanalysis data, Trenberth et al. (2000) also identified the shallow and deep mode in the global monsoon, including in the EP ITCZ. The shallow and deep modes over the EP ITCZ experiences interannual, seasonal, and synoptic variability. Schumacher et al., (2004) showed an increase of stratiform rain fraction (and thus a deeper vertical mode) during El Niño years over this region. Huaman and Schumacher (2018) studied the seasonal variability of the vertical velocity associated with convection in the EP ITCZ and found a predominance of shallow mode during boreal winter and spring, and deep and shallow mode during boreal summer and fall. Additionally, Huaman et al., (2020) showed that convectively coupled Kelvin waves impact the

meridional circulation in the EP ITCZ, enhancing the shallow ascending motion ahead of the Kelvin wave and deep ascending motion within the Kelvin wave.

The vertical structure of the meridional circulation is important to the MSE budget, and thus to the theoretical questions about the relationship of convection to large-scale dynamics (Frierson, 2007; Inoue & Back, 2015; Neelin & Held, 1987; Numaguti, 1993; Raymond et al., 2009; Sobel, 2007). However, it has been a challenge to determine which dataset among reanalyses and satellite products is closer to the truth because of the lack of in situ observations over the EP. The lack of in situ observations causes reanalysis datasets to rely heavily on the physical parameterizations of models that might not represent the actual conditions. Additionally, latent heating algorithms from the TRMM and Global Precipitation Measurement (GPM) satellites are based on look-up tables from cloud-resolving models (CRMs) that might not be representative of the EP ITCZ. Therefore, more studies based on in situ observations are needed to improve our understanding of the vertical velocity and convection over this region and examine the reliability of vertical motion from multiple reanalyses and satellite products. In this study, I analyze the vertical velocity observed during the OTREC 2019 field campaign to determine which product is closer to the OTREC observations and thus more likely to represent the true meridional overturning structure in the EP ITCZ.

### 4.2. Data and Methodology

I used observationally-based vertical velocity (i.e., vertical pressure velocity in Pa $s^{-1}$) from an OTREC 3DVar analysis processed by New Mexico Tech (Fuchs-Stone et

al., 2020), which was generated from gridded dropsonde data collected from NSF/NCAR Gulfstream V flights between 12 and 18 UTC (06 and 12 local time). Flight operations took place from 5 August to 3 October 2019 and twelve research flights (RFs) were performed over the EP OTREC flight box (89° - 86°W, 3° - 11°N; Fig. 4.1a). However, only considered nine research flights were considered: RF02 (12 August), RF05 (17 August), RF08 (23 August), RF14 (21 August), RF16 (24 August), RF18 (27 August), RF19 (28 August), RF21 (1 October), and RF22 (2 October). RF01 (7 August) and RF20 (30 September) were excluded because their extreme precipitation deviated significantly from the other RFs and from the precipitation climatology calculated using daily IMERG precipitation data (Huffman 2015) from 1998 to 2019. RF11 (4 September) was also excluded due to missing data north of 8°N.

Vertical velocity fields for 2014 to 2020 were obtained from the following reanalyses: ERA5, MERRA-2, JRA-55, and NCEP-NCAR. Table 1 lists the spatial and temporal resolution and convection and assimilation schemes for each reanalysis. All the reanalyses are interpolated to 0.5° for comparison of specific latitudinal ranges, but note that JRA-55 and NCEP-NCAR have significantly coarser resolution than this. Additionally, I only analyze reanalysis data during the OTREC flight times (12 to 18 UTC) in order to exclude variations in vertical motion due to the diurnal cycle (not shown).

**Table 4.2 Reanalyses and GPM latent heating products**

| Reanalysis | Resolution | Convective scheme | Assimilation scheme |
|---|---|---|---|
| ERA-5 (Hersbach et al., 2020) | 0.28°x0.28°, 1h 137 pressure levels | Upgraded Mass Flux (Tiedtke, 1989) | 4-D |
| MERRA-2 (Gelaro et al., 2017) | 0.5°x0.625°, 3h 72 pressure levels | Relaxed Arakawa-Schubert (Moorthi & Suarez, 1992) | 3-D |
| JRA5-55 (Kobayashi et al., 2015) | 1.25°x1.25°, 3h 137 pressure levels | Prognostic Arakawa-Schubert (Arakawa & Schubert, 1974) | 4-D |
| NCEP-NCAR (Saha et al., 2014) | 2.5°x2.5°, 6h 17 pressure levels | Simplified Arakawa-Schubert (Pan & Wu, 1995) | 3-D |
| **GPM Algorithm** | **Resolution** | **Satellite Input** | **Heating Look-up Table** |
| CSH (Tao et al., 2001; 2010) | 0.25°x0.25°, 1h 80 pressure levels | Surface precipitation<br>Rain Type (Shallow, convective, stratiform, anvil) | CRM |
| SLH (Shige et al.,2004; 2007) | 0.25°x0.25°, 1h 80 pressure levels | Surface precipitation<br>Rain Type (Shallow, convective, stratiform, anvil)<br>Precipitation-top height<br>Melting level | CRM |
| HS2018 (Huaman & Schumacher, 2018) | 0.25°x0.25°, 1h 80 pressure levels | Surface precipitation<br>Rain Type (Shallow, convective, stratiform, anvil) | Obs |

Hourly latent heating retrievals from GPM are also used. The GPM satellite was launched in 2014 (Hou et al., 2014) and is equipped with a dual-wavelength radar that provides the observational basis of the latent heating retrievals. The swath width of the radar is relatively narrow (245 km) and the satellite orbit precesses through the diurnal cycle, which limits sampling over the OTREC flight box, especially when only 12-18 UTC overpasses are considered. The GPM latent heating algorithms used are: Convective Stratiform Heating (CSH), Spectral Latent Heating (SLH), and a novel

algorithm developed by Huaman and Schumacher (2018; HS2018). The resolution and input data for the algorithms are detailed in Table 1. Hourly precipitation from IMERG and daily SST from OSTIA (Donlon 2012) were also used during the OTREC period.

Vertical velocity was estimated from the GPM latent heating retrievals using a simplified thermodynamic equation from Huaman and Takahashi (2016): $\frac{\omega}{\rho g}\frac{dln(\theta)}{dz} = \frac{LH}{T}$, where $\rho$ is density, $g$ is the gravitational force, $\theta$ is potential temperature, $z$ is height, $LH$ is latent heating, and $T$ is the air temperature. $T$ and $\theta$ were obtained from ERA-5. It is assumed that the vertical advection of potential temperature balances the latent heating (i.e., neglecting horizontal advection, turbulent diffusion, and radiative tendencies; Houze, 1989). The results are not sensitive to the temperature used from different reanalyses.

### 4.3. Vertical velocity during OTREC

Figure 4.1a shows the average IMERG precipitation across the EP for the nine analyzed OTREC RFs. In the OTREC flight box, the maximum precipitation was located north of 7°N, where SST is warmest. There were no significant intraseasonal (e.g., Madden-Julian Oscillation) or interannual (e.g., El Niño) events during OTREC, and the average precipitation during the field campaign was fairly consistent with the IMERG precipitation climatology from 1998-2014 (not shown). The mean vertical structure of the vertical velocity from OTREC dropsondes and reanalyses during the nine RFs is shown in Figs. 4.1b-f. The spatial resolution of the reanalyses ranges from

0.28° to 2.5°; therefore, the vertical velocities values are smoother in the reanalyses with lower resolution.

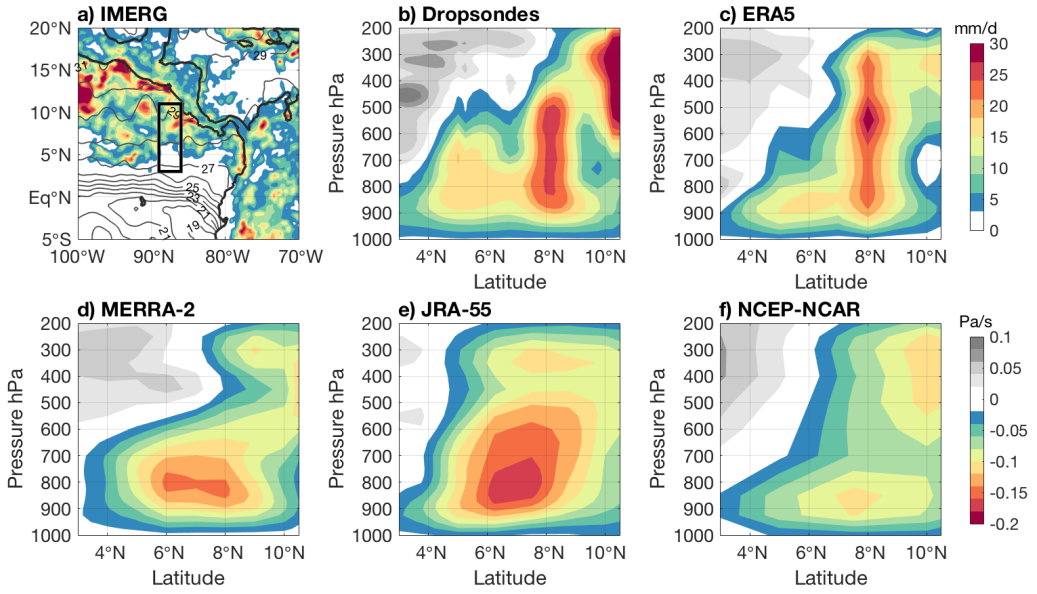


**Figure 4.1 a) Precipitation from IMERG in mm $d^{-1}$ (shaded) and SST in C° (contours). The black box indicates the OTREC flight box. b-f) Vertical cross sections of vertical motion in Pa $s^{-1}$ across 89°W-86°W from OTREC dropsondes and the four analyzed reanalyses (ERA5, MERRA-2, JRA-55, and NCEP-NCAR) averaged over the nine RFs.**

The vertical velocity retrieved from OTREC observations (Fig. 4.1b) suggests a meridional slope with shallow vertical motion between 4°N and 7°N, and deepening farther north at 8°N in the lower and mid troposphere and at 10.5°N in the mid and upper troposphere. The meridional structure of vertical motion during OTREC was generally captured by ERA5 (Fig. 4.1c), which shows weak shallow upward motion centered at 6°N and strong deep upward motion at 8°N. ERA5 assimilated OTREC dropsonde data, thus helping it capture the observed vertical motion structure, although the upward

motion between 600 and 200 hPa at 10.5°N is much weaker in ERA5 compared to the OTREC dropsonde retrieval. JRA-55 (Fig. 4.1e) also assimilated the OTREC dropsondes (Japan Meteorological Agency, personal communication), but its vertical motion is less consistent with OTREC observations. MERRA-2 and NCEP-NCAR (Figs. 4.1d and f) did not assimilate OTREC in situ data (NASA/GSFC for MERRA-2 and National Centers for Environmental Prediction for NCEP-NCAR, personal communication) and exhibit predominantly shallow vertical motion around 7°N and weaker deep vertical motion around 10°N. The weak vertical motion in NCEP-NCAR is likely in part due to the 2.5°x2.5° resolution, which smooths the vertical velocity values.

The different vertical motion structures between the reanalyses can be attributed to the range of resolutions, convective schemes, and/or assimilation methods employed (Table 1); however, it is not clear which factor plays the predominant role. Precipitation from each reanalysis also shows differences (not shown). ERA5 has the highest temporal, spatial, and vertical resolution and all the reanalyses have unique convective schemes. ERA5 and JRA-55 use a four-dimensional variational (4D-Var) data assimilation scheme, while MERRA-2 and NCEP-NCAR use a three-dimensional variational (3D-Var) scheme. Both ERA5 and JRA-55 assimilated the OTREC dropsondes and employ 4D-Var so the disagreement between ERA5 and JRA-55 is probably more related to the convective scheme and spatial resolution.

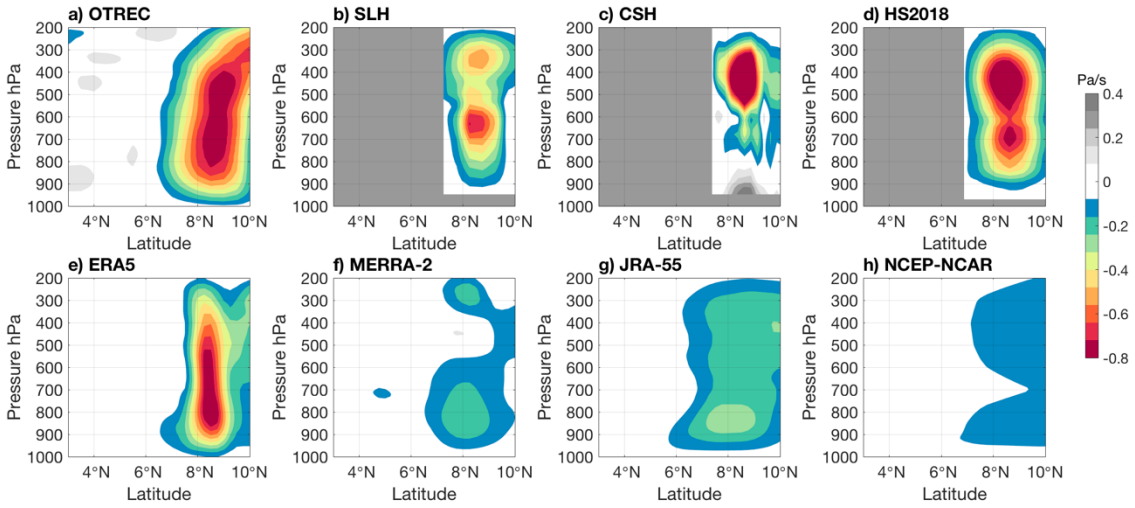


**Figure 4.2 Vertical cross sections of vertical motion in Pa $s^{-1}$ across 89°W-86°W during RF14 (21 September 2019), from a) OTREC dropsondes, b-d) GPM algorithms (SLH, CSH, and HS2018), and e-h) reanalyses.**

Only RF 14 (21 September 2019) coincided with a GPM overpass in the OTREC flight box and 12-18 UTC time window. Vertical velocity profiles from OTREC dropsondes, GPM algorithms and reanalyses on 21 September are shown in Fig. 4.2 and indicate active deep ascending motion in the northern portion of the OTREC box. OTREC observations (Fig. 4.2a) show strong upward motion, up to -0.9 Pa $s^{-1}$, throughout the troposphere. GPM products also show strong deep vertical motion. SLH (Fig. 4.2b) has upward motion throughout the troposphere, although less intense than the OTREC dropsondes, with a vertical velocity peak around 650 hPa. CSH (Fig. 4.2c) shows strong upward motion around 400 hPa and weaker downward motion from 700 hPa to the surface due to evaporative cooling below cloud base in the stratiform rain region. HS2018 (Fig. 4.2d) has strong upward motion through the depth of the troposphere, similar to OTREC observations.

Reanalyses indicate different vertical motion structures on this day, except ERA5. ERA5 vertical velocity (Fig. 4.2e) shows strong upward motion with values up to -0.9 Pa $s^{-1}$ from 850-500 hPa, similar to OTREC but shifted slightly lower in the troposphere. MERRA-2, JRA-55, and NCEP-NCAR (Figs. 4.2f-h) show weak vertical velocities with values between -0.1 Pa $s^{-1}$ and -0.3 Pa $s^{-1}$ and a predominant shallow mode peaking at 850 hPa throughout the EP ITCZ. The disagreement between reanalyses is partially explained by the resolution dependency in each reanalysis. However, JRA-55 provides a more realistic vertical motion profile than MERRA-2 despite its coarser resolution, suggesting that some benefit is still being provided through assimilation of the OTREC dropsonde data.

### 4.4. Monte Carlo Analysis

Although I presented a comprehensive case study from the OTREC field campaign in Section 3, the comparison to GPM data was limited by the near absence of coincident overpasses. In an attempt to make a more representative comparison, I looked for all the GPM radar overpasses in the OTREC flight box and 12-18 UTC time window for August and September during 2014-2020, and found 42 samples. The vertical velocity average derived from the GPM latent heating algorithms for the 42 overpasses is shown in Figs. 4.3b-d. Vertical velocity averages from MERRA-2, JRA-55, and NCEP-NCAR for the same GPM dates are shown in Figs. 4.3e-h. For easier comparison with the OTREC observations, the OTREC vertical motion average is repeated from Fig. 4.1b as panel Fig. 4.3a.

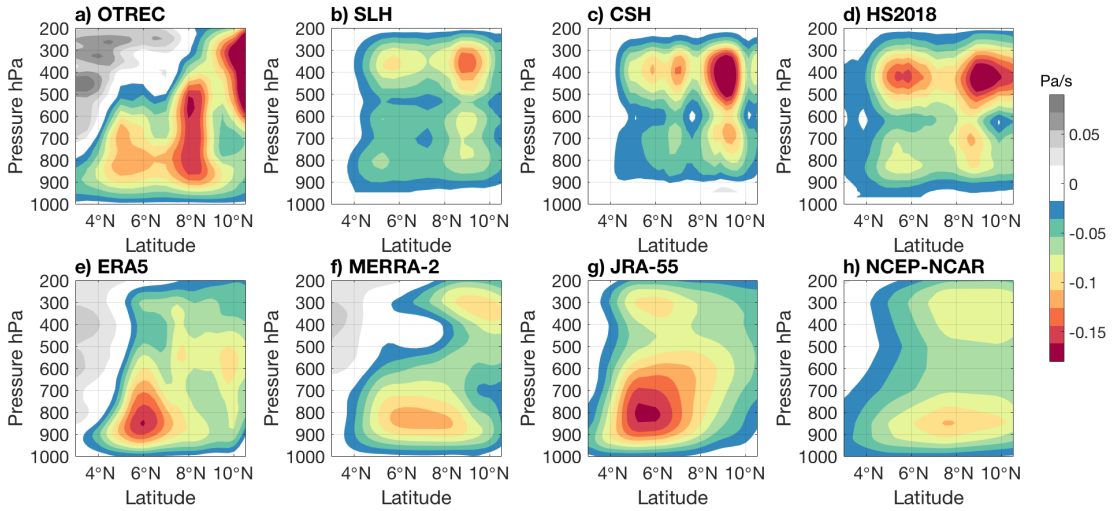


**Figure 4.3 Vertical cross sections of vertical motion in Pa $s^{-1}$ across 89°W-86°W from a) OTREC dropsondes averaged over the 9 RF samples, b-d) GPM algorithms and e-h) reanalyses averaged over 42 day samples between 2014 and 2020.**

Figure 4.3 shows that all of the GPM algorithms produce deep upward motion at 6°N and 9°N. Shallow upward motion predominates in the reanalyses around 6°N and is stronger in JRA-55 and ERA5 than MERRA-2 and NCEP-NCAR. The vertical velocity climatologies for 2014-2020 are similar to the 42-day averages in all of the reanalyses (not shown). Figure 4.3 calls attention to the significant disagreement between GPM algorithms and reanalyses. While reanalyses generally suggest stronger shallow vertical motion over much of the EP ITCZ, GPM algorithms indicate a predominance of deep vertical motion.

To conduct a more robust assessment of the vertical velocity in the EP ITCZ, I performed a Monte Carlo analysis in which numerous random samples of data that were expected to be comparable with the OTREC field campaign data are constructed. The

results of this analysis for three latitude bands (i.e., 4°N-7.5°N, 7.5°N-9°N, and 9°N-10.5°N) are shown in Fig. 4.4. I performed a 9-day average 1000 times and display the results as a set of colored points every 100 hPa representing the minimum average, 25th percentile, mean, 75th percentile, and maximum average vertical motion value for each GPM algorithm and reanalysis. I interpret as a good approximation of vertical velocity from the GPM algorithms or reanalysis data when their mean is inside the OTREC standard error range and their interquartile range (i.e., the range between the 25th and 75th percentiles) includes the OTREC mean.

In the southern part of the EP ITCZ (4°N-7.5°N; Fig. 4.4a), the OTREC dropsondes indicate a well-defined shallow vertical motion peak with a vertical velocity up to -0.1 Pa $s^{-1}$ at 850 hPa. The Monte Carlo distributions of the GPM satellite products show a vertical velocity around -0.05 Pa $s^{-1}$ at 850 hPa and closer to -0.1 Pa $s^{-1}$ above 500 hPa; however, the dispersion distribution is wide at higher levels. Thus, the GPM vertical motion is too weak at low levels and too strong aloft compared to the OTREC observations. At low levels, the underestimation is likely associated with the sensitivity of the radar installed on GPM. To test this theory, I replaced the GPM shallow precipitation with the climatological CloudSat shallow precipitation from Huaman and Schumacher (2018) for August and September making the total precipitation the sum of the GPM stratiform, GPM convective, and CloudSat shallow precipitation. The extra shallow precipitation measured by CloudSat increases latent heating at low levels and therefore vertical velocity (open circles in Fig. 4.4a) and is more consistent with OTREC observations. At higher levels, the OTREC observations indicate descending motion on

the order of 0.05 Pa $s^{-1}$ and dry conditions (not shown). Radiative cooling in our simplified thermodynamic equation is disregarded, which likely contributes to the overestimation of vertical velocity from GPM algorithms at upper levels.

All of the reanalysis Monte Carlo distributions show a shallow peak of vertical velocity at 850 hPa from 4°N-7.5°N (Fig. 4.4a) that is consistent with the OTREC observations and only JRA-55 mean values are outside of the OTREC dispersion range. Above 550 hPa, vertical velocities from reanalyses are larger than the OTREC observations and may be related to the small static stability of the atmosphere (i.e., $d\theta/dz$) retrieved by the reanalyses over this region. The vertical motion can be approximately determined by dividing the diabatic heating rate ($d\theta/dt$) by the static stability of the atmosphere (Mapes & Houze, 1995; Raymond et al., 2005; Sobel et al., 2001). When the reanalysis static stability is very small, as it tends to be in the tropical upper troposphere (because the moist adiabats become close to dry adiabats at low temperature), vertical motion is large even if the diabatic heating is small, and any signals (or errors) in the heating will be amplified by the small denominator.

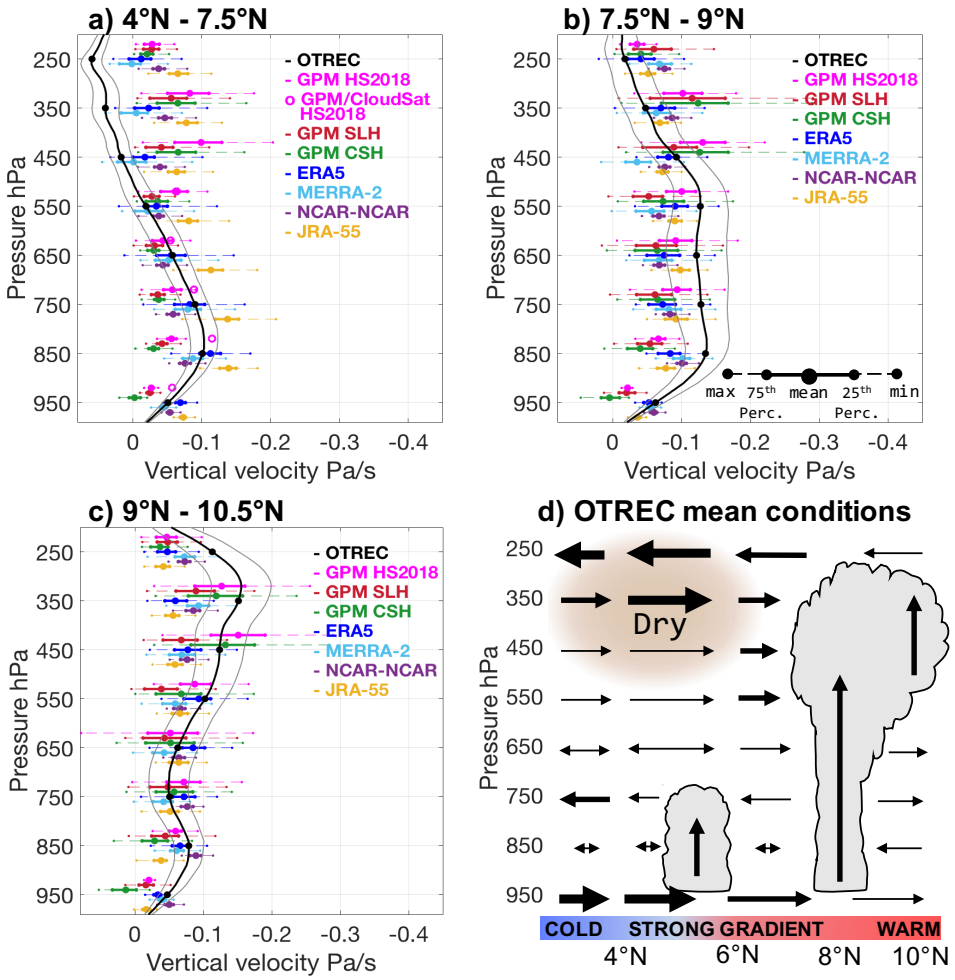


**Figure 3.4 Distribution of vertical motion with height in Pa $s^{-1}$ at a) 4°N-7.5°N, b) 7.5°N-9°N and c) 9°N-10.5°N in the EP ITCZ based on Monte Carlo analysis using 42 samples between 2014 and 2020 from the GPM algorithms and reanalyses. Each set of points represent the minimum average, 25th percentile, mean, 75th percentile, and maximun average. The black profile shows the OTREC vertical velocity 9-day sample mean with standard error in gray lines. c) Sketch of the OTREC mean conditions of the meridional overturning circulation over the East Pacific ITCZ. The thin, thick, and thickest horizontal vectors indicate meridional winds smaller than 2 m $s^{-1}$, between 2 and 4 m $s^{-1}$, and larger than 4 m $s^{-1}$, respectively. The short double arrow indicates meridional winds around 0 m $s^{-1}$.**

In the northern part of the ITCZ, OTREC dropsondes show two deep vertical motion peaks at 7.5°N-9°N and 9°N-10.5°N (Fig. 4.3a), which are retrieved by the GPM satellite products as single deep peak between 7.5°N and 10.5°N (Figs. 4.3b-d). Between 7.5°N and 9°N (Fig. 4.4b), OTREC upward motion is around 0.12 Pa $s^{-1}$ between 850 hPa and 550 hPa and the vertical motion from the reanalyses and GPM Monte Carlo simulations are generally too weak. The GPM underestimation is not fully explained by the shallow precipitation from CloudSat, which is similar to the GPM precipitation over these latitudes. It is unclear why the reanalyses become too weak at low levels in this region. Above 450 hPa, GPM satellite products remain overly strong, whereas the reanalyses become more consistent with OTREC observations.

Between 9°N and 10.5°N (Fig. 4.4c), the OTREC observations show deep upward motion with a maximum at 350 hPa, a profile that is normally associated with organized convective systems. However, a small secondary peak at 850 hPa suggests the presence of at least some shallow convection. The GPM Monte Carlo distributions for CSH and HS2018 are generally consistent with the OTREC dropsondes throughout the profile, whereas SLH becomes too weak aloft. Reanalyses are back to being consistent with the OTREC observations below 550 hPa, but become weaker above. The average of the two OTREC deep vertical motion peaks between 7.5°N and 10.5°N also suggest a deep mode average. Overall, the deep mode structure shown by the OTREC observations is supported by the GPM algorithms, but not by reanalyses.

Figure 4.4d presents a diagram of the overturning meridional circulation of the EP ITCZ based on OTREC observations. Winds were southerly at the surface, consistent

with (Raymond 2004), and extended up to 850 hPa. The southerly surface trade winds converged around 5°N, where the meridional SST gradient is strong, and northerly return flow was present around 750 hPa. A southerly midlevel inflow was seen between 550 and 350 hPa, consistent with (Huaman and Takahashi 2016). Above the shallow circulation, a dry layer associated with the descending motion of the Walker circulation (Wang & Enfield, 2003) was predominant. A deep circulation was seen to the north with deep vertical motion at 8°N and 10°N where SST is warmest, with a strong overturning and diverging circulation around 250 hPa.

### 4.5. Summary

I assessed the vertical velocity structure in the EP ITCZ using dropsondes from the OTREC 2019 field campaign, latent heating retrievals from the GPM satellite radar, and vertical velocity fields from reanalyses. OTREC observations indicated a shallow mode from 3-7°N, over a strong meridional gradient in SST, but a deep mode farther north, where the SST is warmest. However, all the reanalyses showed a predominant shallow mode from 3-10°N across the EP ITCZ unless they assimilated the dropsondes, as was done by ERA5 and JRA-55. Then a weak deep mode was found around 8°N. The reanalyses represent a range of resolutions, convective parameterizations, and assimilation schemes so it is unclear why they all have difficulty deepening convection over the EP ITCZ. Vertical motion derived from the GPM latent heating algorithms indicated deep vertical motions from 3-10°N. The lack of a shallow mode is due to the inability of the GPM radar to sense weakly precipitating shallow convection, but the

addition of cloud radar data can ameliorate the issue. The OTREC 2019 field campaign observations were crucial to identify deficiencies in the reanalyses and GPM algorithms. Reanalyses, especially MERRA2 and NCEP-NCAR, underestimate the deep vertical motion seen in the northern part of the EP ITCZ and GPM algorithms, especially GPM CSH, underestimate the shallow vertical motion in southern part of the EP ITCZ. The inability of reanalyses to retrieve the correct vertical velocity structure is likely related to the physical parameterizations and spatial resolution of the parent models, while the satellite retrievals suffer from the underestimation of light precipitation associated with the sensitivity of the radars onboard the TRMM and GPM satellites.

# CHAPTER V

# DIURNAL VARIATION OF THE MERIDIONAL FLOW AND RAINFALL OVER WEST AFRICA DURING THE PRE-MONSOON AND MONSOON SEASONS

## 5.1. Background

Precipitation and the meridional overturning over West Africa vary seasonally. During the pre-monsoon season (boreal spring), precipitation is predominant offshore in the Gulf of Guinea (e.g., Schumacher & Houze, 2006; Thorncroft et al., 2011). Inland, a dry SMC is observed and its shallow return flow penetrates into the latitude of deep convection (and thus deep overturning) to the south (Zhang et al., 2008). The upward motion of the SMC is associated with the West African heat low, which predominates near the surface (Lavaysse et al., 2009). Precipitation is inhibited over this region.

During the monsoon season (boreal summer), shallow and mid-level non-precipitating stratiform clouds dominate offshore in the Gulf of Guinea (Fink et al., 2017). Inland, there is maximum thunderstorm and shower activity (i.e., the West African monsoon) associated with deep meridional overturning and low-level inflow from the Gulf of Guinea. The SMC West African heat low are located farther north. Indeed, the West African heat low is located over the Sahara and is called Saharan heat low during the monsoon season. Above the Saharan heat low, at 700 hPa, an anticyclonic circulation predominates and its strong easterly flow is known as the African easterly jet (AEJ). The AEJ is formed due to the strong thermal contrast and soil moisture gradient in response to the low-level heating over the Sahara (Vizy & Cook,

2002). The combination of the diabatically forced meridional circulation associated with the surface fluxes and dry convection in the Saharan heat low is crucial to maintain the AEJ (Thorncroft & Blackburn, 1999).

Precipitation and winds over West Africa can also vary diurnally (Bouniol et al., 2012; Collow et al, 2016; Gounou et al., 2012; Janiga & Thorncroft, 2014; Laing et al., 2018; Liu et al., 2015, 2020; Pfeifroth et al., 2016; Sultan et al., 2007; Vizy & Cook, 2019; Vondou et al., 2010). For example, Yang and Slingo (2001) used brightness temperature observations from satellite to show a late evening rain maximum over West Africa during June-August. This is the time when mesoscale convective systems contribute the most rain over the region (Nesbitt & Zipser, 2003). Parker et al., (2005) observed a strong diurnal cycle of low-level winds during the West African monsoon season using radiosondes and pilot balloons. The intensification of the low-level winds at night was later documented as a nocturnal low-level jet (NLLJ) by Lothon et al., (2008). In this study, the NLLJ is labeled as the Sahel/Sahara low-level jet (SLLJ) because it is located over the Sahel during the pre-monsoon season and the Sahara during the monsoon season. A separate NLLJ was reported by Guedje et al. (2019), who observed a coastal NLLJ over Benin. This coastal NLLJ is important for the northward transport of cold air with high relative humidity and nighttime genesis of extensive stratus cloud (Lohou et al., 2020).

Parker et al. (2005) and Lothon et al. (2008) explain the mechanisms behind the SLLJ as follows. In the daytime, the planetary boundary layer (PBL) is deep and the low-level winds are weak. This condition is associated with weak wind shear because of

the vertical mixing with higher level winds. Overnight, the boundary layer becomes more stratified and turbulence is weaker, allowing winds just above the PBL (around 925 hPa) to strengthen. As the Coriolis force is weak at latitudes near the Gulf of Guinea, the wind acceleration during the night is proportional and parallel to the horizontal pressure gradient force associated with the Saharan heat low. Fiedler et al. (2013) found that the SLLJ is stronger and more frequent from May to July and can impact dust emissions throughout the year.

The differential heating of the ocean and land surface during the day results in strong meridional temperature and density gradients near the Gulf of Guinea coastal zone. The balance between the horizontal advection of cool maritime air inland and turbulence in the PBL over land results is a sea breeze front over the coast in the afternoon (Racz & Smith, 1999). Grams et al. (2010) showed that the sea breeze front has important impacts on the regional heat and moisture budgets. The sea breeze front also acts as a trigger for convective systems to overcome convective inhibition and to develop earlier during the day than in the region farther north (Grams et al., 2010; Spengler et al., 2005). Fink et al., (2010) found substantial rainfall associated with the sea breeze circulation between March and November. Shallow convective showers cross the coastline during morning hours and develop into strong afternoon thunderstorms while propagating inland (Maranan et al., 2018). The propagation of convective systems is also consistent with CloudSat and CALIPSO satellite observations that show the advance of the monsoon flow in the early afternoon (Stein et al., 2011).

Most West African diurnal cycle studies are based on the monsoon season; the diurnal cycle during the pre-monsoon season over the Gulf of Guinea and West Africa in general has been understudied even though it offers interesting dynamical contrasts to the monsoon season. Further, climate models have trouble representing the diurnal cycle, potentially due to the fidelity of their convective parameterizations and relatively coarse temporal and horizontal resolutions (Diro et al., 2012).

The ECMWF Reanalysis 5th Generation (ERA5) is the first reanalysis with a temporal resolution of one hour and a spatial resolution less than 0.5°, so ERA5 is the latest and likely technologically advanced reanalyses to study the West African region. The goal of this study is to characterize the diurnal variation of West African precipitation and low-level winds emanating from the Gulf of Guinea coast during the pre-monsoon in April, May, and June (AMJ) season and farther inland during the monsoon in July, August, and September (JAS) season using ERA5 and precipitation observations from the NASA Tropical Rainfall Measuring Mission (TRMM) and Global Precipitation Measurement (GPM) satellite radars.

## 5.2. Data and Methodology

Hourly data from ERA5 (Hersbach et al., 2020) for 1998 to 2019 were used in this study. ERA5 has 37 vertical pressure levels a horizontal resolution of 32 km. The data was interpolated to 0.5° using bilinear interpolation to optimize data processing. ERA5's high temporal and spatial resolution allows analysis of the diurnal variation of winds over the West African region with higher fidelity than previously available

reanalyses, which are 3-hourly and 0.5° or coarser resolution. The ERA5 variables used in this study were: horizontal and vertical winds, temperature, humidity, and large-scale and convective precipitation. The vertically-integrated moisture flux convergence (MFC) from all the pressure available between 975 to 200 hPa was calculated from Banacos and Schultz (2005): $MFC = -\nabla.(qV_h) = -V_h.\nabla q - q\nabla.V_h$, where q is specific humidity, $V_h$ is horizontal winds, and $\nabla$ is $\hat{\imath}\delta/\delta x + \hat{\jmath}\delta/\delta y$. MFC is a variable highly related to moisture tendency and precipitation rate. Pressures above 975 hPa and not 1000 hPa were considered in order to exclude 1000 hPa values that are under the surface.

The sea breeze and NLLJs were identified using meridional winds and ERA5 convergence at 950 hPa. The vertical structure of ERA5 vertical velocity and meridional flow at different times during the day were analyzed in order to determine the role of the sea breeze and NLLJ near the coast and the SLLJ farther inland on the deep and shallow meridional circulations and associated convection. Hourly TRMM/GPM precipitation observations were considered in this study to complement the ERA5 data since precipitation is one of the less constrained variables in reanalyses.

Observations from the TRMM Precipitation Radar (PR) for 1998 to 2014 and from the GPM Dual-Frequency Precipitation Radar (DPR) for 2014 to 2019 were used. The orbital data was assigned to grids with a horizontal resolution of 0.25° and temporal resolution of an hour. The data was interpolated to 0.5° to be consistent with horizontal resolution of our interpolated ERA5 dataset. The TRMM PR was a single-wavelength ($K_u$) radar that operated at 13.8 GHz. Its minimum detectable reflectivity was 17 (18) dBz and it had a swath width of 240 (215) km before (after) 2001 when the satellite was

boost from 350 to 402.5 km in order to conserve fuel. The GPM DPR consists of a $K_a$-band radar operating at 35.5 GHz and a $K_u$-band radar operating at 13.6 GHz. The swath width is 245 km for the $K_u$-band channel, and 125 km for the $K_a$-band channel. The DPR's minimum detectable reflectivity is approximately 14 dBz. This study uses TRMM 2APR and GPM 2ADPR products (Stocker et al., 2018). TRMM 2APR is the data reprocessed using the newer GPM algorithms and provides surface precipitation that is retrieved using the near-surface reflectivity.

The TRMM/GPM precipitation is categorized as convective, stratiform or shallow in the 2APR and 2ADPR products (NASA/JAXA, 2016). The convective classification refers to regions of deep active convection, where strong vertical air motions dominate, and precipitation particles increase in mass by coalescence and/or riming (Houze, 1989). The stratiform classification represents regions of aging convection, where weaker vertical motions dominate, and precipitation particles increase in mass by vapor deposition above the melting level (i.e. 0°C; Houze, 1997). The convective-stratiform separation algorithm determines whether the echo is convective or stratiform by examining the horizontal variability of the reflectivity (Steiner et al., 1995) and its vertical profile (Awaka et al., 2007). The shallow classification refers to echo tops lower than the climatological 0°C level and is generally considered to form from convective processes in the tropics (Funk et al., 2013; Kodama et al., 2009).

The TRMM and GPM satellites overlapped from April to September 2014 before TRMM began its slow descent. Because the DPR is more sensitive than the PR, observations from both radars during this overlapping period were compared to

determine the impact of sensitivity on the precipitation retrievals. The DPR retrieved 10% more shallow precipitation than the PR during the monsoon season (i.e., JAS). Shallow convection typically has very low rain rates, so the DPR should be able to sense more of the shallow population than the PR because of its higher sensitivity to lighter rain. However, the DPR retrieved 25% less shallow precipitation compared to the PR during the pre-monsoon season (i.e., AMJ) around the coastal area (5°N). DPR (deep) convective precipitation increased over this region, so it is postulated we that because the DPR's increased sensitivity makes it able to sense higher echo tops than the PR, it is more likely to categorize congestus clouds as deep convective rather than shallow. It is worth mentioning that the horizontal structure and diurnal variation of precipitation from the GPM and TRMM radars are consistent, and our main results do not change when the TRMM and GPM datasets are analyzed independently. The difference in sensitivity is balanced by having the additional sampling throughout the diurnal cycle, which takes a long time to achieve because of the precessing orbits of both satellites.

### 5.3. Seasonal mean precipitation and meridional overturning

Figure 5.1 shows the seasonal mean precipitation from the TRMM/GPM radars and seasonal mean vertical motion and meridional flow from ERA5 over West Africa from 1998 to 2019. The pre-monsoon season is represented by AMJ and the monsoon season is represented by JAS. These seasonal definitions better delineate conditions before and after the monsoon, compared to the more traditional MAM/June-August seasonal separation (Fink et al., 2010; Gu & Adler, 2004). Figures 5.1a and b show that

the main band of precipitation is offshore during the pre-monsoon, whereas most of the rain during the monsoon is over land. While a significant amount of rain is still present off the west coast of West Africa during the monsoon season, our study is focused on the southern coast and central portion of West Africa and the meridional patterns therein. As such, the rest of this study will only show latitudinal cross sections between 7°W and 3°E (i.e., the dashed lines in Figs. 5.1a and b). This longitude range was chosen because the precipitation is zonally uniform over this region and the coastline doesn't vary much with latitude, as well as to minimize orographic influences by the higher topography to the west and east. The rain types by latitude (Figs. 5.1c and d) and the cross sections of meridional overturning (Figs. 5.1e and f) indicate two distinct regions during both seasons: a deep, highly convective circulation just south of the coast in AMJ and north of the coast in JAS, and a shallow, weakly precipitating circulation located farther inland.

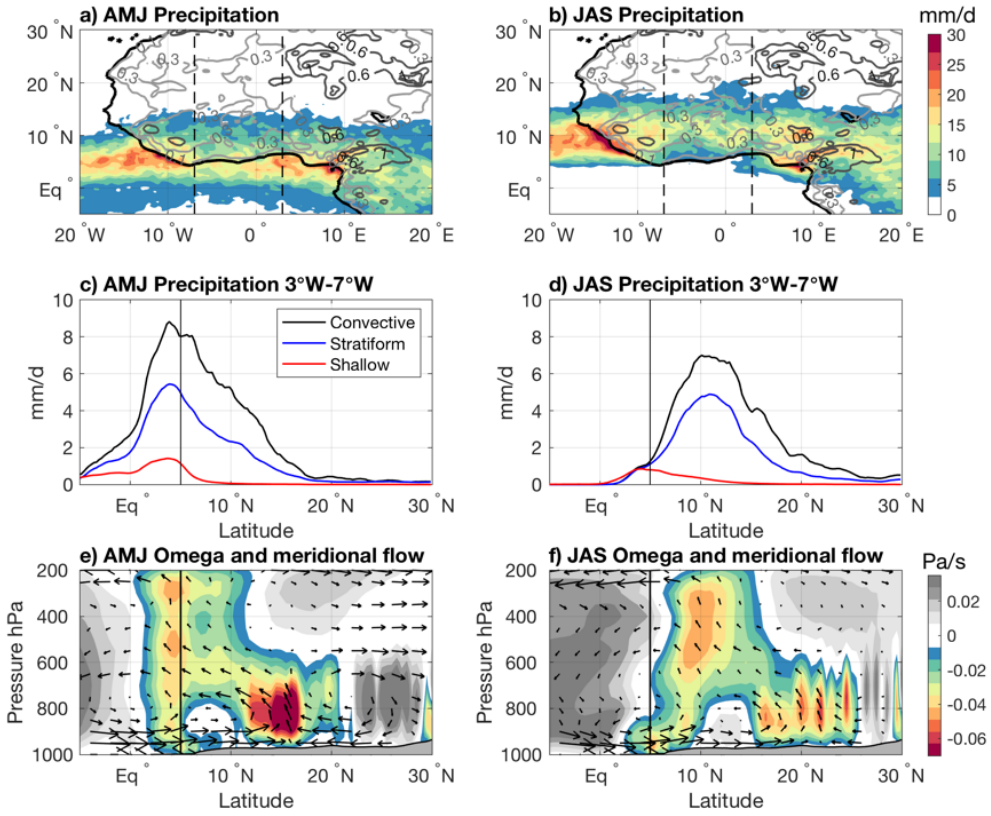


**Figure 5.1 a-b) Total precipitation from the TRMM/GPM radars (shaded, in mm $d^{-1}$) and topography (contours, in km) during AMJ (left panel) and JAS (right panel). c-d) Convective, stratiform and shallow precipitation from TRMM/GPM radars and e-f) omega cross section (shaded, in Pa $s^{-1}$) and meridional flow (arrows) from ERA5 across 7°W – 3°E (dashed lines in top figures) for each season. The vertical meridional flow component has been multiplied by 10 to account for the small ratio of the plot. Largest meridional wind vector is 5 m $s^{-1}$. The solid line at 5.5°N highlights the coastline.**

During AMJ, the pre-monsoon season, deep upward motion linked to the deep meridional overturning is located around 4°N (Fig. 5.1e), with southerly flow at the surface and northerly flow at upper levels at its equatorward flank. Strong precipitation is linked to this deep upward motion (Fig. 5.1a) and convective, stratiform and shallow precipitation explain 55, 35 and 10% of the total precipitation at this latitude, respectively (Fig. 5.1c). Additionally, shallow upward motion is located over the Sahel

around 15°N with the return flow of the overturning circulation penetrating the latitude of deep upward motion at mid-levels (Fig. 5.1e). The dynamical processes of the West African SMC are different than the SMCs in the East Atlantic and East Pacific (Huaman & Schumacher, 2018; Zhang et al., 2008). The ascending motion of the shallow circulation is linked to surface sensible heat fluxes instead of latent heating from convection (Hagos & Zhang, 2010). The West African SMC is also strengthened by the enhanced low-level convergence associated with the SLLJ (Lothon et al., 2008). The West African SMC transports some moisture far inland and moderate amounts of convective and stratiform precipitation are seen in the southern part of the SMC region from 10-15°N (Fig. 5.1c).

During JAS, the monsoon season, the deep upward motion linked to the deep meridional overturning is now located over land, at around 10°N (Fig. 5.1f). This deep circulation is associated with larger amounts of both convective and stratiform precipitation (Fig. 5.1d), although the fraction of rain that is stratiform is larger (40%) than in the pre-monsoon (32%), consistent with Schumacher and Houze (2006). Even though the shallow precipitation is insignificant over the monsoon region (i.e., 4%), it is predominant over the coastal area (Maranan et al., 2018). This shallow precipitation is linked to a very shallow circulation with overturning meridional flow at 800 hPa (Fig. 5.1f). Additionally, the generally dry shallow upward motion linked to the West African SMC is located farther north and over the Sahara (around 20°N) and is less intense but wider compared to the pre-monsoon season. The total shallow upward motion seems to be composed of isolated shallow upward cells between 16° and 26°N, probably forced

by irregularities in the topography over this region (Fig. 5.1b) since air above elevated terrain warms more quickly (Lavaysse et al., 2009).

### 5.4. Diurnal cycle of dynamical fields

The sea breeze and NLLJs play important roles in the diurnal cycle of the West African region. During sea breeze events, the air over land warms during daytime, pressure drops, and air accelerates from sea to land in response. The SLLJ results from the strong meridional temperature and pressure gradients in the Sahel and Sahara regions. Figure 5.2 shows the seasonal cycle of the 950-hPa meridional wind (top panels) and divergence (bottom panels) in shading at different time periods of the day from 7°W – 3°E. Since the sea breeze takes place during the afternoon and NLLJs occur at night, an approximation of the sea breeze (NLLJ) is calculated by removing the daily mean meridional wind and divergence from the 12-18 UTC (20-08 UTC) averages, shown as contours in Fig. 5.2. UTC and local time are indistinguishable in this longitude range. The wind anomalies associated with the sea breeze occur over the coastal region (about 6°N) throughout the year (Fig. 5.2a), and produce anomalies in low-level convergence (i.e. negative values of divergence) from 6-8°N (Fig. 5.2b). The SLLJ is also evident over land throughout the year (Fig. 5.2c). The southerly flow of the SLLJ migrates between 5°N in winter and 20°N in summer and drives strong low-level convergence into the West African SMC (Fig. 5.2d). A second NLLJ is evident from July to September just north of the coast (around 8°N) in the low-level convergence

field. Guedje et al. (2019) identified this second NLLJ and labeled it as the coastal NLLJ.

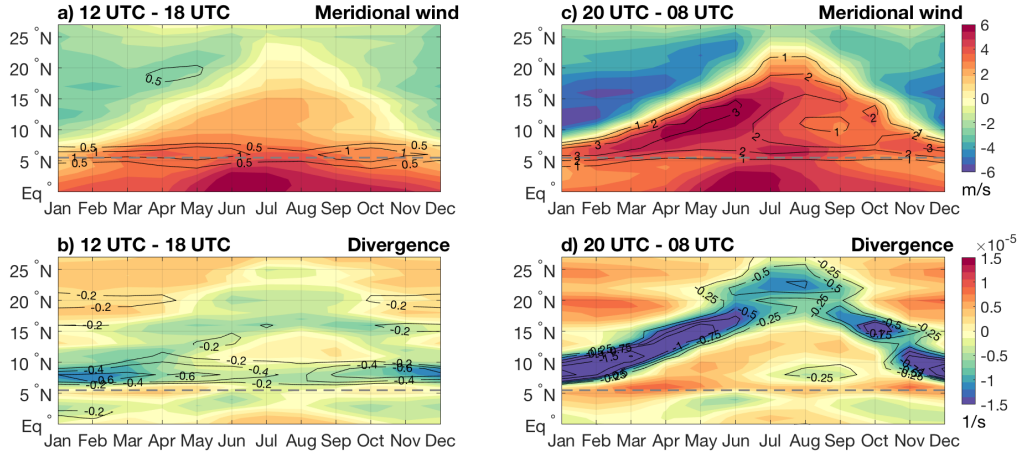


**Figure 5.2 Total meridional wind (shaded) and the sea breeze (12 – 18 UTC, contours) and NLLJ (20 – 08 UTC, contours) anomalies in m $s^{-1}$ at 950 hPa (a and c), convergence (shaded) and sea breeze and NLLJ anomalies (contours) in $s^{-1}$ at 950 hPa (b and d). The dashed line at 5.5°N highlights the coastline.**

Figure 5.3 shows the diurnal cycle of the divergence, vorticity, meridional wind, zonal wind, temperature, and specific humidity at 950 hPa across 7°W – 3°E during the pre-monsoon (AMJ) and monsoon (JAS) seasons. Each of these atmospheric variables exhibit significant diurnal variability that varies by season. During AMJ, low-level convergence over the ocean (4°N) is maximum during the late morning (Fig. 5.3a). At 12 UTC, low-level convergence is observed over the coastal region (6°N) and propagates inland during the early afternoon at about 11 m $s^{-1}$ (Fig. 5.3a), along with increasing southerly flow from the Atlantic (Fig. 5.3c). The convergence phase speed is consistent with Grams et al. (2010), who estimated a sea breeze phase speed of 10 m $s^{-1}$ at the West African coast in boreal summer. Thus, the sea breeze front is the result of the

balance between horizontal advection of cool maritime air and turbulence in the daytime PBL over land. The sea breeze front penetrates inland until 21 UTC. Positive vorticity is seen behind the sea breeze front (Fig. 5.3b), which might enhance shallow precipitation over the coast (Fig. 5.1c), consistent with Maranan et al. (2018).

At night during AMJ, strong southerly flow associated with the SLLJ is present around 10°N (Fig. 5.3c) and drives low-level convergence at 15°N (Fig. 5.3a). Although the sea breeze and SLLJ are linked to southerly flow at similar latitude bands (i.e., between 5° and 10°N), the associated regions of low-level convergence do not interact due to the small scale of the sea breeze and large continental scale of the SLLJ. The sea breeze is seen as a strong low-level convergence propagating into land (i.e., 250 km onshore) from 12 UTC to 18 UTC. At 18 UTC, the maximum low-level convergence is located 15° (i.e., 1000 km onshore) and results from the SLLJ. The SLLJ drives low-level convergence and enhances the West African SMC at 15°N, over the Sahel. This region is also dominated by positive vorticity (Fig. 5.3b) and a large temperature gradient (Fig. 5.3e). However, the low specific humidity over this region inhibits convection (Fig. 5.3f). While the focus of our study is on meridional flow, the diurnal cycle of zonal wind is also observed (Fig. 5.3d). This result is consistent with Parker et al. (2005), who showed increasing zonal winds at night when meridional winds also increase. The maximum westerly and easterly flows around 10° and 20°N, respectively, are linked to the cyclonic circulation over the West African heat low region.

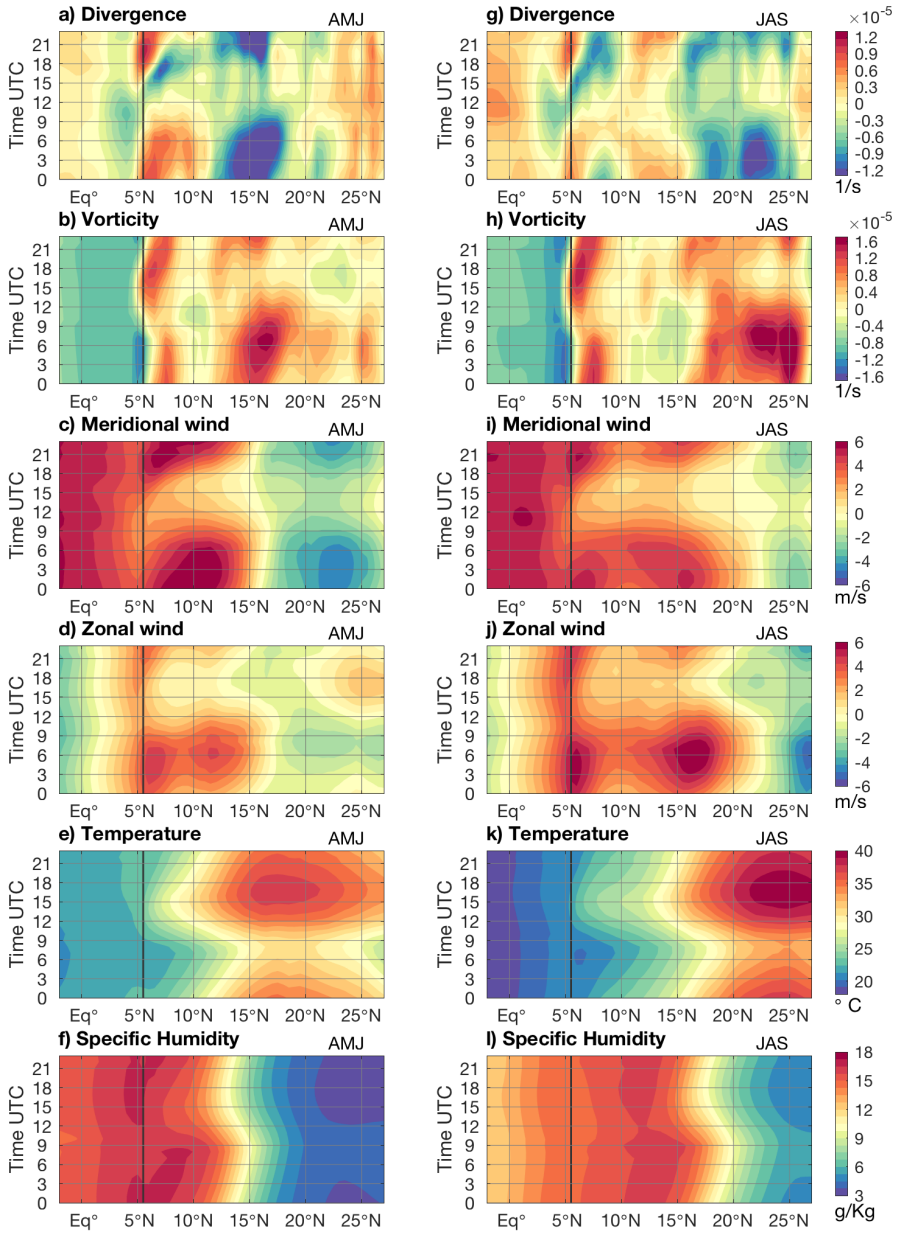


**Figure 5.3 Latitude-time diagram at 950 hPa of divergence (a and g) in $s^{-1}$, vorticity (b and h) in $s^{-1}$, meridional wind (c and i) in m $s^{-1}$, zonal wind (d and j) in m $s^{-1}$, temperature (e and k) in °C, and specific humidity (f and l) in g $kg^{-1}$ across 7°W-3°E during AMJ (left) and JAS (right). The solid line at 5.5°N highlights the coastline.**

Similar to AMJ, the oceanic low-level convergence during JAS is maximum between 6 to 15 UTC (Fig. 5.3g) and begins to propagate onshore around 12 UTC in association with increasing southerly flow from the Atlantic (Fig. 5.3i). However, the sea breeze convergence signature only propagates onshore until 18 UTC. After 18 UTC, a non-propagating low-level convergence feature associated with the coastal NLLJ is observed around 8°N until 06 UTC, consistent with Guedje et al. (2019). Behind the sea breeze and coastal NLLJ regions, strong positive vorticity occurs (Fig. 5.3h) that enhances shallow precipitation in the coastal region (Fig. 5.1d). The SLLJ is observed around 16°N (Fig. 5.3i) and drives strong low-level convergence around 21°N (Fig. 5.3g). The SLLJ in JAS is less intense compared to the pre-monsoon season (cf. Figs. 5.3c and i) because of the weaker southerly Atlantic inflow at this higher latitude. The coastal NLLJ does not interact with the SLLJ, which is located hundreds of km farther north. Although the SLLJ region shows positive vorticity (Fig. 5.3h), precipitation is inhibited due to the dry conditions (Fig. 5.3l) and strong temperature gradient (Fig. 5.3k) that drives a strong gradient of sensible heating but latent heating is muted. The diurnal cycle of the zonal wind is also strong during the monsoon season (Fig. 5.3j).

During the pre-monsoon season, the sea breeze front and SLLJ are important features in the diurnal variation of the West African upward motion and convection. During the monsoon season, besides the sea breeze front and SLLJ, a coastal NLLJ forces low-level convergence and is involved in low-level stratus cloud formation over the Gulf of Guinea coast at night (Fig. 5.3g; Lohou et al. 2020). These features can interact with and modify the deep convection and associated meridional circulation over

West Africa during the pre-monsoon and monsoon seasons. The modification of the meridional circulation and convection is expected to be different during these two seasons due to the shift of the convection from the coast to farther inland.

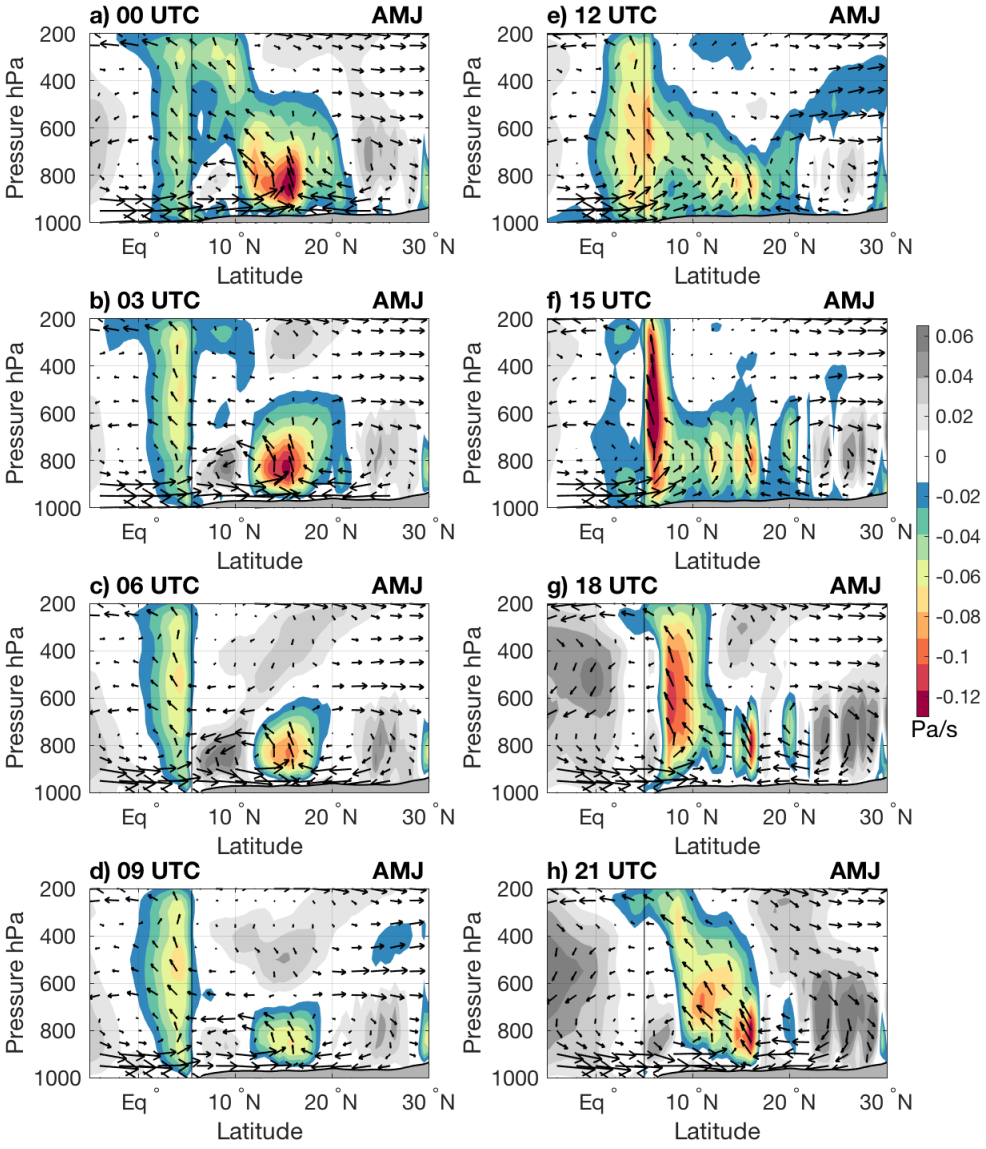


**Figure 5.4 Diurnal variation of vertical motion (Pa $s^{-1}$) and meridional flow cross sections across 7°W-3°E during AMJ. The vertical meridional flow component has been multiplied by 10 to account for the small ratio of the plot. Largest meridional wind vector is 5 m $s^{-1}$. The solid line at 5.5°N highlights the coastline.**

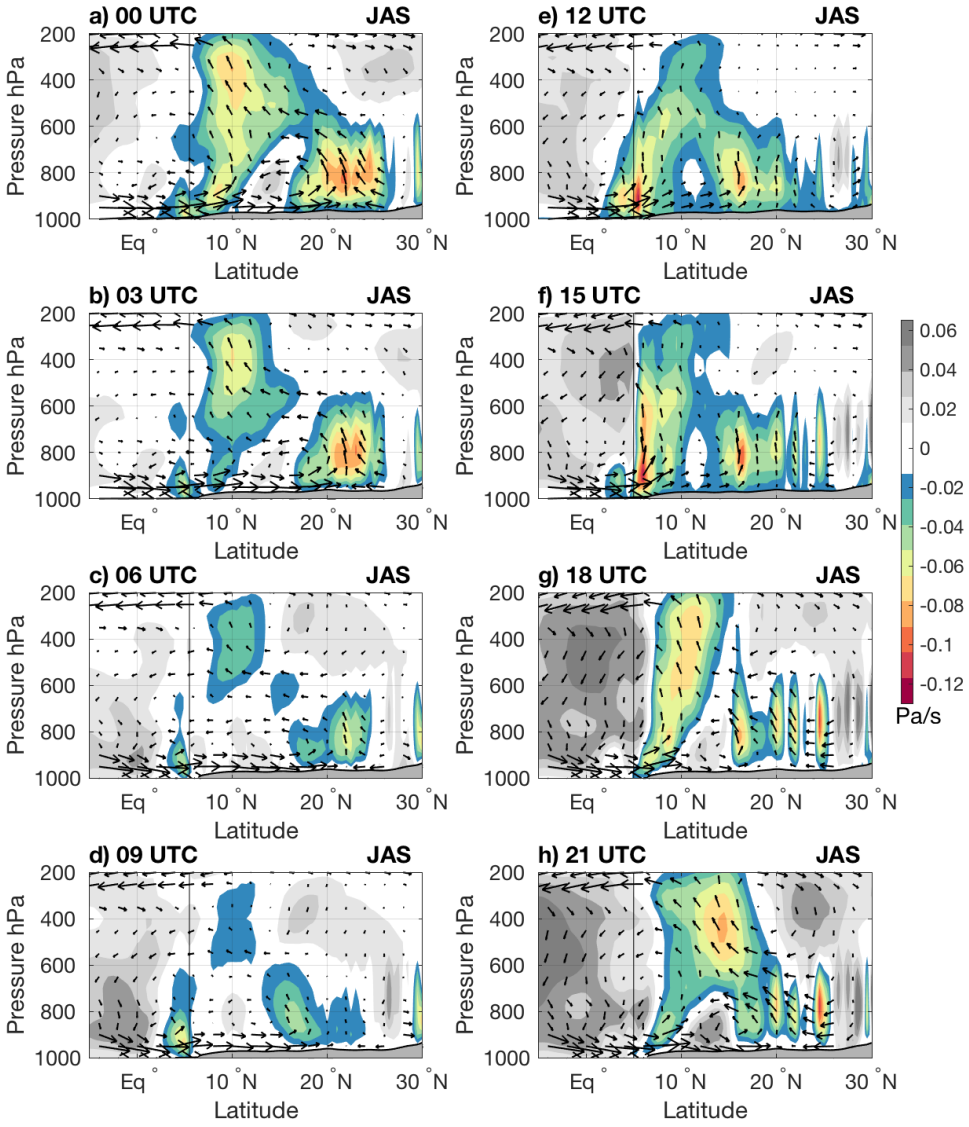


**Figure 5.5 Same as fig. 5.5 but for JAS.**

Figures 5.4 and 5.5 show the diurnal variation in the vertical structure of the vertical velocity and meridional flow during the pre-monsoon (AMJ) and monsoon (JAS) seasons, respectively. During AMJ at 00 UTC (Fig. 5.4a), the shallow upward motion associated with the West African SMC is located at 15°N. The strong upward motion and shallow circulation are driven by the strong SLLJ, which induces low-level

convergence at night (Fig. 5.3a). Deep upward motion associated with the deep meridional circulation is seen over the ocean around 4°N. Between these two cells, there is a subsidence region centered at 10°N. The low-level subsidence may be associated with the stability of the PBL during nighttime and the shrinking of both planetary and relative vorticity in order to conserve the potential vorticity over this region (Vizy & Cook, 2002). At low levels, the column of air moves from a positive relative vorticity at 16°N to a less positive relative vorticity at 11°N. A similar vertical structure is seen at 03, 06, and 09 UTC (Figs. 5.4b-d), but with the shallow upward motion weakening inland, the deep upward motion intensifying over the Gulf of Guinea, and the subsidence between the two cells strongest at 06 UTC. The shallow upward motion over the Sahel is weakest at 09 UTC due to the weakening low-level convergence associated with the SLLJ after sunrise.

As daytime sensible heating warms the lower atmosphere, mixing within the PBL increases, moist air interacts with the dry near-surface air, and turbulence diffusion is generated. At 12 UTC (Fig. 5.4e), the PBL is well mixed and the subsidence at 10°N disappears. The balance between horizontal advection of cool maritime air and turbulence in the PBL over land results in a sea breeze front over land (Fig. 5.3a). The deep upward motion starts to shift from the water to north over the coastal region around 6°N with the advancing sea breeze front. At 15 UTC (Fig. 5.4f), the sea breeze front penetrates farther inland, triggering convective systems with deep and strong upward motion at 7.5°N. At 18 UTC (Fig. 5.4g), the deep upward motion has propagated to 9°N and becomes entwined with the southern edge of the West African SMC by 21 UTC

(Fig. 5.4h). After the passage of the sea breeze front, advection of cool, maritime air with strong stable stratification is evident until the morning hours and the subsidence at 10°N and SLLJ are restored (Figs. 5.3c; 5.4a-c).

During JAS (Fig. 5.5), deep upward motion and the associated precipitation (Fig. 5.1b) is located exclusively over land, making the diurnal variation of the vertical structure of the upward motion and meridional flow over the West African region (7°E – 3°E) different compared to the pre-monsoon season. At 00 UTC (Fig. 5.5a), the shallow upward motion associated with the low-level convergence driven by the SLLJ is located around 22°N, farther north and less intense compared to the pre-monsoon season due the weaker southerly Atlantic inflow at higher latitudes. The coastal NLLJ occurs near 8°N and also enhances shallow ascending vertical motion and probably low-level stratus clouds due to the strong low-level convergence and stratification of the boundary layer. Lohou et al. (2020) and Van der Linden et al. (2015) observed non-precipitating, low-level clouds in the coastal NLLJ region during nighttime. Deep upward motion is located at 10°N. The deep and shallow upward motion combined suggest a tilted monsoonal structure with shallow convection around 7°N, deep convection (i.e., ascending motion throughout the troposphere) around 9°N, and stratiform rain (i.e., ascending motion at upper levels and descending motion at lower levels) around 12°N. The low-level descending motion at 15°N is linked to the subsidence region between the deep monsoon and shallow Saharan cells also seen during the pre-monsoon season during nighttime due to weak wind shear and a stratified PBL. Between 03-09 UTC (Figs. 5.5b-d), the shallow upward motion and low-level convergence associated with the coastal NLLJ and SLLJ at

8° and 20°N, respectively, weaken. It is interesting to see oceanic shallow upward motion around 4°N related to stratus clouds typically located over the southeastern Atlantic during the early morning hours (Warren & Hahn, 2002). The deep upward motion around 10°N also weakens, while some upper-level upward motion persists through 9 UTC.

At 12 UTC (Fig. 5.5e), shallow upward motion is observed over the coast, around 6°N. The sea breeze front seems to force shallow upward motion onshore, instead of deep upward motion as seen during the pre-monsoon season (Fig. 5.4e). The subsidence region at 10°N minimizes as the result of the air mixing in the PBL due to daytime sensible heating. At 15 UTC (Fig. 5.5f), the shallow upward motion over the coast intensifies on the land side of the coast and the monsoon upward motion at 9°N starts developing. At 18 UTC (Fig. 5.5g), monsoon deep convection is tilted with shallow upward motion around 7°N and deep upward motion around 10°N. There is much less inland propagation of deep convection associated with the sea breeze than observed during the pre-monsoon. Isolated shallow upward motion cells have developed over the Saharan region between 16° and 26°N and might be the result of the large daytime sensible heating and irregular topography over this region (Fig. 5.1f). At 21 UTC (Fig. 5.5h), the monsoonal deep upward motion is located at 15°N, subsuming the southern part of the shallow cell around 18°N. The low-level subsidence at 15°N is restored. Over the oceanic and coastal area, the descending motion of the deep circulation associated with the monsoon convection seems to inhibit any shallow upward motion during 18 and 21 UTC.

## 5.5. Diurnal cycle of precipitation

The previous section showed that the diurnal variation of the vertical upward motion is in part forced by the sea breeze front, SLLJ, and coastal NLLJ. The propagation of upward motion is triggered by the sea breeze front during the afternoon, and the SLLJ and coastal NLLJ force low-level convergence over the West African SMC and Gulf of Guinea coast, respectively. The precipitation associated with the sea breeze propagation and NLLJs by season using ERA5 and TRMM/GPM data was next analyzed.

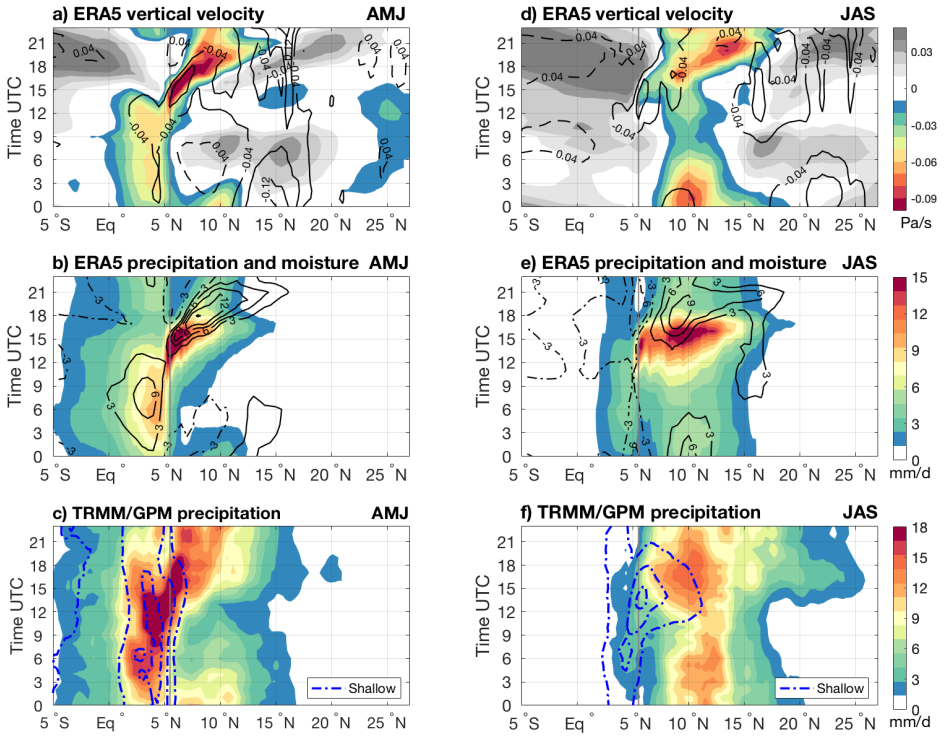


**Figure 5.6 Latitude-time diagram of vertical velocity at 400 hPa (shaded) and 850 hPa (contours) in Pa $s^{-1}$ (a and d), precipitation (shaded) and MFC (contours) in mm $d^{-1}$ from ERA5 (b and e), and convective (shaded), stratiform (black contours each 1 mm $d^{-1}$ starting at 2 mm $d^{-1}$), and shallow (blue contours each 0.5 mm $d^{-1}$ starting at 0.5 mm $d^{-1}$) precipitation in mm $d^{-1}$ from TRMM-GPM (c and f) during AMJ (left) and JAS (right). The solid gray line at 5.5°N highlights the coastline.**

Figure 5.6 shows latitude-time diagrams of the 850-hPa and 400-hPa vertical velocity from ERA5, MFC (defined in Section 2) and precipitation from ERA5, and precipitation from the TRMM/GPM radars across 7°W – 3°E during the pre-monsoon and monsoon season. During AMJ, the 850-hPa vertical velocity (Fig. 5.6a, contours) is similar to the near-surface convergence in Fig. 5.3a and shows the diurnal evolution of the shallow upward motion near 15°N forced by the SLLJ during nighttime. Very little precipitation is associated with this feature in either the ERA5 (Fig. 5.6b, shaded) or TRMM/GPM (Fig. 5.6c) datasets. Over the ocean (4°N), moderate upward motion occurs throughout the troposphere (i.e., 850 and 400 hPa) at night and into the late morning and is associated with moderate rain amounts in ERA5 and strong rain amounts based on TRMM/GPM observations. Shallow convective rain observed by the spaceborne radars also maximizes in this region and time of day.

Over the coast during AMJ, strong upward motion (Fig. 5.6a) is seen throughout the troposphere at 12 UTC and propagates with a phase speed around 11 m $s^{-1}$ onto land during the afternoon following the sea breeze front. The propagating upward motion is associated with strong ERA5 precipitation near the coast between 12 to 18 UTC (Fig. 5.6b), consistent with TRMM/GPM observations (Fig. 5.6c). However, ERA5 shows low precipitation (5 mm $d^{-1}$) after 18 UTC between 6-12°N, while TRMM/GPM observes moderate precipitation (12 mm $d^{-1}$) into the early morning. The ERA5 MFC (shown as contours in Fig. 5.6b) and precipitation maxima are collocated over the ocean, but the maximum MFC between 8-10°N occurs during the early evening when ERA5 precipitation is less intense. Therefore, despite the fact that ERA5 captures the sea

breeze front and its coupling to moisture, it fails to produce deep upward motion with strong precipitation between 18 to 00 UTC over land and instead is retrieving shallower structures with less intense precipitation but large MFC.

During JAS, ERA5 indicates shallow upward motion over the Sahara (Fig. 5.6d) with a nocturnal maximum around 22°N and additional regions of daytime shallow upward motion poleward of 15°N resulting from turbulence in the PBL. ERA5 produces very little precipitation poleward of 15°N (Fig. 5.6e), whereas TRMM/GPM indicates light to moderate daytime rain at these latitudes (Fig. 5.6f). This disparity suggests that the ERA5 convective parameterization needs to be more responsive to shallow large-scale forcing, in this case the production of large eddies in the PBL resulting from strong daytime heating that can overcome environmental convective inhibition and produce deep convective cells. On the other hand, ERA5 produces larger rain amounts over the Gulf of Guinea compared to TRMM/GPM, despite the general absence of large-scale upward motion.

Over the coast during JAS, the sea breeze forces shallow upward motion (Fig. 5.6d) and shallow precipitation (Fig. 5.6f) during the early afternoon that then transitions into deeper upward motion and convection. The coastal NLLJ, which occurs around 8°N between 18 to 03 UTC (Figs. 5.2 and 5.3g), forces very shallow upward motion and is not linked to significant precipitation in the ERA5 (Fig. 5.6e) or TRMM/GPM (Fig. 5.6f) datasets. Therefore, low-level stratus clouds are suggested over this region. MFC is also enhanced just to the north of the coastal NLLJ (Fig. 5.6e). The 400-hPa vertical velocity (Fig. 5.6d) indicates deep upward motion from 10° to 15°N between 15 and 6 UTC

associated with the African monsoon, which appears to be independent from the sea breeze front. Although ERA5 and TRMM/GPM both show inland precipitation propagation near the coast associated with the sea breeze, the precipitation datasets are inconsistent in the African monsoon region (around 10°N). ERA5 shows large precipitation amounts (> 15 mm $d^{-1}$) between 15 to 18 UTC with a significant decrease in precipitation after 18 UTC, while TRMM/GPM observes moderate precipitation (7-10 mm $d^{-1}$) from the afternoon into the morning hours. ERA5 MFC (Fig. 5.6e) shows a similar diurnal variation compared to TRMM/GPM precipitation in the African monsoon region, but the ERA5 precipitation does not respond to the MFC and large-scale vertical motion fields over land during the evening hours (similar to what occurs during AMJ). The early and overly intense onset of precipitation over land during the day is also a persistent problem in most climate models (Dai, 2006; Fiedler et al., 2020; Kniffka et al., 2019).

To further explore the diurnal precipitation differences between ERA5 and TRMM/GPM, different types of precipitation from both datasets were compares. ERA5 provides convective and large-scale precipitation, which depend on the convective and cloud microphysical schemes, respectively (Haerter & Berg, 2009). Convective precipitation is generated by the convection scheme, which represents convection at spatial scales smaller than the grid box. The cloud microphysical scheme represents the formation and dissipation of clouds and large-scale precipitation due to changes in atmospheric quantities (such as pressure, temperature and moisture) at spatial scales of the grid box. The convection scheme operates first and can affect the production of

large-scale rain by moistening the grid if convection occurs during the time step. Otherwise, the large-scale microphysics is responsible for any rain production.

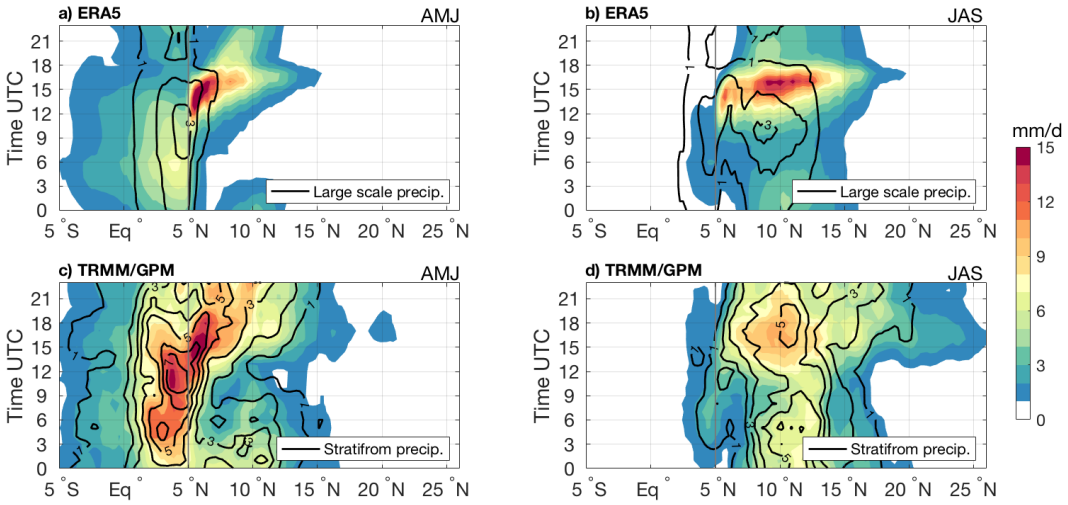


**Figure 5.7 Latitude-time diagram of a-b) convective (shaded) and large scale (contours) precipitation from ERA, and c-d) convective plus shallow (shaded) and stratiform (contours) precipitation from TRMM/GPM across 7°W-3°E during AMJ. Precipitation in mm $d^{-1}$. The solid gray line at 5.5°N highlights the coastline.**

The TRMM and GPM radars provide convective, stratiform, and shallow precipitation that has been classified according to the vertical profile and intensity of the footprint-scale reflectivity (further described in Section 2). While ERA5 convective precipitation should be generally equivalent to the TRMM/GPM convective precipitation, ERA5 large-scale precipitation is not a physical equivalent of radar-based stratiform precipitation. Stratiform rain represents aged convection in the tropics (Houze, 1989, 1997); however, ERA5 diagnoses large-scale rain directly from grid-scale variables rather than via sub-grid-scale convection. Regardless, comparing the precipitation types from both datasets is helpful in determining where and when the

reanalysis rainfall (which is heavily model based) diverges most from the radar-observed rainfall over West Africa.

Figure 5.7 shows latitude-time plots of the convective and large-scale/stratiform precipitation from ERA5 and TRMM/GPM during the pre-monsoon and monsoon seasons. As already discussed, ERA5 underestimates precipitation over the Gulf of Guinea (2-5°N) during AMJ compared to TRMM/GPM (Figs. 5.6b and c). Figures 5.7a and c demonstrate that this underestimate occurs in both the convective and large-scale rain fields. While the underestimation originates with the underproduction of rain by the convective parameterization, the large-scale microphysics are not sufficient to overcome this underproduction. ERA5 and TRMM/GPM show better agreement in the convective rain associated with the sea breeze front. The most intense convective precipitation is observed near the coast (i.e., within 200 km onshore) and both datasets are consistent in daytime propagation and intensity. However, ERA5 underestimates convective rain by about 20% during nighttime over land. The large-scale/stratiform precipitation from ERA5 and TRMM/GPM differ more strongly over land with almost no large-scale rain being produced by ERA5, while TRMM/GPM indicates that about a third of the rain is stratiform. Therefore, the ERA5 total precipitation biases during the pre-monsoon season are associated with the inability of the convective parameterization and large-scale microphysics scheme to represent mesoscale convective system life cycles and stratiform rain processes (e.g., Dai, 2006; Schumacher & Houze, 2003) especially at night.

During JAS, ERA5 overestimates land rainfall during the day and underestimates it at night compared to TRMM/GPM (Figs. 5.6e and f). Figures 5.7b and d illustrates that, once again, the daytime convective precipitation signatures match reasonably well between the two data sets, this time over the broader monsoon rain band, although ERA5 15-18 UTC convective rain is overly intense and there continues to be less agreement in convective rain at night. In addition, the difference between the ERA5 large-scale rain and the TRMM/GPM stratiform rain remains stark. While ERA5 produces large-scale precipitation over land during the monsoon season (unlike during the pre-monsoon season), large-scale rain rates are low and maximize from 09-12 UTC in contrast to the TRMM/GPM observations that show stratiform rain rates at a minimum at 09 UTC and largest at 18 and 03-06 UTC. The TRMM/GPM stratiform precipitation is also coincident with or slightly lags the convective precipitation, consistent with the concept of stratiform rain forming from regions active convection, whereas the ERA5 large-scale rain appears to form in isolation, separate from any convective rain signal. Therefore, the ERA5 total precipitation biases during the monsoon season also result from inaccuracies in both the convective and microphysical scheme performances and their inability to represent long-lived, organized convective systems.

### 5.6. Synthesis of sea breeze and NLLJ impacts over West Africa

The purpose of this section is to synthesize the impacts of the sea breeze, SLLJ and coastal NLLJ on West African convection and meridional overturning before and during the active monsoon season. Figure 5.8 shows a schematic of the diurnal cycle of

meridional flow, upward motion and convection motivated by both the ERA5 dynamical fields and TRMM/GPM radar precipitation analyzed in the previous sections. Note that the convective structures and rainfall are based mainly on TRMM/GPM when disagreement exists between TRMM/GPM and ERA5, especially during the monsoon season (cf. Figs. 5.6e and f).

During AMJ, a combination of shallow convective, deep convective, and stratiform rain is located over the ocean at 09 UTC associated with both shallow and deep overturning (Fig. 5.8a). A region of non-precipitating shallow upward motion is present at 15°N and is related to the low-level convergence driven by the temperature gradient in the Sahara region. Low-level subsidence is seen around 10°N between the deep and shallow overturning cells. At 12 UTC (Fig. 5.8b), a southerly, maritime flow (indicated by the blue arrow) associated with the sea breeze front propagates onto land; the resulting convection is deep and produces strong precipitation. While the deep convection propagates onto land, the weakly precipitating shallow convection stays over the ocean and eventually dies off. Additionally, mixing in the PBL due to sensible heating during the day (yellow arrow) inhibits the subsidence between the deep and shallow overturning cells. From 15 to 18 UTC (Fig. 5.8c), the deep precipitating convection propagates farther inland, forced by the sea breeze front and assisted by the turbulence associated with the daytime mixing in the PBL. Precipitation is maximum at this time and is composed of both convective and stratiform components.

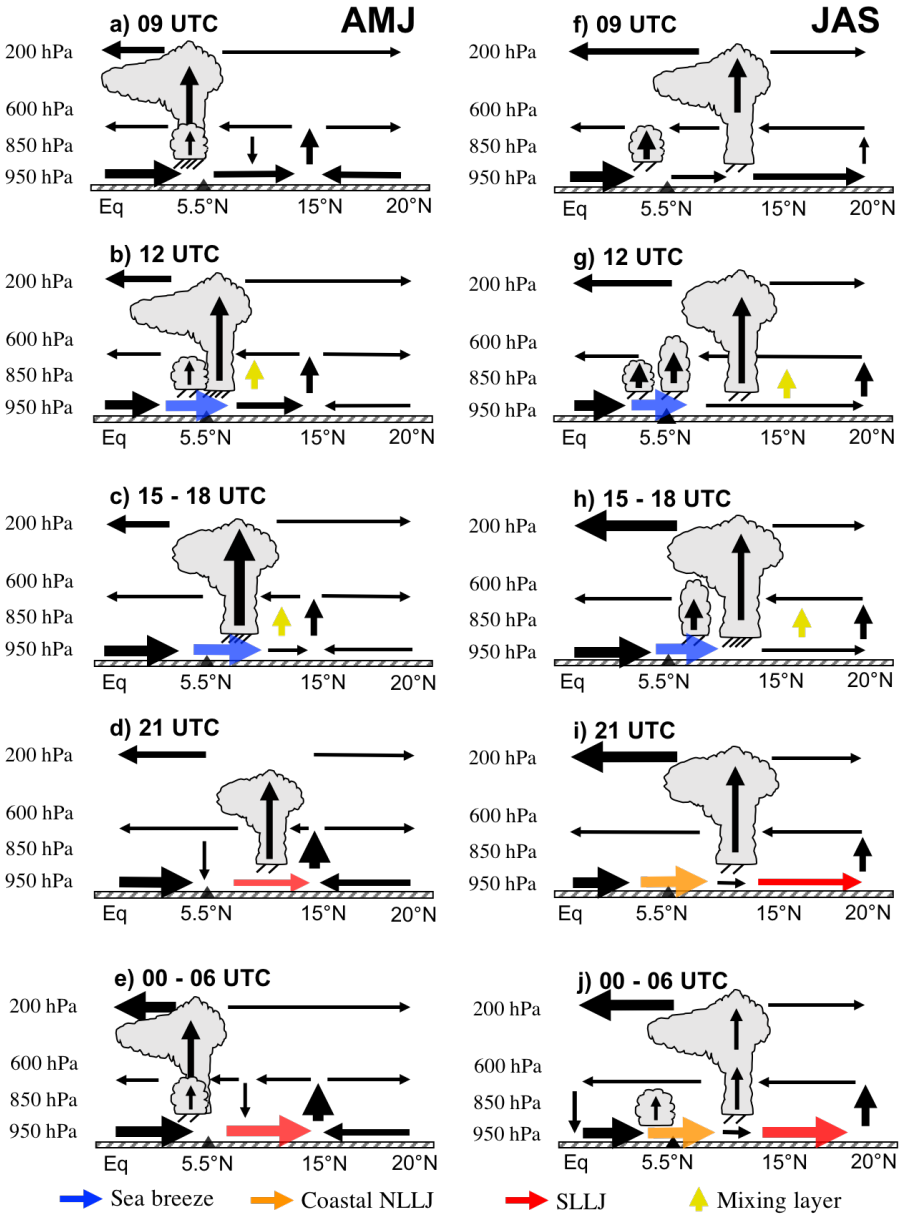


**Figure 5.8 Schematic of the diurnal variation of West African meridional overturning and convection during the pre-monsoon (left) and monsoon (right) season. The triangle indicates the location of the coastline. The thin, thick, and thickest horizontal (vertical) vectors indicate meridional winds (upward motion) smaller than 2 m $s^{-1}$ (-0.05 Pa $s^{-1}$), between 2 and 4 m $s^{-1}$ (-0.05 and -0.1 Pa $s^{-1}$), and larger than 4 m $s^{-1}$ (-0.1 Pa $s^{-1}$), respectively. Two (four) dashes under the convective cloud indicate precipitation smaller (larger) than 18 mm $d^{-1}$ during the pre-monsoon season and smaller (larger) than 13 mm $d^{-1}$ during the monsoon season.**

By 21 UTC (Fig. 5.8d), the AMJ convection becomes less deep as it propagates farther inland. The convection also appears to be interacting with the southern part of the West African SMC. The SLLJ (indicated by the red arrow) develops during this time and strengthens the shallow upward motion over the Sahara due to strong low-level convergence with the synoptic-scale northerlies. Between 00 and 06 UTC (Fig. 5.8e), the convection over land has died out completely and new convection forms over the ocean. The mixing layer over the PBL has vanished and shallow descending motion reemerges between the shallow and deep cells around 10°N. The SLLJ has fully developed and strengthens the dry West African SMC.

During JAS, a different diurnal cycle in low-level wind features, meridional overturning, and convection is seen. At 09 UTC (Fig. 5.8f), shallow precipitating convection is present over the ocean and dry shallow upward motion associated with the Saharan heat low occurs at 20°N. A mix of deep convective and stratiform rain is present around 12°N, but the predominance of the stratiform rain (more likely to occur in the decaying phase of large convective systems) causes the large-scale vertical velocity to have upward motion at upper levels and downward motion below the 0°C level (which occurs at about 550 hPa). At 12 UTC (Fig. 5.8g), newly developing precipitating convection associated with daytime heating over land is located near 10°N and is independent from the shallower convection in the coastal region forced by the sea breeze front. From 15 to 18 UTC (Fig. 5.8h), the inland convection continues to deepen and precipitation increases, while the shallow convection from the coast reaches its greatest inland extent.

At 21 UTC (Fig. 5.8i), deep convection associated with the active monsoon is still vigorous but the shallow convection associated with the sea breeze front has vanished. Two strong southerly flows are seen over land and are linked to the coastal NLLJ and SLLJ. The coastal NLLJ (orange arrow) is important for the northward transport of moisture. Between 00 and 06 UTC (Fig. 5.11j), the deep convection decays and precipitating mid-level clouds are observed, consistent with CloudSat data (Stein et al., 2011). Low-level stratus clouds are observed at night (Lohou et al., 2020) and are related to the coastal NLLJ. The SLLJ and associated low-level convergence has intensified the shallow upward motion associated with the West African SMC.

**5.7. Summary**

ERA5 reanalysis and TRMM and GPM satellite radar data from 1998-2019 were used to provide new insights on the diurnal variation of the West African meridional overturning and convection during the pre-monsoon (AMJ) and monsoon (JAS) seasons. ERA5 dynamical fields showed evidence of a sea breeze front and LLJs in the afternoon and nighttime, respectively, consistent with previous observational studies (Guedje et al., 2019; Lothon et al., 2008). The sea breeze front forces low-level convergence that triggers convective systems and assists in their propagation from the coast inland. Two NLLJs were detected: the coastal NLLJ and SLLJ. The coastal NLLJ is only evident during the monsoon season and provides a source of inland moisture, while the SLLJ forces low-level convergence over the Saharan heat low enhancing the dry SMC throughout the year.

During the pre-monsoon season, when the zonal precipitation band is located over the Gulf of Guinea, a sea breeze front initiates intense precipitation over the coastal region and propagates convective systems onshore during the early afternoon. The sea breeze front penetrates farther inland once turbulence in the PBL dies down in the evening. The SLLJ drives strong low-level convergence into the West African heat low, around 15°N, and the associated dry shallow upward motion intensifies during nighttime when the PBL is stratified and wind shear is weak. During the monsoon season, when the zonal precipitation band is located inland at 10°N, the sea breeze front is linked to shallow convective systems and seems to not interact with the main West African monsoon convection located farther inland. At night, the coastal NLLJ replaces the sea breeze feature and the SLLJ forces low-level convergence into the dry Saharan shallow upward motion at around 22°N.

TRMM/GPM and ERA5 precipitation was also compared. ERA5 has a small precipitation bias over the coastal region where the sea breeze front plays an important role in triggering convection during the early afternoon. However, ERA5 strongly underestimates precipitation over the Gulf of Guinea during the pre-monsoon and farther inland during the monsoon, when each region is experiencing large rain amounts. This underestimation occurs in both the convective and large-scale rain fields so fixing the underestimation would require assessing the convective parameterization, the large-scale microphysics, and their interaction. Although ERA5 shows biases in the diurnal cycle of precipitation, it is able to capture many of the dynamical features associated with the diurnal low-level circulation features over West Africa, like the sea breeze and NLLJs.

Sensitivity tests (not shown) indicate that ERA5 performs better than other reanalyses in capturing these features. Therefore, ERA5 was considered to be an appropriate reanalysis to study the diurnal variation of the West African meridional overturning, but its precipitation should be complemented by observational sources due to limitations in the ERA5 convective and microphysical schemes in simulating mesoscale organized convection.

# CHAPTER VI

# CONCLUSIONS

The large-scale overturning circulation of the tropical atmosphere is complex. On the largest scale, there is the DMC in the Hadley Cell with a maximum in vertical motion around 400 hPa that is typically averaged over seasonal or longer time scales. Additionally, Trenberth et al. (2000) identified a SMC centered near 800 hPa that contributes on the order of 20% of the variance of the global monsoon, with higher contributions over regions such as the East Pacific and West African ITCZs. A number of studies have since analyzed the prevalence and importance of these SMCs, but significant disagreement still exists between datasets. This research aimed to understand the interaction of these large-scale circulations with convective systems in the East Pacific and West Africa.

## 6.1. East Pacific

In the East Pacific, while the DMC is related to the Hadley Cell, the SMC circulation is driven by the meridional SST gradient that produces low-level convergence and latent heating from shallow convection. Organized cloud systems propagate eastward (e.g., Kelvin waves) or westward (e.g., easterly waves) at synoptic scales (i.e., between 2 to 20 days) and can interact with the SMC and DMC seen in the East Pacific ITCZ. In this dissertation, the interaction between synoptic propagating disturbances and the large-scale circulation was studied during different seasons, I found

that these disturbances have different impacts in the SMC and DMC observed in the East Pacific ITCZ.

During boreal winter, convective disturbances that propagate eastward at 10 m $s^{-1}$ along 15°N, many degrees north of the climatological ITCZ, within the central and East Pacific were documented for the first time in this dissertation. These eastward disturbances exhibit high cloudiness associated with upper-level divergence on the east side of NH Rossby waves propagating into the tropics. NH Rossby waves inject positive potential vorticity into the tropics that can initiate and modulate slower-moving, eastward propagating modes. These eastward disturbances impact the large-scale circulation in the East Pacific to a certain extent. The upper-level outflow of the eastward disturbances strengthens the DMC in the northern portion of the East Pacific ITCZ, but the SMC observed in the southern part of the ITCZ and below 700 hPa is not significantly impacted by these eastward propagating disturbances. The SMC is the result of the strong meridional SST gradient, which is strong during boreal winter due to presence of the East Pacific cold tongue.

During boreal spring, Kelvin waves initiate in the west Pacific and propagate eastward at 15 m $s^{-1}$ along the ITCZ axis. As Kelvin waves reach the central and East Pacific, they may interact with NH extratropical Rossby waves, which propagate eastward at 10 m $s^{-1}$. The intrusion of high potential vorticity air associated with NH extratropical Rossby waves into low latitudes excites upper-level divergence in the Kelvin wave, which strengthens the Kelvin wave convection and DMC within the ITCZ.

Additionally, shallow convection ahead of the Kelvin wave appears to enhance the SMC in the southern part of the ITCZ.

OTREC 2019 field campaign observations were crucial to characterize the synoptic variability of the East Pacific ITCZ during boreal summer and fall. Easterly waves are the most predominant synoptic events during these seasons, and this dissertation documented the interaction between easterly waves and the large-scale circulation in the East Pacific for the first time. I identified three strong easterly waves during the OTREC field campaign that strongly modulated the DMC and SMC seen in the East Pacific ITCZ. The trough of the easterly wave was associated with enhanced deep convection and DMC within the ITCZ (i.e., 8°N) and the SMC was displaced north of 6°N. This alteration is associated with the export of column-integrated moisture and MSE by vertical advection. The subsequent convectively suppressed, anticyclonic part of the easterly wave enhanced the SMC at 850 hPa. Positive values of moisture and MSE fields supported by horizontal advection in the easterly wave ridge likely enhanced shallow convection at 4°N. The strong SMC was coupled with an easterly wave anticyclonic structure that drove strong northerly winds between 700 and 800 hPa.

Additionally, due to the strong disagreement of vertical velocity between reanalyses and satellite products in the East Pacific ITCZ documented in previous studies, I assessed the vertical velocity in the East Pacific using the OTREC 2019 field campaign dataset, latent heating retrievals from the GPM satellite, which hosts the newest NASA precipitation radar, and vertical velocity fields from modern reanalyses. The OTREC observations were crucial to identify deficiencies in the reanalyses and

GPM algorithms. Vertical motion retrievals from the OTREC dropsondes indicated shallow ascending motion and an SMC from 3-7°N, over a strong meridional gradient in SST, and deep ascending and a DMC further north, where the SST is warmest. However, all the reanalyses showed a predominant SMC from 3-10°N across the East Pacific ITCZ unless they assimilated the dropsondes, then a weak DMC was found around 8°N. The reanalyses represent a range of resolutions, convective parameterizations, and assimilation schemes so it is unclear why they all have difficulty deepening convection over the EP ITCZ. Vertical motion derived from the GPM latent heating algorithms indicated deep vertical motions associated with a DMC from 3-10°N. The lack of shallow vertical motion is due to the inability of the GPM radar to sense weakly precipitating shallow convection, but the addition of cloud radar data can ameliorate the issue. This dissertation highlights that reanalysis and GPM algorithms, independently, are not able to fully describe the vertical structure of the circulation and associated convection across the EP ITCZ. Both GPM algorithms and reanalysis schemes, especially the convective scheme, need to be revised to accurately capture the vertical structure of the East Pacific ITCZ better.

### 6.2. West Africa

Over West Africa, there is a DMC related to monsoon convection and an SMC driven by the strong temperature gradient over the Sahel region. However, the West African SMC is dry and forced by sensible heating over the Sahel and Saharan Desert. This dissertation presented new insights on the diurnal variation of the West African

meridional overturning and convection during the pre-monsoon (AMJ) and monsoon (JAS) seasons. ERA5 dynamical fields showed evidence of multiple low-level wind features throughout the day. The afternoon sea breeze front forces low-level convergence that triggers convective systems and assists in their propagation from the coast inland. Two NLLJs were detected: the coastal NLLJ and SLLJ. The coastal NLLJ is only evident during the monsoon season and provides a source of inland moisture, while the SLLJ forces low-level convergence over the Saharan heat low enhancing the dry SMC throughout the year.

During the pre-monsoon season, when the zonal precipitation band is located over the Gulf of Guinea, a sea breeze front initiates intense precipitation over the coastal region and propagates convective systems onshore during the early afternoon. The sea breeze front penetrates farther inland once turbulence in the PBL dies down in the evening. The SLLJ drives strong low-level convergence into the West African heat low, around 15°N, and the associated dry SMC intensifies during nighttime when the PBL is stratified, and wind shear is weak. During the monsoon season, when the zonal precipitation band is located inland at 10°N, the sea breeze front is linked to shallow convective systems and seems to not interact with the main West African monsoon convection located farther inland. At night, the coastal NLLJ replaces the sea breeze feature and the SLLJ forces low-level convergence into the dry Saharan SMC at around 22°N.

I complemented the ERA5 analysis with observations from the TRMM and GPM precipitation radars. ERA5 has a small precipitation bias over the coastal region where

the sea breeze front plays an important role in triggering convection during the early afternoon. However, ERA5 strongly underestimates precipitation over the Gulf of Guinea during the pre-monsoon and farther inland during the monsoon, when each region is experiencing large rain amounts. This underestimation occurs in both the convective and large-scale rain fields so fixing the underestimation would require assessing the convective parameterization, the large-scale microphysics, and their interaction. Although ERA5 shows biases in the diurnal cycle of precipitation, it is able to capture many of the dynamical features associated with the diurnal low-level circulation features over West Africa, like the sea breeze and NLLJs, probably because if its high temporal and spatial resolution.

# REFERENCES


Arakawa, A., & Schubert, W. H. (1974). Interaction of a Cumulus Cloud Ensemble with the Large-Scale Environment, Part I. *Journal of Atmospheric Sciences*, *31(3)*, 148–162.

Awaka, J., Iguchi, T., & Okamoto, K. (2007). Rain type classification algorithm. *Springer*, 213–224.

Back, L. E., & Bretherton, C. S. (2006). Geographic variability in the export of moist static energy and vertical motion profiles in the tropical Pacific. *Geophysical Research Letters*, *33*(17), 1–5. https://doi.org/10.1029/2006GL026672

Back, L. E., & Bretherton, C. S. (2009). On the relationship between SST gradients, boundary layer winds, and convergence over the tropical oceans. *Journal of Climate*, *22*(15), 4182–4196.

Banacos, P. C., & Schultz, D. M. (2005). The Use of Moisture Flux Convergence in Forecasting Convective Initiation: Historical and Operational Perspectives. *Weather and Forecasting*, *20(3)*, 351–366.

Baranowski, D. B., Flatau, M. K., Flatau, P. J., & Matthews, A. J. (2016). Impact of atmospheric convectively coupled equatorial Kelvin waves on upper ocean variability. *Journal of Geophysical Research : Atmospheres*, 2045–2059. https://doi.org/10.1002/2015JD024150.Received

Berry, G., Thorncroft, C., & Hewson, T. (2007). African Easterly Waves during 2004 — Analysis Using Objective Techniques. *Monthly Weather Review*, *135(4)*, 1251–

1267. https://doi.org/10.1175/MWR3343.1

Bosilovich, M. G., Lucchesi, R., & Suarez, M. (2015). MERRA-2: File specification.

Bouniol, D., Couvreux, F., Kamsu-Tamo, P. H., Leplay, M., Guichard, F., Favot, F., & O'connor, E. J. (2012). Diurnal and seasonal cycles of cloud occurrences, types, and radiative impact over West Africa. *Journal of Applied Meteorology and Climatology*, *51*(3), 534–553. https://doi.org/10.1175/JAMC-D-11-051.1

Collow, A. B., Ghate, V. P., Miller, M. A., & Trabachino, L. C. (2016). A one-year study of the diurnal cycle of meteorology, clouds and radiation in the West African Sahel region. *Quarterly Journal of the Royal Meteorological Society*, *142*(694), 16–29. https://doi.org/10.1002/qj.2623

Dai, A. (2006). Precipitation characteristics in eighteen coupled climate models. *Journal of Climate*, *19*(18), 4605–4630. https://doi.org/10.1175/JCLI3884.1

Diro, G. T., Rauscher, S. A., Giorgi, F., & Tompkins, A. M. (2012). Sensitivity of seasonal climate and diurnal precipitation over Central America to land and sea surface schemes in RegCM4. *Climate Research*, *52*(1), 31–48. https://doi.org/10.3354/cr01049

Dominguez, C., Done, J. M., & Bruyère, C. L. (2020). Easterly wave contributions to seasonal rainfall over the tropical Americas in observations and a regional climate model. *Climate Dynamics*, *54*(1), 191–209. https://doi.org/10.1007/s00382-019-04996-7

Fiedler, S., Crueger, T., D'Agostino, R., Peters, K., Becker, T., Leutwyler, D., … Stevens, B. (2020). Simulated tropical precipitation assessed across three major

phases of the coupled model intercomparison project (CMIP). *Monthly Weather Review*, *148*(9), 3653–3680. https://doi.org/10.1175/MWR-D-19-0404.1

Fiedler, S., Schepanski, K., Heinold, B., Knippertz, P., & Tegen, I. (2013). Climatology of nocturnal low-level jets over North Africa and implications for modeling mineral dust emission. *Journal of Geophysical Research Atmospheres*, *118*(12), 6100–6121. https://doi.org/10.1002/jgrd.50394

Fink, A. H., Engel, T., Ermert, V., Van der Linden, R., Schneidewind, M., Redl, R., … Others. (2017). Mean climate and seasonal cycle. *Meteorology of Tropical West Africa: The Forecasters' Handbook*, 1–39.

Fink, A., Paeth, H., Ermert, V., Pohle, S., & Diederich, M. (2010). I-5.1 Meteorological processes influencing the weather and climate of Benin.

Frank, W., & Roundy, P. E. (2006). The Role of Tropical Waves in Tropical Cyclogenesis. *Monthly Weather Review*, *134(9)*, 2397–2417.

Frierson, D. M. W. (2007). The dynamics of idealized convection schemes and their effect on the zonally averaged tropical circulation. *Journal of the Atmospheric Sciences*, *64*(6), 1959–1974. https://doi.org/10.1175/JAS3935.1

Fuchs-Stone, Ž., Raymond, D. J., & Sentic, S. (2020). OTREC2019 : Convection Over the East Paci fi c and Southwest Caribbean. *Geophysical Research Letters*, *47(11)*(2017), 1–8. https://doi.org/10.1029/2020GL087564

Funk, A., Schumacher, C., & Awaka, J. (2013). Analysis of rain classifications over the tropics by version 7 of the TRMM PR 2A23 algorithm. *Journal of the Meteorological Society of Japan. Ser. II*, *91(3)*, 257–272.

Gelaro, R., McCarty, W., Suárez, M. J., Todling, R., Molod, A., Takacs, L., … Zhao, B. (2017). The modern-era retrospective analysis for research and applications, version 2 (MERRA-2). *Journal of Climate*, *30*(14), 5419–5454. https://doi.org/10.1175/JCLI-D-16-0758.1

Gomes, H. B., Ambrizzi, T., Pontes, B. F., Hodges, K., Silva, P. L., Herdies, D. L., … Heliofábio, L. S. (2019). Climatology of easterly wave disturbances over the tropical South Atlantic. *Climate Dynamics*, *53*(3), 1393–1411. https://doi.org/10.1007/s00382-019-04667-7

Gounou, A., Guichard, F., & Couvreux, F. (2012). Observations of Diurnal Cycles Over a West African Meridional Transect: Pre-Monsoon and Full-Monsoon Seasons. *Boundary-Layer Meteorology*, *144*(3), 329–357. https://doi.org/10.1007/s10546-012-9723-8

Grams, C. M., Jones, S. C., Marsham, J. H., Parker, D. J., Haywood, J. M., & Heuveline, V. (2010). The Atlantic inflow to the Saharan heat low: Observations and Modelling. *Quarterly Journal of the Royal Meteorological Society*, *136*(SUPPL. 1), 125–140. https://doi.org/10.1002/qj.429

Gu, G., & Adler, R. F. (2004). Seasonal evolution and variability associated with the West African monsoon system. *Journal of Climate*, *17*(17), 3364–3377. https://doi.org/10.1175/1520-0442(2004)017<3364:SEAVAW>2.0.CO;2

Guedje, F. K., Houeto, A. V., Houngninou, E. B., Fink, A. H., & Knippertz, P. (2019). Climatology of coastal wind regimes in Benin. *Meteorologische Zeitschrift*, 23–39.

Haerter, J. O., & Berg, P. (2009). Unexpected rise in extreme precipitation caused by a

shift in rain type? *Nature Geoscience*, *2*(6), 372–373. https://doi.org/10.1038/ngeo523

Hagos, S., & Zhang, C. (2010). Diabatic heating, divergent circulation and moisture transport in the African monsoon system, *136*(December 2009), 411–425. https://doi.org/10.1002/qj.538

Hagos, S., Zhang, C., Tao, W. K., Lang, S., Takayabu, Y. N., Shige, S., … L'ecuyer, T. (2010). Estimates of tropical diabatic heating profiles: Commonalities and uncertainties. *Journal of Climate*, *23*(3), 542–558. https://doi.org/10.1175/2009JCLI3025.1

Handlos, Z. J., & Back, L. E. (2014). Estimating vertical motion profile shape within tropical weather states over the oceans. *Journal of Climate*, *27*(20), 7667–7686. https://doi.org/10.1175/JCLI-D-13-00602.1

Hersbach, H., Bell, B., Berrisford, P., Hirahara, S., Horanyi, A., Munoz-Sabater, J., … Others. (2020). The ERA5 Atmospheric Reanalysis. *Quarterly Journal of the Royal Meteorological Society*, *146(730)*, 1999–2049.

Hodges, K. I., Chappell, D. W., Robinson, G. J., & Yang, G. (2000). An Improved Algorithm for Generating Global Window Brightness Temperatures from Multiple Satellite Infrared Imagery. *Journal of Atmospheric and Oceanic Technology*, 1296–1312.

Hodges, K. (1995). Feature tracking on the unit sphere. *Monthly Weather Review*, *123(12)*, 3458–3465.

Hodges, K. (1999). Adaptive Constraints for Feature Tracking. *Monthly Weather*

*Review*, (127(6)), 1362–1373.

Holloway, C. E., & Neelin, J. D. (2009). Moisture Vertical Structure , Column Water Vapor , and Tropical Deep Convection. *Journal of Atmospheric Sciences*, *66(6)*, 1665–1683. https://doi.org/10.1175/2008JAS2806.1

Hoskins, B. J., James, I. N., & White, G. H. (1983). The Shape, Propagation and Mean-Flow Interaction of Large-Scale Weather Systems. *Journal of the Atmospheric Sciences*. https://doi.org/10.1175/1520-0469(1983)040<1595:TSPAMF>2.0.CO;2

Hou, A. Y., Kakar, R. K., Neeck, S., Azarbarzin, A. A., Kummerow, C. D., Kojima, M., … Iguchi, T. (2014). The global precipitation measurement mission. *Bulletin of the American Meteorological Society*, *95(5)*(May), 701–722. https://doi.org/10.1175/BAMS-D-13-00164.1

Houze, R. A. (1989). Observed structure of mesoscale convective systems and implications for large-scale heating. *Quarterly Journal of the Royal Meteorological Society*, *115*(487), 425–461.

Houze, R. A. (1997). Stratiform Precipitation in Regions of Convection: A Meteorological Paradox? *Bulletin of the American Meteorological Society*, *78*(10), 2179–2196. https://doi.org/10.1175/1520-0477(1997)078<2179:SPIROC>2.0.CO;2

Huaman, L., & Schumacher, C. (2018). Assessing the vertical latent heating structure of the east Pacific ITCZ using the CloudSat CPR and TRMM PR. *Journal of Climate*, *31*(7). https://doi.org/10.1175/JCLI-D-17-0590.1

Huaman, L., Schumacher, C., & Kiladis, G. N. (2020). Eastward-Propagating Disturbances in the Tropical Pacific. *Monthly Weather Review*, *148(9)*, 3713–3728.

https://doi.org/10.1175/MWR-D-20-0029.1

Huaman, L., & Takahashi, K. (2016). The vertical structure of the eastern Pacific ITCZs and associated circulation using the TRMM Precipitation Radar and in situ data. *Geophysical Research Letters*, *43*(15), 8230–8239. https://doi.org/10.1002/2016GL068835

Huang, P., & Huang, R. (2011). Climatology and Interannual Variability of Convectively Coupled Equatorial Waves Activity. *Journal of Climate*, 4451–4465. https://doi.org/10.1175/2011JCLI4021.1

Huffman, G. J., Bolvin, D. T., Braithwaite, D., Hsu, K., Joyce, R., Xie, P., & Yoo, S.-H. (2015). NASA global precipitation measurement (GPM) integrated multi-satellite retrievals for GPM (IMERG). *Algorithm Theoretical Basis Document (ATBD) Version*, *4*.

Huffman, G. J., Bolvin, D. T., Nelkin, E. J., Wolff, D. B., Adler, R. F., Gu, G., … Stocker, E. F. (2007). The TRMM Multisatellite Precipitation Analysis (TMPA): Quasi-Global, Multiyear, Combined-Sensor Precipitation Estimates at Fine Scales. *Journal of Hydrometeorology*, *8*(1), 38–55. https://doi.org/10.1175/JHM560.1

Inoue, K., & Back, L. (2015). Column-Integrated Moist Static Energy Budget Analysis on Various Time Scales during TOGA COARE. *Journal of the Atmospheric Sciences*, *72(5)*, 1856–1871. https://doi.org/10.1175/JAS-D-14-0249.1

Janiga, M. A., & Thorncroft, C. D. (2013). Regional differences in the kinematic and thermodynamic structure of African easterly waves. *Quarterly Journal of the Royal Meteorological Society*, *139(675)*, 1598–1614. https://doi.org/10.1002/qj.2047

Janiga, M. A., & Thorncroft, C. D. (2014). Convection over tropical Africa and the East Atlantic during the West African monsoon: Regional and diurnal variability. *Journal of Climate*, *27*(11), 4189–4208. https://doi.org/10.1175/JCLI-D-13-00449.1

Jaramillo, L., Poveda, G., & Mejia, J. F. (2017). Mesoscale convective systems and other precipitation features. *International Journal of Climatology*, *37*, 380–397. https://doi.org/10.1002/joc.5009

Kiladis, G. N., & Weickmann, K. M. (1992). Extratropical forcing of tropical Pacific convection during northern winter. *Monthly Weather Review, 120(9)*, 1924–1939.

Kiladis, G. N., & Weickmann, K. M. (1997). Horizontal Structure and Seasonality of Large-Scale Circulations Associated with Submonthly Tropical Convection. *Monthly Weather Review, 125(9)*, 1997–2013.

Kiladis, G. N., Wheeler, M. C., Haertel, P. T., Straub, K. H., & Roundy, P. E. (2009). Convectively Coupled Equatorial Waves. *Reviews of Geophysics*, (47(2)). https://doi.org/10.1029/2008RG000266.1.

Kiladis, G. N. (1998). Observations of Rossby Waves Linked to Convection over the Eastern Tropical Pacific. *Journal of the Atmospheric Sciences*, *55*(3), 321–339. https://doi.org/10.1175/1520-0469(1998)055<0321:OORWLT>2.0.CO;2

Kiladis, G. N., Thorncroft, C. D., & Hall, N. M. (2006). Three-Dimensional Structure and Dynamics of African Easterly Waves . Part I : Observations. *Journal of Atmospheric Sciences*, *63(9)*, 2212–2230.

Kniffka, A., Knippertz, P., & Fink, A. H. (2019). The role of low-level clouds in the West African monsoon system. *Atmospheric Chemistry and Physics*, *19(3)*, 1623–

1647.

Kobayashi, S., Ota, Y., Harada, Y., Ebita, A., Moriya, M., Onoda, H., … Others. (2015). The JRA-55 reanalysis: General specifications and basic characteristics. *Journal of the Meteorological Society of Japan. Ser. II*, *93*, 5–48.

Kodama, Y. M., Katsumata, M., Mori, S., Satoh, S., Hirose, Y., & Ueda, H. (2009). Climatology of warm rain and associated latent heating derived from TRMM PR observations. *Journal of Climate*, *22*(18), 4908–4929. https://doi.org/10.1175/2009JCLI2575.1

Laing, A. G., Carbone, R., Levizzani, V., & Tuttle, J. (2018). The propagation and diurnal cycles of deep convection in northern tropical Africa. *Quarterly Journal of the Royal Meteorological Society*, *134(630)*, 93–109. https://doi.org/10.1002/qj

Lavaysse, C., Flamant, C., Janicot, S., Parker, D. J., Lafore, J. P., Sultan, B., & Pelon, J. (2009). Seasonal evolution of the West African heat low: A climatological perspective. *Climate Dynamics*, *33*(2–3), 313–330. https://doi.org/10.1007/s00382-009-0553-4

Liebmann, B., Kiladis, G. N., Carvalho, L. M., Jones, C., Vera, C. S., Bladé, I., & Allured, D. (2009). Origin of Convectively Coupled Kelvin Waves over South America. *Journal of Climate*, *22(2)*, 300–315. https://doi.org/10.1175/2008JCLI2340.1

Lindzen, R. S., & Nigan, S. (1987). On the Role of Sea Surface Temperature Gradients in Forcing Low-Level Winds and Convergence in the Tropics. *Journal of the Atmospheric Sciences*, *44*.

Liu, C., Shige, S., Takayabu, Y. N., & Zipser, E. (2015). Latent heating contribution from precipitation systems with different sizes, depths, and intensities in the tropics. *Journal of Climate*, *28*(1), 186–203. https://doi.org/10.1175/JCLI-D-14-00370.1

Liu, W., Cook, K. H., & Vizy, E. K. (2020). Role of the West African westerly jet in the seasonal and diurnal cycles of precipitation over West Africa. *Climate Dynamics*, *54*(1–2), 843–861. https://doi.org/10.1007/s00382-019-05035-1

Livezey, R. E., & Chen, W. Y. (1983). Statistical field significance and its determination by Monte Carlo techniques. *Monthly Weather Review*, *111(1)*, 46–59.

Lohou, F., Kalthoff, N., Adler, B., Babic, K., Dione, C., Lothon, M., … Zouzoua, M. (2020). Conceptual model of diurnal cycle of low-level stratiform clouds over southern West Africa. *Atmospheric Chemistry and Physics*, *20(4)*, 2263–2275.

Lothon, M., Saïd, F., Lohou, F., & Campistron, B. (2008). Observation of the diurnal cycle in the low troposphere of West Africa. *Monthly Weather Review*, *136*(9), 3477–3500. https://doi.org/10.1175/2008MWR2427.1

Mapes, B. E., & Houze Jr, R. A. (1995). Diabatic divergence profiles in western Pacific mesoscale convective systems. *Journal of Atmospheric Sciences*, *52(10)*, 1807–1828.

Maranan, M., Fink, A. H., & Knippertz, P. (2018). Rainfall types over southern West Africa: Objective identification, climatology and synoptic environment. *Quarterly Journal of the Royal Meteorological Society*, *144*(714), 1628–1648. https://doi.org/10.1002/qj.3345

Marchand, R., Mace, G. G., Ackerman, T., & Stephens, G. (2008). Hydrometeor

Detection Using Cloudsat — An Earth-Orbiting 94-GHz Cloud Radar. *Journal of Atmospheric and Oceanic Technology*, *25(4)*, 519–533. https://doi.org/10.1175/2007JTECHA1006.1

Martin, E. R., & Schumacher, C. (2011). Modulation of Caribbean Precipitation by the Madden – Julian Oscillation. *Journal of Climate*, *24(3)*, 813–824. https://doi.org/10.1175/2010JCLI3773.1

Masunaga, H., & Luo, Z. J. (2016). Convective and large-scale mass flux profiles over tropical oceans determined from synergistic analysis of a suite of satellite observations. *Journal of Geophysical Research: Atmospheres*, *121(13)*, 7958–7974. https://doi.org/10.1002/2016JD024753.Abstract

Matsuno, T. (1966). Quasi-Geostrophic Motions Equatorial Area *, (February), 25–43.

Molinari, J., Knight, D., Dickinson, M., Vollaro, D., & Skubis, S. (1997). Potential Vorticity, Easterly Waves , and Eastern Pacific Tropical Cyclogenesis. *Monthly Weather Review*, *125(1)*, 2699–2708.

Molinari, J., & Vollaro, D. (2000). Planetary- and Synoptic-Scale Influences on Eastern Pacific Tropical Cyclogenesis. *Monthly Weather Review*, *128(9)*, 3296–3307.

Moorthi, S., & Suarez, M. J. (1992). Relaxed Arakawa-Schubert. A parameterization of moist convection for general circulation models. *Monthly Weather Review*, *148*, 148–162.

NASA/JAXA. (2016). Tropical rainfall measuring mission (TRMM) precipitation radar algorithm. Instruction manual for version 7. [Available at http://www.eorc.jaxa.jp/TRMM/documents/PR_algorithm_product_information/pr_

manual/ PR_Instruction_Manual_V7_L1.pdf.].

Neelin, J. D., & Held, I. M. (1987). Modeling tropical convergence based on the moist static energy budget. *Monthly Weather Review*, *115(1)*, 148–162.

Nesbitt, S. W., & Zipser, E. J. (2003). The diurnal cycle of rainfall and convective intensity according to three years of TRMM measurements. *Journal of Climate*, *16*(10), 1456–1475. https://doi.org/10.1175/1520-0442-16.10.1456

Nolan, D. S., & Rappin, E. D. (2008). Increased sensitivity of tropical cyclogenesis to wind shear in higher SST environments. *Geophysical Research Letters*, *35(14)*, 1–7. https://doi.org/10.1029/2008GL034147

Numaguti, A. (1993). Dynamics and energy balance of the Hadley circulation and the tropical precipitation zones: Significance of the distribution of evaporation. *Journal of Atmospheric Sciences*, *50(13)*, 1874–1887.

Ortega, S., Webster, P. J., Toma, V., & Chang, H. R. (2018). The effect of potential vorticity fluxes on the circulation of the. *Quarterly Journal of the Royal Meteorological Society*, (2017), 848–860. https://doi.org/10.1002/qj.3261

Pan, H., & Wu, W.-S. (1995). Implementing a mass flux convection parameterization package for the NMC medium-range forecast model.

Parker, D. J., Burton, R. R., Diongue-Niang, A., Ellis, R. J., Felton, M., Taylor, C. M., … Tompkins, A. M. (2005). The diurnal cycle of the West African monsoon circulation. *Quarterly Journal of the Royal Meteorological Society*, *131*(611), 2839–2860. https://doi.org/10.1256/qj.04.52

Pasch, R. J., Blake, E. S., Avila, L. A., Beven, J. L., Brown, D. P., Franklin, J. L., …

Stewart, S. R. (2009). Eastern North Pacific Hurricane Season of 2006. *Monthly Weather Review*, *137(1)*, 3–20. https://doi.org/10.1175/2008MWR2508.1

Petersen, W. A., Cifelli, R., Boccippio, D. J., Rutledge, S. A., & Fairall, C. W. (2003). Convection and Easterly Wave Structures Observed in the Eastern Pacific Warm Pool during EPIC-2001. *Journal of the Atmospheric Sciences*, *60*(15), 1754–1773. https://doi.org/10.1175/1520-0469(2003)060<1754:CAEWSO>2.0.CO;2

Pfeifroth, U., Trentmann, J., Fink, A. H., & Ahrens, B. (2016). Evaluating satellite-based diurnal cycles of precipitation in the African tropics. *Journal of Applied Meteorology and Climatology*, *55*(1), 23–39. https://doi.org/10.1175/JAMC-D-15-0065.1

Poveda, G., Jaramillo, L., & Vallejo, L. F. (2014). Seasonal precipitation patterns along pathways of South American low-level jets and aerial rivers Germ, *50*(3), 98–118. https://doi.org/10.1002/2013WR014087

Racz, Z., & Smith, R. K. (1999). The dynamics of heat lows Heat lows or troughs are a prominent climatological feature of many arid land areas of the world during the wanner months , especially in low latitudes where insolation is at corresponding isotherms at 850 mb for a typical situat. *Quarterly Journal of the Royal Meteorological Society*, *125(553)*, 225–252.

Rapp, A. D., Peterson, A. G., Frauenfeld, O. W., Quiring, S. M., & Roark, E. B. (2014). Climatology of Storm Characteristics in Costa Rica using the TRMM Precipitation Radar. *Journal of Hydrometeorology*, *15(6)*, 2615–2633. https://doi.org/10.1175/JHM-D-13-0174.1

Rauber, R. M., Ellis, S. M., Vivekanandan, J., Stith, J., Lee, W.-C., McFarquhar, G. M., … Janiszeski, A. (2017). Finescale structure of a snowstorm over the northeastern United States: A first look at high-resolution HIAPER cloud radar observations. *Bulletin of the American Meteorological Society*, *98(2)*, 253–270. https://doi.org/10.1175/BAMS-D-15-00180.1

Raymond, D. J., Gjorgjievska, S., Sessions, S., & Fuchs, Z. (2014). Tropical cyclogenesis and mid-level vorticity. *Aust. Meteorol. Oceanogr.*, *64(11)*.

Raymond, D. J., Sessions, S. L., Sobel, A. H., & Fuchs, Ž. (2009). The Mechanics of Gross Moist Stability. *Journal of Advances in Modeling Earth Systems*, *1*(3), n/a-n/a. https://doi.org/10.3894/james.2009.1.9

Raymond, D. J., & Torres, D. J. (1998). Fundamental Moist Modes of the Equatorial Troposphere. *Journal of the Atmospheric Sciences*, *55(10)*, 1771–1790.

Raymond, D., Lopez-Carrillo, C., & Cavazos, L. L. (2005). Case-studies of developing east Pacific easterly waves. *Quarterly Journal of the Royal Meteorological Society*, *124(550)*, 2005–2034.

Reed, R. J., & Johnson, R. H. (1974). The vorticity budget of synoptic-scale wave disturbances in the tropical western Pacific. *Journal of Atmospheric Sciences*, *31(7)*, 1784–1790.

Reed, R. J., Norquist, D. C., & Recker, E. E. (1977). The structure and properties of African wave disturbances as observed during phase III of GATE. *Monthly Weather Review*, *105(3)*, 317–333.

Reed, R. J., & Recker, E. E. (1971). Structure and Properties of Synoptic-Scale Wave

Disturbances in the Equatorial Western Pacific. *Journal of the Atmospheric Sciences*. https://doi.org/10.1175/1520-0469(1971)028<1117:SAPOSS>2.0.CO;2

Rennick, M. A. (1976). The generation of African waves. *Journal of Atmospheric Sciences*, *33(10)*, 1955–1969.

Riehl, H. (1954). *Tropical Meteorology*. McGraw-Hill.

Roundy, P. E., & Frank, W. M. (2004). A Climatology of Waves in the Equatorial Region. *Journal of Atmospheric Sciences*, 2105–2132.

Rydbeck, A. V, & Maloney, E. D. (2014). Energetics of East Pacific Easterly Waves during Intraseasonal Events. *Journal of Climate*, *27(20)*(1962), 7603–7621. https://doi.org/10.1175/JCLI-D-14-00211.1

Rydbeck, A. V, & Maloney, E. D. (2015). On the Convective Coupling and Moisture Organization of East Pacific Easterly Waves. *Journal of the Atmospheric Sciences*, *72(10)*, 3850–3870. https://doi.org/10.1175/JAS-D-15-0056.1

Rydbeck, A. V, Maloney, E. D., & Alaka Jr, G. J. (2017). In Situ Initiation of East Pacific Easterly Waves in a Regional Model. *Journal of the Atmospheric Sciences*, *74(2)*(2015), 333–351. https://doi.org/10.1175/JAS-D-16-0124.1

Saha, S., Moorthi, S., Wu, X., Wang, J., Nadiga, S., Tripp, P., … Becker, E. (2014). The NCEP climate forecast system version 2. *Journal of Climate*, *27*(6), 2185–2208. https://doi.org/10.1175/JCLI-D-12-00823.1

Schumacher, C., Houze Jr, R. A., & Kraucunas, I. (2004). The Tropical Dynamical Response to Latent Heating Estimates Derived from the TRMM Precipitation Radar. *Journal of the Atmospheric Sciences*, *61(12)*, 1341–1358.

Schumacher, C., & Houze, R. A. (2003). Stratiform rain in the tropics as seen by the TRMM precipitation radar. *Journal of Climate*, *16*(11), 1739–1756. https://doi.org/10.1175/1520-0442(2003)016<1739:SRITTA>2.0.CO;2

Schumacher, C., & Houze, R. A. (2006). Stratiform precipitation production over sub-Saharan Africa and the tropical East Atlantic as observed by TRMM. *Quarterly Journal of the Royal Meteorological Society*, *132*(620), 2235–2255. https://doi.org/10.1256/qj.05.121

Schumacher, C., Houze, R. a., & Kraucunas, I. (2004). The Tropical Dynamical Response to Latent Heating Estimates Derived from the TRMM Precipitation Radar. *Journal of the Atmospheric Sciences*, *61*, 1341–1358. https://doi.org/10.1175/1520-0469(2004)061<1341:TTDRTL>2.0.CO;2

Serra, Y. L., & Houze Jr, R. A. (2002). Observations of Variability on Synoptic Timescales in the East Pacific ITCZ *. *Journal of the Atmospheric Sciences*, *59(10)*, 1723–1743.

Serra, Y. L., Jiang, X., Tian, B., Amador-astua, J., Maloney, E. D., & Kiladis, G. N. (2014). Tropical Intraseasonal Modes of the Atmosphere. *Annual Review of Environment and Resources*, *39*, 189–215. https://doi.org/10.1146/annurev-environ-020413-134219

Serra, Y. L., Kiladis, G. N., & Cronin, M. F. (2008). Horizontal and Vertical Structure of Easterly Waves in the Pacific ITCZ. *Journal of the Atmospheric Sciences*, *65*(4), 1266–1284. https://doi.org/10.1175/2007JAS2341.1

Serra, Y. L., Kiladis, G. N., & Hodges, K. I. (2010). Tracking and Mean Structure of

Easterly Waves over the Intra-Americas Sea. *Journal of Climate*, *23(18)*, 4823–4840. https://doi.org/10.1175/2010JCLI3223.1

Shapiro, L. J. (1986). The three-dimensional structure of synoptic-scale disturbances over the tropical Atlantic. *Monthly Weather Review*, *114(10)*, 1876–1891.

Sherwood, S. C., Minnis, P., & Mcgill, M. (2004). Deep convective cloud-top heights and their thermodynamic control during CRYSTAL-FACE. *Journal of Geophysical Research: Atmospheres*, *109*, 1–11. https://doi.org/10.1029/2004JD004811

Shige, S., Takayabu, Y. N., Tao, W.-K., & Johnson, D. E. (2004). Spectral retrieval of latent heating profiles from TRMM PR data. Part I: Development of a model-based algorithm. *Journal of Applied Meteorology*, *43*(8), 1095–1113.

Shige, S., Takayabu, Y. N., Tao, W.-K., & Shie, C.-L. (2007). Spectral retrieval of latent heating profiles from TRMM PR data. Part II: Algorithm improvement and heating estimates over tropical ocean regions. *Journal of Applied Meteorology and Climatology*, *46*(7), 1098–1124.

Sobel, A. H. (2007). Simple models of ensemble-averaged precipitation and surface wind, given the sea surface temperature. *The Global Circulation of the Atmosphere*, *219*.

Sobel, A. H., Nilsson, J., & Polvani, L. M. (2001). The weak temperature gradient approximation and balanced tropical moisture waves. *Journal of the Atmospheric Sciences*, *58*(23), 3650–3665. https://doi.org/10.1175/1520-0469(2001)058<3650:TWTGAA>2.0.CO;2

Spengler, T., Reeder, M. J., & Smith, R. K. (2005). The dynamics of heat lows in simple

background flows. *Quarterly Journal of the Royal Meteorological Society*, *131*(612), 3147–3165. https://doi.org/10.1256/qj.04.177

Stan, C., Straus, D. M., Frederiksen, J. S., Lin, H., Maloney, E. D., & Schumacher, C. (2017). Review of Tropical-Extratropical Teleconnections on Intraseasonal Time Scales. *Reviews of Geophysics*, *55(4)*, 902–937. https://doi.org/10.1002/2016RG000538

Stein, T. H. M., Parker, D. J., Delanoë, J., Dixon, N. S., Hogan, R. J., Knippertz, P., … Marsham, J. H. (2011). The vertical cloud structure of the West African monsoon: A 4 year climatology using CloudSat and CALIPSO. *Journal of Geophysical Research Atmospheres*, *116*(22), 1–13. https://doi.org/10.1029/2011JD016029

Steiner, M., Houze Jr, R. A., & Yuter, S. E. (1995). Climatological characterization of three-dimensional storm structure from operational radar and rain gauge data. *Journal of Applied Meteorology and Climatology*, *148*, 148–162.

Stephens, G. L., Vane, D. G., Boain, R. J., Mace, G. G., Sassen, K., Wang, Z., ... & CloudSat Science Team. (2002). The CloudSat mission and the A-Train: A new dimension of space-based observations of clouds and precipitation. *Bulletin of the American Meteorological Society*, *83(12)*(2002).

Stocker, E. F., Alquaied, F., Bilanow, S., Ji, Y., & Jones, L. (2018). TRMM version 8 reprocessing improvements and incorporation into the GPM data suite. *Journal of Atmospheric and Oceanic Technology*, *35*(6), 1181–1199. https://doi.org/10.1175/JTECH-D-17-0166.1

Straub, K. H., & Kiladis, G. N. (2002). Observations of a Convectively Coupled Kelvin

Wave in the Eastern Pacific ITCZ. *Journal of the Atmospheric Sciences*, *59*(1), 30–53. https://doi.org/10.1175/1520-0469(2002)059<0030:OOACCK>2.0.CO;2

Straub, K. H., & Kiladis, G. N. (2003). Extratropical Forcing of Convectively Coupled Kelvin Waves during Austral Winter. *Journal of the Atmospheric Sciences*, *60*(3), 526–543. https://doi.org/10.1175/1520-0469(2003)060<0526:EFOCCK>2.0.CO;2

Sultan, B., Janicot, S., & Drobinski, P. (2007). Characterization of the diurnal cycle of the West African monsoon around the monsoon onset. *Journal of Climate*, *20*(15), 4014–4032. https://doi.org/10.1175/JCLI4218.1

Tai, K.-S., & Ogura, Y. (1987). An observational study of easterly waves over the eastern Pacific in the northern summer using FGGE data. *Journal of Atmospheric Sciences*, *44(2)*, 339–361.

Tao, W.-K., Lang, S., Olson, W. S., Meneghini, R., Yang, S., Simpson, J., … Halverson, J. (2001). Retrieved vertical profiles of latent heat release using TRMM rainfall products for February 1998. *J. Appl. Meteor.*, *40*(February 1988), 957–982. https://doi.org/10.1175/1520-0450(2001)040<0957:RVPOLH>2.0.CO;2

Tao, W.-K., Lang, S., Zeng, X., Shige, S., & Takayabu, Y. (2010). Relating convective and stratiform rain to latent heating. *Journal of Climate*, *23*(7), 1874–1893.

Thompson Jr, R. M., Payne, S. W., Recker, E. E., & Reed, R. J. (1979). Structure and properties of synoptic-scale wave disturbances in the intertropical convergence zone of the eastern Atlantic. *Journal of Atmospheric Sciences*, *36(1)*, 53–72.

Thorncroft, C., & Blackburn, M. (1999). Maintenance of the African easterly jet. *Quarterly Journal of the Royal Meteorological Society*, *125(555)*, 763–786.

https://doi.org/10.1256/qj.03.130

Thorncroft, C. D., Nguyen, H., Zhang, C., & Peyrille, P. (2011). Annual cycle of the West African monsoon: Regional circulations and associated water vapour transport. *Quarterly Journal of the Royal Meteorological Society*, *137*(654), 129–147. https://doi.org/10.1002/qj.728

Thorncroft, C., & Hoskins, B. (1993). An idealized study of African easterly waves . I : A linear view. *Quarterly Journal of the Royal Meteorological Society*, *120(518)*, 953–982.

Tiedtke, M. (1989). A comprehensive mass flux scheme for cumulus parameterization in large-scale models. *Monthly Weather Review*, *117(8)*, 1779–1800.

Toma, V. E., & Webster, P. J. (2010a). Oscillations of the intertropical convergence zone and the genesis of easterly waves . Part I : diagnostics and theory. *Climate Dynamics*, *34(4)*, 587–604. https://doi.org/10.1007/s00382-009-0584-x

Toma, V. E., & Webster, P. J. (2010b). Oscillations of the Intertropical Convergence Zone and the genesis of easterly waves Part II : numerical verification. *Climate Dynamics*, *34(4)*, 605–613. https://doi.org/10.1007/s00382-009-0585-9

Tomas, R. A., & Webster, P. J. (1994). Horizontal and vertical structure of cross-equatorial wave propagation. *Journal of Atmospheric Sciences*, *51(11)*, 1417–1430.

Trenberth, K. E., Stepaniak, D. P., & Caron, J. M. (2000). The Global Monsoon as Seen through the Divergent Atmospheric Circulation. *Journal of Climate*, *13(22)*, 3969–3993.

Van der Linden, R., Fink, A. H., & Redl, R. (2015). Satellite-based climatology of low-

level continental clouds in southern West Africa during the summer monsoon season. *Journal of Geophysical Research: Atmospheres*, *120(3)*, 1186–1201. https://doi.org/10.1038/175238c0

Vincent, D. G. (1994). (1994). The South Pacific convergence zone (SPCZ): A review. *Monthly Weather Review*, *122(9)*, 1949–1970.

Vizy, E. K., & Cook, K. H. (2002). Development and application of a mesoscale climate model for the tropics: Influence of sea surface temperature anomalies on the West African monsoon. *Journal of Geophysical Research Atmospheres*, *107*(3). https://doi.org/10.1029/2001jd000686

Vizy, E. K., & Cook, K. H. (2019). Understanding the summertime diurnal cycle of precipitation over sub-Saharan West Africa: regions with daytime rainfall peaks in the absence of significant topographic features. *Climate Dynamics*, *52*(5–6), 2903–2922. https://doi.org/10.1007/s00382-018-4315-z

Vomel, H., Goodstein, M., Tudor, L., Witte, J., Fuchs-Stone, Z., Sentic, S., … Others. (2021). High-resolution in situ observations of atmospheric thermodynamics using dropsondes during the Organization of Tropical East Pacific Convection (OTREC) field campaign. *Earth System Science Data*, *13(3)*, 1107–1117.

Vondou, D. A., Nzeukou, A., Lenouo, A., & Mkankam Kamga, F. (2010). Seasonal variations in the diurnal patterns of convection in Cameroon-Nigeria and their neighboring areas. *Atmospheric Science Letters*, *11*(4), 290–300. https://doi.org/10.1002/asl.297

Wang, C., & Enfield, D. B. (2003). A further study of the tropical Western Hemisphere

warm pool. *Journal of Climate*, *16*(10), 1476–1493.

Warren, S. G., & Hahn, C. (2002). Cloud climatology. *Encyclopedia of Atmospheric Sciences*, *2*, 476–483.

Wheeler, M., & Kiladis, G. N. (1999). Convectively Coupled Equatorial Waves : Analysis of Clouds and Temperature in the Wavenumber – Frequency Domain. *Journal of Atmospheric Sciences*, *56(3)*, 374–399.

Whitaker, J. W., & Maloney, E. D. (2018). Influence of the Madden – Julian Oscillation and Caribbean Low-Level Jet on East Pacific Easterly Wave Dynamics. *Journal of the Atmospheric Sciences*, *75(4)*(2013), 1121–1141. https://doi.org/10.1175/JAS-D-17-0250.1

Whitaker, J. W., & Maloney, E. D. (2020). Genesis of an East Pacific Easterly Wave from a Panama Bight MCS : A Case Study Analysis from June 2012. *Journal of the Atmospheric Sciences*, *77(10)*, 3567–3584. https://doi.org/10.1175/JAS-D-20-0032.1

Wolding, B. O., & Maloney, E. D. (2015). Objective Diagnostics and the Madden – Julian Oscillation . Part II : Application to Moist Static Energy and Moisture Budgets. *Journal of Climate*, *28(19)*, 7786–7808. https://doi.org/10.1175/JCLI-D-14-00689.1

Wolding, B. O., Maloney, E. D., & Branson, M. (2016). Vertically resolved weak temperature gradient analysis of the Madden-Julian Oscillation in SP-CESM. *Journal of Advances in Modeling Earth Systems*, *8(4)*, 1586–1619. https://doi.org/10.1002/2016MS000724.Received

Yang, G. Y., & Slingo, J. (2001). The diurnal cycle in the tropics. *Monthly Weather Review*, *129*(1994), 784–801. https://doi.org/10.1175/1520-0493(2001)129<0784:TDCITT>2.0.CO;2

Ye, B., Del Genio, A. D., & Lo, K. K. (1998). CAPE Variations in the Current Climate and in a Climate Change. *Journal of Climate*, *11(8)*, 1997–2015.

Yokoyama, C., & Takayabu, Y. N. (2012). Relationships between Rain Characteristics and Environment . Part II : Atmospheric Disturbances Associated with Shallow Convection over the Eastern Tropical Pacific. *Monthly Weather Review*, *140(9)*, 2841–2859. https://doi.org/10.1175/MWR-D-11-00251.1

Yokoyama, C., Zipser, E. J., & Liu, C. (2014). TRMM-Observed shallow versus deep convection in the eastern Pacific related to large-scale circulations in reanalysis datasets. *Journal of Climate*, *27*(14), 5575–5592. https://doi.org/10.1175/JCLI-D-13-00315.1

Zehnder, J. A., Powell, D. M., & Ropp, D. L. (1999). The Interaction of Easterly Waves , Orography , and the Intertropical Convergence Zone in the Genesis of Eastern Pacific Tropical Cyclones. *Monthly Weather Review*, *127(7)*, 1566–1585.

Zhang, C., McGauley, M., & Bond, N. A. (2004). Shallow meridional circulation in the tropical eastern Pacific. *Journal of Climate*, *17*(1), 133–139. https://doi.org/10.1175/1520-0442(2004)017<0133:SMCITT>2.0.CO;2

Zhang, C., Nolan, D. S., Thorncroft, C. D., & Nguyen, H. (2008). Shallow meridional circulations in the tropical atmosphere. *Journal of Climate*, *21*(14), 3453–3470.

Zuidema, P., Mapes, B., Lin, J., Fairall, C., & Wick, G. (2006). The Interaction of

Clouds and Dry Air in the Eastern Tropical Pacific. *Journal of Climate*, *19(18)*, 4531–4544.